Dynamic regulation of autocatalytic EGFR activation

Dissertation

Zur Erlangung des akademischen Grades eines
Doktors der Naturwissenschaften
(Dr. rer. nat.)
der Fakultät Chemie und Chemische Biologie
der Technischen Universität Dortmund

vorgelegt von

Martin Baumdick

Oktober 2017

Vorgelegt im Oktober 2017

von Martin Baumdick

Gutachter:
Prof. Dr. Philippe Bastiaens
Prof. Dr. Roger Goody

Main work presented in this dissertation was performed in the laboratory of Prof. Dr. Philippe Bastiaens at the Max Planck Institute of Molecular Physiology in Dortmund (Germany).

Martin Baumdick was awarded an EMBO short-term fellowship to visit the laboratory of Prof. Dr. Jason Chin at the Laboratory of Molecular Biology, MRC in Cambridge (UK) in September-November 2015.

Eidesstattliche Versicherung (Affidavit)

Name, Vorname
(Surname, first name)

Matrikel-Nr.
(Enrolment number)

Belehrung:

Wer vorsätzlich gegen eine die Täuschung über Prüfungsleistungen betreffende Regelung einer Hochschulprüfungsordnung verstößt, handelt ordnungswidrig. Die Ordnungswidrigkeit kann mit einer Geldbuße von bis zu 50.000,00 € geahndet werden. Zuständige Verwaltungsbehörde für die Verfolgung und Ahndung von Ordnungswidrigkeiten ist der Kanzler/die Kanzlerin der Technischen Universität Dortmund. Im Falle eines mehrfachen oder sonstigen schwerwiegenden Täuschungsversuches kann der Prüfling zudem exmatrikuliert werden, § 63 Abs. 5 Hochschulgesetz NRW.

Die Abgabe einer falschen Versicherung an Eides statt ist strafbar.

Wer vorsätzlich eine falsche Versicherung an Eides statt abgibt, kann mit einer Freiheitsstrafe bis zu drei Jahren oder mit Geldstrafe bestraft werden, § 156 StGB. Die fahrlässige Abgabe einer falschen Versicherung an Eides statt kann mit einer Freiheitsstrafe bis zu einem Jahr oder Geldstrafe bestraft werden, § 161 StGB.

Die oben stehende Belehrung habe ich zur Kenntnis genommen:

Official notification:

Any person who intentionally breaches any regulation of university examination regulations relating to deception in examination performance is acting improperly. This offence can be punished with a fine of up to EUR 50,000.00. The competent administrative authority for the pursuit and prosecution of offences of this type is the chancellor of the TU Dortmund University. In the case of multiple or other serious attempts at deception, the candidate can also be unenrolled, Section 63, paragraph 5 of the Universities Act of North Rhine-Westphalia.

The submission of a false affidavit is punishable.

Any person who intentionally submits a false affidavit can be punished with a prison sentence of up to three years or a fine, Section 156 of the Criminal Code. The negligent submission of a false affidavit can be punished with a prison sentence of up to one year or a fine, Section 161 of the Criminal Code.

I have taken note of the above official notification.

Ort, Datum
(Place, date)

Unterschrift
(Signature)

Titel der Dissertation:
(Title of the thesis):

Ich versichere hiermit an Eides statt, dass ich die vorliegende Dissertation mit dem Titel selbstständig und ohne unzulässige fremde Hilfe angefertigt habe. Ich habe keine anderen als die angegebenen Quellen und Hilfsmittel benutzt sowie wörtliche und sinngemäße Zitate kenntlich gemacht.
Die Arbeit hat in gegenwärtiger oder in einer anderen Fassung weder der TU Dortmund noch einer anderen Hochschule im Zusammenhang mit einer staatlichen oder akademischen Prüfung vorgelegen.

I hereby swear that I have completed the present dissertation independently and without inadmissible external support. I have not used any sources or tools other than those indicated and have identified literal and analogous quotations.

The thesis in its current version or another version has not been presented to the TU Dortmund University or another university in connection with a state or academic examination.*

*Please be aware that solely the German version of the affidavit ("Eidesstattliche Versicherung") for the PhD thesis is the official and legally binding version.

Ort, Datum
(Place, date)

Unterschrift
(Signature)

Contents

Abbreviations

°C	degree Celsius
a.u.	arbitrary units
aa	amino acids
Ab	antibody
Akt/PKB	protein kinase B
ATP	adenosine triphosphate
BCNK	bicyclo[6.1.0]non-4-yn-9-ylmethanol lysine
Bis-Tris	bis-(2-hydroxyethyl) aminotris (hydroxymethyl) methane
bp	base pair
BSA	bovine serum albumin
C-terminus	carboxyl terminus
ddH_2O	double distilled water
DMEM	Dulbecco's modified eagle medium
DMSO	dimethyl sulfoxide
DNA	deoxyribonucleic acid
DTT	dithiothreitol
e.g.	*exampli gratis*
ECD	extracellular ligand-binding domain
EDTA	ethylenediaminetetraacetic acid
EGF	epidermal growth factor
EGFR	epidermal growth factor receptor
ER	endoplasmatic reticulum
Erk	extracellular signal-regulated kinase
FCS	fetal calf serum
Fig.	figure
FLIM	fluorescence lifetime imaging microscopy
FP	fluorescent protein
FRET	Förster resonance energy transfer
HBSS	Hanks buffered salt solution
hr	hour
IP	immunoprecipitation

IRF	instrument response function
JNK	c-jun-N-terminal kinase
K	lysine
kb	kilo base pair
kD	kilo Dalton
l	liter
L-Glu	L-glutamine
LB	lysogeny broth
MAPK	mitogen-activated protein kinase
mCitrine	monomeric Citrine
MeOH	methanol
min	minute
ml	milliliter
mRNA	messenger RNA
N-terminus	amino-terminus
NEAA	non-essential amino acids
nm	nanometer
ns	nanosecond
PAGE	polyacrylamide gel electrophoresis
PBS	phosphate buffered saline
pH	*potentium hydrogenii*
PI3K	phosphoinositide-3-kinase
PM	plasma membrane
PMT	photomultiplier tube
ps	picosecond
PTB	phosphotyrosine binding
pY	phosphotyrosine
PVDF	polyvinylidene fluori
RNA	ribonucleic acid
RE	recycling endosome
ROI	region of interest
rpm	rounds per minute
RT	room temperature
RTK	receptor tyrosine kinase

s	second
SDS	sodium dodecyl sulphate
SEM	standard error of the mean
SH2	Src homology 2
TAE	Tris-acetate-EDTA
TBS	Tris buffered saline
TCSPC	time correlated single photon counting
tet	tetrazine
TKD	tyrosine kinase domain
Tris	Tris[hydroxymethyl]aminomethane
tRNA	transfer RNA
U	units
UAA	unnatural amino acid
UV	ultraviolet
V	volt
WT	wild type
Y	tyrosine
μ	micro
τ	lifetime
τ_{av}	average lifetime
τ_{D}	donor lifetime
τ_{DA}	donor-acceptor lifetime

Abstract

The dynamics of epidermal growth factor receptor (EGFR) signaling emerge from its recursive interactions with protein tyrosine phosphatases (PTPs) and autocatalytic receptor activation thereby determining cellular behavior including proliferation, migration and differentiation. The autocatalytic activation of EGFR causes an amplification of EGFR phosphorylation in response to extracellular signals, but its trade-off is spontaneous activation at high receptor densities even in the absence of ligand.

Structural and molecular dynamics studies identified an allosteric activation mechanism upon EGF-induced receptor activation, but the molecular basis of autocatalytic EGFR activation remains unclear. To better understand autocatalysis we developed a Förster Resonance Energy Transfer (FRET)-based, conformational EGFR indicator (CONEGI) using genetic code expansion to monitor the conformational state of the tyrosine kinase domain (TKD) in living cells and relate it to EGFR activity. We show that EGFR monomers can adopt an active conformation that is stabilized upon Y845 phosphorylation. Since Y845 is an auto-phosphorylation site this creates a positive feedback loop generating an autocatalytic amplification mechanism.

To counteract autonomous, autocatalytic EGFR activation in the absence of ligand, intrinsic and extrinsic safeguard mechanisms are required. Intrinsic auto-inhibitory structural features can be overcome by thermal conformational fluctuations allowing a sub-population of EGFR to adopt an active conformation. This autonomous, autocatalytic EGFR activity is counterbalanced by a spatial cycle that suppresses phosphorylation of Y845 on EGFR monomers by vesicular recycling through perinuclear areas with high PTP1B activity. EGF-binding induces receptor dimerization and phosphorylation of the c-Cbl docking Y1045 leading to receptor ubiquitination that targets EGFR for degradation in lysosomes. The re-routing regulates EGFR signaling response by the transit-time to late endosomes where it is switched-off by high PTP1B activity. This ubiquitin-mediated switch from a suppressive cycle to a unidirectional trafficking mode is a uniquely suited solution to suppress spontaneous activation while maintaining responsiveness to EGF.

Zusammenfassung

Die Signalweiterleitung nach Aktivierung des epidermalen Wachstumsfaktorrezeptors (EGFR) basiert auf ständigen Wechselwirkungen mit Proteintyrosinphosphatasen (PTPs) sowie der Fähigkeit von EGFR seine eigene Aktivierung zu amplifizieren. Dieses Zusammenspiel bestimmt zelluläre Prozesse wie Zellteilung, Zelldifferenzierung oder Zellmigration. Die EGFR-Selbstaktivierung vervielfacht die EGFR-Phosphorylierung nach Stimulierung mit Ligand, aber ermöglicht gleichzeitig spontane, ungewollte Aktivierung bei hohen Rezeptorkonzentration in Abwesenheit von Ligand.

Strukturelle und molekulardynamische Studien haben einen allosterischen Aktivierungsmechansimus nach Ligandenstimulierung identifiziert, jedoch wurde der molekulare Mechanismus der Amplifikation der EGFR-Selbstaktivierung bisher nicht entschlüsselt. Um diesen Mechanismus zu untersuchen, haben wir einen auf Förster Resonanz Energie Transfer (FRET)-basierenden EGFR Konformationssensor (CONEGI) mithilfe von genetischer Codeveränderung entwickelt, welcher es ermöglicht den Konformationszustand der Tyrosinkinasedomäne (TKD) zu beobachten und mit der Aktivität von EGFR zu korrelieren. Wir fanden heraus, dass EGFR-Monomere einen aktiven Konformationszustand annehmen können, der durch die Auto-Phosphorylierung von Y845 stabilisiert wird und eine Vervielfältigung der EGFR-Selbstaktivierung begünstigt.

Um die Eigenaktivierung von EGFR in Abwesenheit von Ligand zu unterbinden, existiert ein inhibierender, vesikulärer Transportkreislauf, der die Phosphorylierung von Y845 in EGFR-Monomeren durch kontinuierliches vesikuläres Recycling durch perinukleare Regionen mit hoher Phosphatase-Aktivität unterdrückt. Stimulierung mit EGF fördert die Dimerisierung von EGFR, die Phosphorylierung der c-Cbl-Bindestelle Y1045 und die Ubiquitinierung von EGFR, wodurch EGFR für den Abbau im Lysosom markiert wird. Diese Umleitung des vesikulären Transports reguliert die Aktivität von EGFR durch die Verweilzeit von EGFR in Endosomen bis das späte Endosom erreicht wird, wo die Rezeptoraktivität durch eine hohe PTP1B-Aktivität abgeschaltet wird. Diese Ubiquitin-abhängige Umleitung des vesikulären EGFR-Transports von einem inhibierenden Kreislauf in einen einseitig gerichteten Transportweg ermöglicht die Unterdrückung von ungewollter Eigenaktivierung und erhält gleichzeitig die Fähigkeit auf Stimulierung mit Ligand zu antworten.

1. Introduction

Living cells and organisms continuously perceive their environment in order to quickly adapt to a changing surrounding, e.g. different membrane integrated proteins including receptor tyrosine kinases (RTKs) transduce extracellular cues into intracellular signals. On the molecular level, signal transduction occurs through protein-protein interactions, conformational changes and posttranslational modifications. The activity of signaling proteins thereby depends on their local concentrations and counterbalancing activities that modulate or even prevent their activation. These dynamic factors generate spatio-temporal activity profiles of signaling proteins, which influence cellular responses. For a long time, it was thought that extracellular stimuli activate one signaling pathway, leading to a distinct cellular outcome. However, more recently it was shown that activation of the same signaling pathway by two different stimuli, epidermal growth factor (EGF) and nerve growth factor (NGF), in PC-12 cells leads to two distinct cellular fates. EGF signaling promotes a transient activation of mitogen-activated protein kinase (MAPK) inducing cell proliferation, while NGF stimulation triggers cell differentiation via sustained MAPK activation[1]. This example demonstrates that signaling pathways are highly interconnected and form complex and dynamic signaling networks using positive and negative feedback loops that process and integrate information. The RTK epidermal growth factor receptor (EGFR) is known as a key node in such signaling networks and aberrant EGFR activity was linked to tumor development. Ligand-induced allosteric dimer formation results in receptor activation and trans-phosphorylation of regulatory and signaling tyrosine residues in the C-terminal tail that serve as docking sites for adaptor proteins. Phosphorylated EGFR is internalized and traffics through perinuclear areas with high protein tyrosine phosphatase (PTP) activity to terminate EGFR signaling before receptor degradation in lysosomes. The promotion or termination of EGFR signaling, which determines signal amplitude and duration, is therefore influenced on many levels including conformational states, local protein concentrations and vesicular trafficking dynamics.

1.1. Family of receptor tyrosine kinases (RTKs)

1.1.1. RTK family and history

RTKs belong to the family of protein tyrosine kinases and because of their plasma membrane (PM) localization, they are key players in signal transduction from the cell exterior to the cell interior. They act as key regulators to determine cell fate including proliferation, migration, differentiation, survival, metabolism and cell cycle control. Aberrant activation of RTKs through overexpression or oncogenic mutations is associated with the development and progression of several cancer types making them an important target for cancer research. To date 58 human RTKs have been identified, which are classified in 20 subfamilies[2]. The shared topology among RTKs includes an extracellular, ligand-binding domain, a single-pass transmembrane domain and a cytosolic domain including a tyrosine kinase domain (TKD) (**Fig.1**).

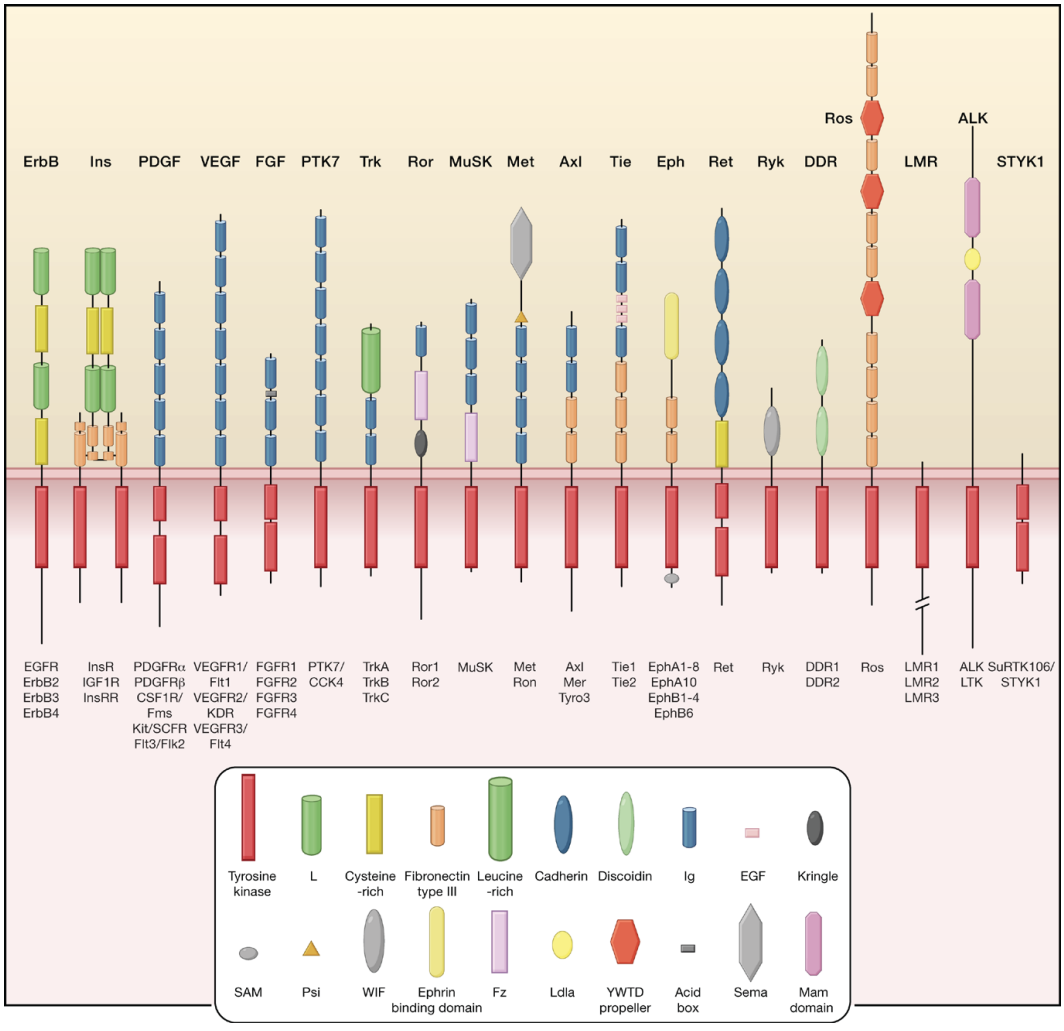

Figure 1: Family of receptor tyrosine kinases. Schematic representation of the 20 subfamilies of RTKs with the name of each receptor listed below. The different domains of the extracellular and cytosolic part are indicated in the key[2].

RTK activation has been ascribed to receptor dimerization induced by growth factor binding[3]. However, some RTKs exhibit more complex activation mechanisms, e.g. the insulin receptor and the IGF1 receptor exist as pre-dimers that undergo conformational changes upon ligand binding[4], whereas Eph receptors require higher-order clustering for activation[5]. The active TKD conformation displays similarities among most RTKs, while inactive conformations vary substantially[6] suggesting different activation mechanisms caused by distinct inhibitory structural features in the absence of ligand. Key regulatory structural elements in the activation mechanism of all RTKs, including the αC-helix in the N lobe and the activation loop in the C lobe of the TKD, undergo substantial conformational changes upon receptor activation to stabilize the active conformation[7–10]. If required, the juxtamembrane segment and the C tail can also play a major role in regulation of RTK activity[7,11,12]. Following receptor activation, auto-phosphorylation of specific tyrosine residues on the C-terminal tail results in recruitment of adaptor proteins bearing Src Homology 2 (SH2) and phosphotyrosine binding (PTB) domains, thereby activating downstream signaling, which is then modulated by counteracting activities of protein tyrosine phosphatases (PTPs) that remove tyrosine phosphorylation.

1.1.2. ErbB subfamily of RTKs

One subfamily among RTKs is the ErbB receptor family, which has been linked to oncogenic transformation, especially in lung and breast cancer[13,14]. This family of RTKs consists of four members: EGFR (ErbB1/HER1), ErbB2 (HER2, Neu), ErbB3 (HER3) and ErbB4 (HER4). All ErbB family members and their progenitors are ubiquitously expressed in epithelial, neuronal and mesenchymal tissues[15]. Whereas EGFR plays a crucial role in epithelial development in lung, skin and gastrointestinal tract, ErbB2, ErbB3 and ErbB4 are involved in the cardiac muscle and central nervous system development[16–20].

Ligand binding to ErbB receptors induces homo- or hetero-dimerization resulting in phosphorylation of tyrosine residues in the C-terminal tail thereby initiating downstream signaling. Whereas EGFR and ErbB4 can form homo-dimers and hetero-dimers with other family members, activation of ErbB2 and ErbB3 depends on hetero-dimer formation, because of missing ligands (ErbB2) or the lack of intrinsic kinase activity (ErbB3). Seven ligands that activate EGFR have been identified so far: epidermal growth factor (EGF), transforming growth factor α (TGF α), betacellulin (BTC), epiregulin (EPR), epigen (EGN), amphiregulin (ARG) and heparin-binding EGF-like growth factor (HB-EGF)[21].

Stimulation with these ligands induces transient or sustained EGFR activation which promotes different cellular outcomes, demonstrating biased agonism through the induction of different active conformations leading to different dimer strength[22]. BTC, EPR and HB-EGF as well as neuregulins (NRGs) activate ErbB4, whereas ErbB3 can only be activated by NRGs[23,24].

1.2. Epidermal growth factor receptor (EGFR)

1.2.1. Physiological relevance of EGFR signaling

EGFR has been implicated in numerous physiological processes including embryonic development, wound healing, and tissue homeostasis[25,26]. Mice lacking EGFR showed growth retardation and die within twenty days after birth due to a host of defects, including gross abnormalities in bones, brain and heart tissue. Furthermore, epithelial development is impaired in many organs such as lung, skin, eyes, hair follicles and gastrointestinal tract, often resulting in the animals death[19,20]. EGFR signaling is distinct and opposed in different cell types and tissues. Whereas EGFR is involved in survival signaling in cortical astrocytes in the brain, EGFR signaling negatively regulates premature differentiation of keratinocytes in the epidermis[20,27,28] or of osteoblasts and chondrocytes in bone development[29,30]. In contrast, EGFR activation favors differentiation of mesenchymal cells in semilunar valves in the heart and of type II pneumocytes in the lung[20,29,31,32] and controls cell proliferation and cell-cycle entry after tissue injury in hepatocytes[33]. The different roles of EGFR signaling in these cellular processes demonstrate the complexity of the EGFR signaling network requiring fine-tuned spatio-temporal regulation of EGFR activity for context-dependent cellular responses.

1.2.2. Structural insight into EGFR and its activation mechanism

EGFR consists of an extracellular ligand-binding domain (ECD), a single-pass transmembrane domain and a cytosolic domain consisting of a juxtamembrane segment, the tyrosine kinase domain (TKD) and a regulatory C-terminal tail with several tyrosine residues that serve as docking sites for adaptor proteins upon their phosphorylation. The EGFR TKD exhibits a bilobate structure with an N lobe that contains five β sheets (β1- β5) and one α helix (αC-helix) and a C lobe consisting of multiple α helices and the activation

loop (**Fig.2**). Both lobes are connected via a short hinge region that harbors the catalytically active site.

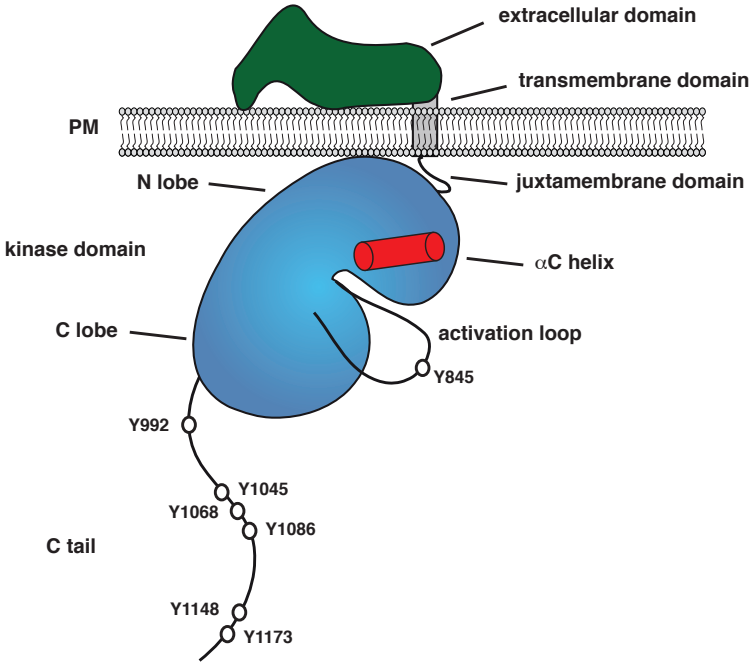

Figure 2: Schematic representation of the EGFR structure. A single transmembrane domain connects the extracellular ligand-binding domain with the cytosolic part of EGFR. The cytosolic domain is further separated to the juxtamembrane segment, the tyrosine kinase domain with the αC-helix and activation loop, and the C-terminal tail with several tyrosine residues.

In the absence of ligand, several structural features regulate EGFR activity and lock EGFR in an inactive conformation to avoid spurious activation, these are: 1) The ECD, which consists of four subdomains (I-IV), adopts a tethered, auto-inhibited conformation in which subdomain II and IV are held together[34]. 2) Two polybasic stretches, one in the juxtamembrane segment (LRRLL motif) and the other in the kinase domain (polybasic stretch: K689, K692, K713, K715), which are associated with the negatively charged PM, stabilize the inactive conformation[35,36]. 3) Local disorder in the αC-helix in the C lobe of the kinase domain increases the threshold for EGFR kinase activation[10]. 4) The C-terminal tail interacts via its LLSSL motif with the dimerization interface of the TKD in the inactive conformation and prevents EGFR activation[12].

EGF-binding to subdomain I and III of the ECD, opens the tethered conformation and exposes the 'dimerization arm' of subdomain II[34]. Coupling of the extracellular module with the cytosolic domain via the transmembrane domain leads to intracellular conformational changes resulting in the allosteric activation of the EGFR TKD[37]. The transmembrane domains thereby form an N-terminal dimer and release the juxtamembrane

segments from the PM. Subsequent formation of an antiparallel helix dimer of the juxtamembrane segments promotes dissociation of the TKDs from the PM and asymmetric dimer formation (**Fig.3**). In the asymmetric dimer one receptor acts as an 'activator' kinase and the other one serves as a 'receiver' kinase.

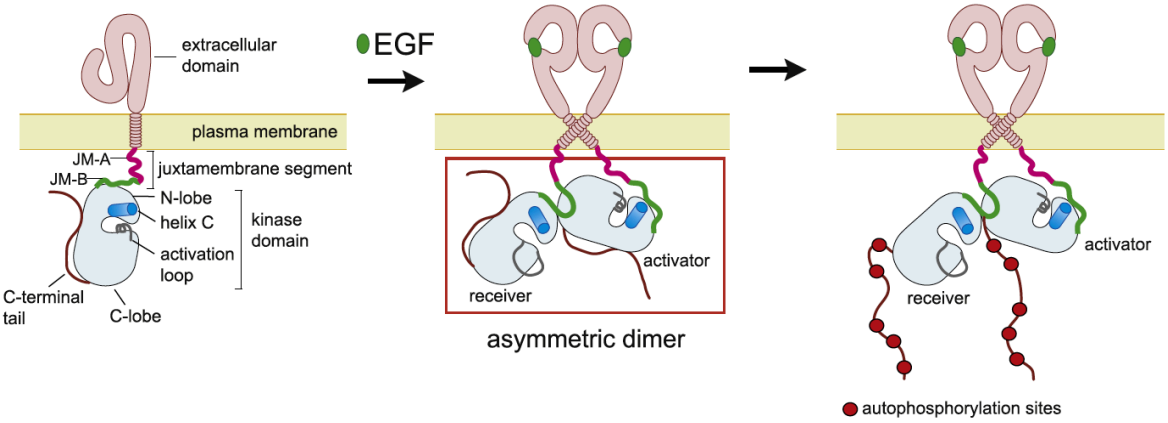

Figure 3.: Allosteric EGFR activation mechanism. Ligand binding to EGFR results in the formation of an asymmetric dimer, where one receptor acts as an 'activator' and the second one as a 'receiver'. Tyrosine phosphorylation at the C tail of the 'receiver' kinase can only occur if the receptors dynamically change their positions[38].

This ligand-induced EGFR activation is controlled by conformational changes in the αC-helix and the activation loop of the EGFR TKD that stabilize the active kinase conformation in the asymmetric dimer. The αC-helix moves from its 'out'-configuration to an ordered 'in'-configuration (**Fig.4**), while sampling intermediate states during the transition[10,39]. The 'in'-conformation of the αC-helix maintains a catalytically important salt bridge between K721 and E738 that is required for the coordination of the α- and β-phosphate group of the substrate ATP molecule and subsequent phosphate transfer. Disrupting the salt bridge, e.g. by a K721A mutation, results in loss of kinase activity. Furthermore, to adopt the active conformation the activation loop frees the catalytic cleft for ATP binding (**Fig.4**) and the C-terminal tail dissociates from the dimerization interface of the TKDs[12] allowing the formation of the asymmetric dimer.

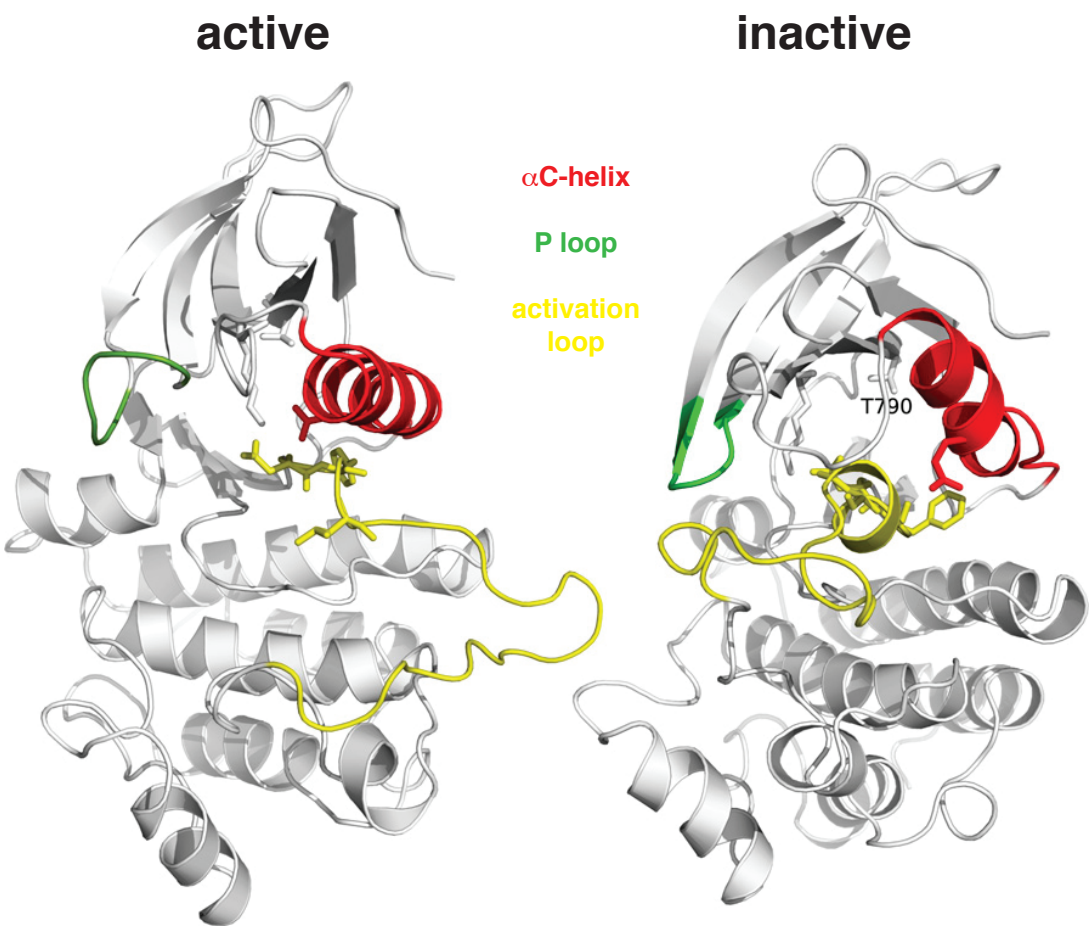

Figure 4: Crystal structures of the active (left) and inactive (right) EGFR kinase domain. The αC-helix is marked in red, the activation loop in yellow and the P loop in green[40].

In addition, hydrophobic interaction between residues P675, L680, I682 and L736 in the C lobe of the 'activator' kinase and I917, M921, V924 and M928 in the N lobe of the 'receiver' kinase are essential for dimerization and stabilize the asymmetric dimer. Point mutations (I682Q, V924R) disrupt the dimerization interface and generate dimerization-impaired EGFR mutants. The I682Q mutation thereby restricts EGFR to serve as the 'activator' kinase, whereas the V924R mutation limits EGFR to act as the 'receiver' kinase. In the functional asymmetric dimer the 'activator' kinase locks the 'receiver' kinase in an active conformation and then the 'receiver' kinase trans-phosphorylates tyrosine residues Y992, Y1045, Y1068, Y1086, Y1148 and Y1173 at the C-terminal tail of the 'activator' kinase[37]. These phosphorylated tyrosine residues serve as docking sites for adaptor proteins containing SH2 or PTB domains that specifically recognize phosphor-tyrosines[41] and facilitate effector protein binding, leading to the activation of downstream signaling cascades including Ras-Raf-MEK-ERK1/2, STAT or PI3K-Akt-mTOR pathway, which control e.g. cell proliferation, differentiation or survival[42]. Importantly, EGFR

signaling is not only restricted to the PM, but also occurs from endosomes, which serve as additional signaling platforms in the cell interior[43,44].

Recently, however, higher-order EGFR oligomerization, which has been observed for a decade[45–47], was suggested to be required for auto-phosphorylation on distal tyrosine residues in the C-terminal tail and downstream activation of phosphatidyl inositol 3-kinase (PI3K)[48]. The molecular mechanism of higher-order clustering is supposed to be based on further dimerization of EGF-bound dimers via their multimerization motifs in subdomain IV of the ECD, thereby building chains of asymmetric dimers (**Fig.5**). In these receptor oligomers, one receptor adopts the 'off' state acting as the 'activator', while all other kinases are assumed to be active. Since higher-order clustering has also been shown in the activation processes of other RTKs (e.g. the Eph receptor family)[5], it may represent a general mechanism for RTK activation.

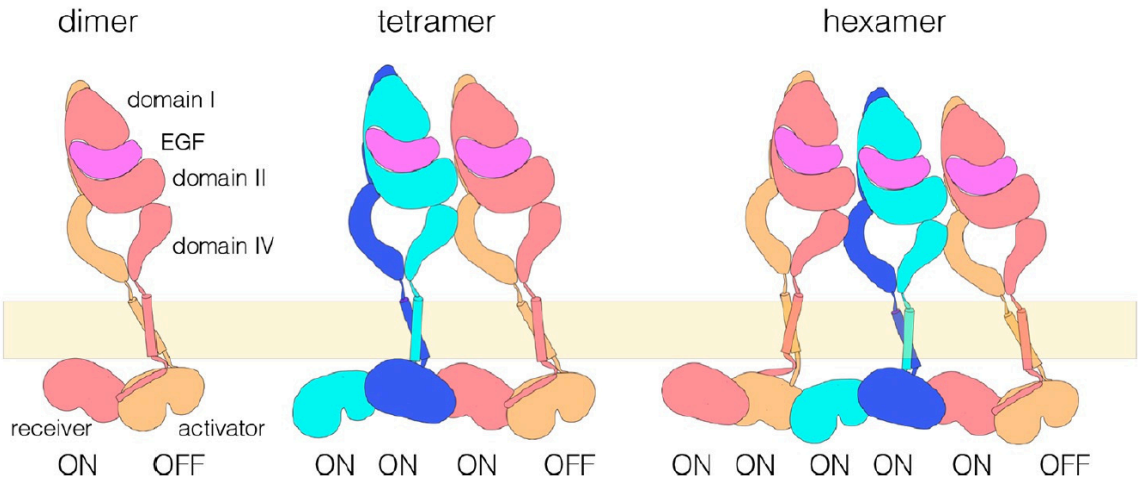

Figure 5: Model for EGFR multimerization. Higher-order oligomers are generated by dimerization of dimers building a chain of kinase domains. The first kinases are assumed to be in the 'ON' state, while the last one is inactive[48].

However, despite its structural auto-inhibitory features spontaneous EGFR activation has been observed in the absence of ligand[49] especially at high receptor concentrations (e.g. in different types of cancer that overexpress EGFR[50]). To overcome this auto-inhibition, thermal conformational fluctuations are required that enable a subpopulation of receptors to adopt an active conformation. Such a two state equilibrium has been postulated for the fibroblast growth factor receptor (FGFR) and could also exist for EGFR and other RTKs[2,51]. Recently, structural and molecular dynamics simulations suggested that Y845 phosphorylation in the activation loop suppresses the intrinsic disorder in the αC-helix, thereby stabilizing the active conformation[10]. If this active conformation further catalyzes

Y845 phosphorylation on other EGFR molecules, thereby further stabilizing EGFR molecules in an active conformation, this would provide the basis for autocatalytic amplification of EGFR activity[49,52]. However, whether EGFR autocatalysis induced by Y845 phosphorylation enhances EGFR dimerization affinity or is based on another molecular mechanism is unclear.

1.2.3. EGFR activation coupled to PTP inhibition

The canonical view of EGFR signaling implies that EGFR phosphorylation activates a linear downstream pathway leading to a distinct cellular response. However, EGFR harbors several phosphorylation sites that recruit multiple adaptor and effector proteins, creating a large number of activated signaling molecules. This suggests that EGFR participates in multiple signaling pathways that are highly interconnected, creating a complex and dynamic signaling network that controls the spatial-temporal activity of signaling molecules[2]. The interplay of RTKs and protein tyrosine phosphatases (PTPs) is a good example for how different network topologies such as positive and negative feedback loops can shape cellular behavior by determining signal amplitude and duration[53–57]. PTPs including membrane-localized receptor-type PTPs (RPTPs), the cytosolic Shp1 and Shp2 and the endoplasmatic reticulum (ER)-anchored PTP1B and TCPTP, counteract growth factor mediated EGFR phosphorylation[58–64]. However, the high catalytic activities of PTPs (~two orders of magnitude higher than EGFR) would suffice to not only suppress spontaneous but also ligand-induced EGFR phosphorylation[65,66]. Multiple mechanisms are used to overcome this challenge in EGFR activation. The counterbalancing activities of RTKs and PTPs are spatially separated in the cell, enabling EGF-mediated EGFR activation at the PM, while ER-anchored PTP1B dephosphorylates ligand-stimulated, internalized EGFR mainly in pericentriolar areas where PTP1B exhibits its highest activity[67]. Furthermore, EGFR activation can be coupled to PTP inhibition in a reaction-diffusion network through the local production of reactive oxygen species (ROS) by NADPH oxidases at the PM[49,54,68]. ROS such as hydrogen peroxide (H_2O_2) are fast diffusing second messenger molecules that inhibit PTPs by reversible oxidation of the catalytic cysteine thiolate to a sulfenic acid[69]. Substantial cell damage is prevented through fast ROS degradation by catalases. The resulting short half-life of ROS generates a ROS gradient from the PM towards the cell interior. However, the local production of ROS suffices to inhibit nearby PTPs and to lower the activation threshold for neighboring EGFR

molecules[54]. Due to the EGFR activity-dependent ROS-mediated PTP inhibition[70,71], the negative feedback of PTPs on EGFR converts into a double negative feedback, which can be considered as a positive feedback amplifying EGFR phosphorylation (**Fig.6A,B**). This toggle switch in the EGFR-PTP network creates a bistable system that responds in a switch-like behavior between only two possible states, a 'resting state' and an 'active state'[49] (**Fig.6C**). Exceeding a threshold concentration of ligand induces EGFR phosphorylation, which can be preserved even if the ligand concentration returns to concentrations below the threshold. This creates a range of ligand doses, in which EGFR can either be switched on or off depending on its actual state. Such property in a system has also been observed for mitosis promoting factor (MPF) in frog eggs showing that bistability is a general feature in cellular signaling networks[72].

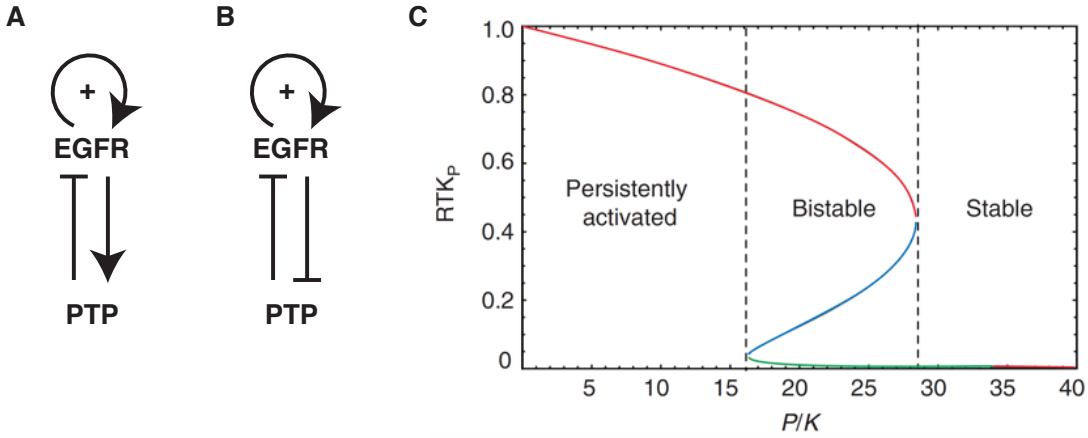

Figure 6: RTK and PTP reaction network. A. Negative feedback between EGFR and PTP. **B.** RTK activation coupled to PTP inhibition by ROS creates a double negative feedback loop. Together with the autocatalytic activity of the RTK the systems becomes bistable. **C.** The fraction of phosphorylated RTK (pRTK) at steady state is plotted as a function of the relative maximal PTP to RTK activity (P/K). The red and green lines represent stable states, whereas the blue line indicates the region where green and red lines coincide resulting in an unstable saddle point. In this region the system is bistable[49].

1.3. Rab proteins in vesicular EGFR trafficking

The endocytic machinery regulates the duration of EGFR signaling after ligand activation by controlling balance of the rate between EGFR degradation versus recycling. Small Rab GTPases are key players in vesicular trafficking processes that control formation and fusion of vesicles. Like other GTPases, Rab proteins switch between a GDP-bound 'off' and a GTP-bound 'on' state mediated by guanine nucleotide exchange factors (GEFs) and GTPase-activating proteins (GAPs) (**Fig.7**). The more than 60 members of Rab proteins are specifically and reversibly associated with the membrane of specific intracellular compartments by one or two geranylgeranyl groups[73]. Newly synthesized GDP-bound Rabs are captured by Rab escort proteins (REPs) and transported to the geranylgeranyl

transferases[74]. This allows GDP dissociation inhibitors (GDIs) to recognize cytosolic geranylgeranyl GDP-bound Rab and deliver it to the cognate membrane[75]. For this, GDI displacement factors (GDFs) have been suggested to confer specificity to Rab membrane association by recognizing specific Rab-GDI complexes[76].

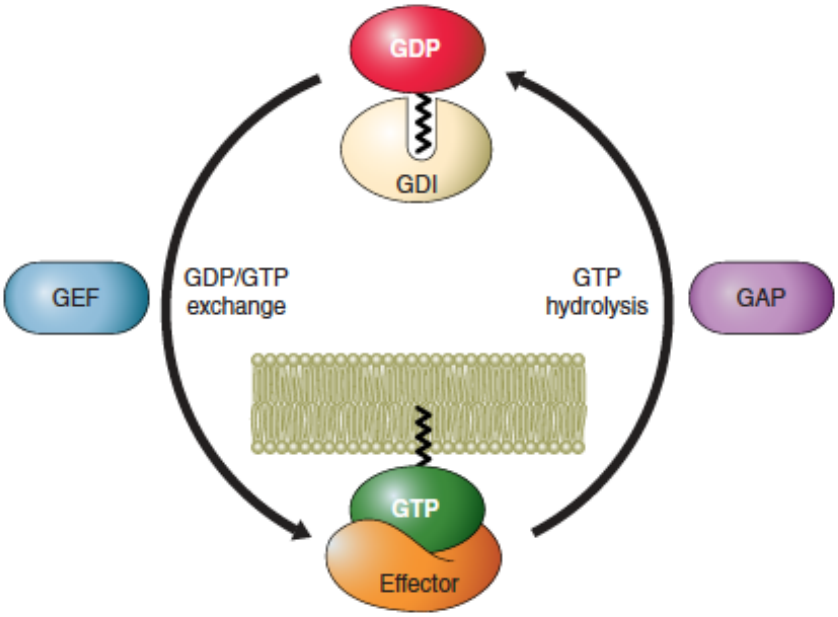

Figure 7: The Rab GTPase cycle. Rab conversion between a GDP-bound and a GTP-bound state is mediated by GDP/GTP exchange factors (GEFs) and GTPase-activating proteins (GAPs). The GTP-bound state interacts with effector molecules[77].

Ligand-activated phosphorylated EGFR internalizes via clathrin-mediated endocytosis (CME) upon low ligand doses or clathrin-independent endocytosis (CIE) at high ligand concentrations due to saturation of CME[78]. On the way from the PM to the cell interior, small clathrin coated vesicles (CCVs) loaded with EGFR fuse to Rab5-positive early endosomes (EEs)[79]. From EEs, EGFR is either targeted to Rab7-positive late endosomes (LEs), dephosphorylated in pericentriolar areas with high PTP1B activity and subsequently committed to LAMP1-positive lysosomes for degradation or recycled back to the PM via the Rab4-positive fast recycling endosome (RE) or the Rab11-positive pericentriolar slow RE[67,80–84] (**Fig.8**). One important factor determining receptor fate is receptor ubiquitination mediated by the E3-ubiquitin ligase c-Cbl[80,85]. c-Cbl binds EGFR either directly at phosphorylated Y1045 via its tyrosine binding domain or indirectly through Grb2, which binds EGFR at phosphorylated Y1068 and Y1086 via its SH2 domain[86,87]. EGF-induced, c-Cbl-mediated EGFR ubiquitination is governed by a threshold-controlled mechanism that allows a cell to regulate the balance between EGFR signaling persistence and termination[88]. Sorting of ubiquitinated EGFR into multivesicular bodies (MVBs) that are

formed by the invagination of endosomal membranes after recruitment of the ESCRT complex[89,90] commits the receptor subsequently to lysosomes for degradation[80]. The transport of receptors from LEs to lysosomes is ensured by temporal fusion of both compartments leading to cargo exchange. Subsequent fission terminates the so-called 'kiss and run' event[91]. However, despite studies on vesicular trafficking of EGFR after ligand stimulation, it is not clear whether and how vesicular constitutive trafficking regulates EGFR activity in the absence of ligand.

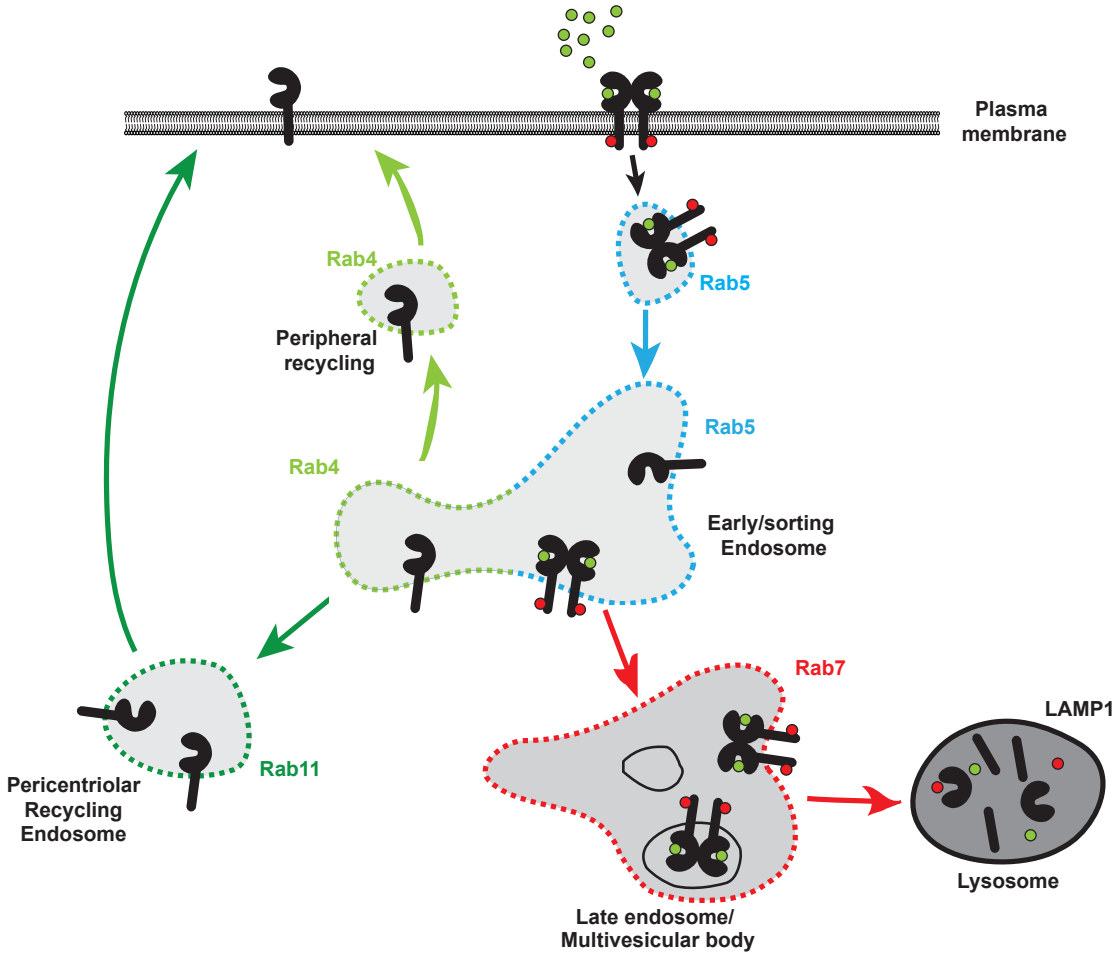

Figure 8: Vesicular trafficking of EGFR upon EGF stimulation. Ligand-bound EGFR is internalized and either recycled back to the PM via peripheral or pericentriolar recycling or targeted to lysosomes for degradation. The indicated Rab GTPases are specific for the different endosomal compartments and involved in endosomal fusion and fission events.

1.4. Fluorescence as a tool to study protein functions

1.4.1. Fluorescence microscopy

Since the discovery of the green fluorescence protein (GFP) in the jellyfish, *Aequorea victoria*, in 1962 by Shimomura fluorescence microscopy emerged as an important tool in natural sciences to observe and measure cellular processes that had previously been invisible[92]. Fluorescence occurs upon the emission of photons from electrons relaxing from an excited singlet state to the ground state usually illustrated in a Jablonski diagram that depicts the processes of absorption and emission of light (**Fig.9**). Emission rates of fluorescence are rapid, typically in the range of nanoseconds. Although the ground state S_0 as well as the higher order singlet states S_1 and S_2 exhibits multiple vibrational energy levels, absorption and emission occur mostly from the lowest vibrational level. Following light absorption, an electron is elevated from the ground state $S_{0,0}$ to higher vibrational levels of the singlet states S_1 or S_2. Due to internal conversion, molecules relax non-radiatively, in a rapid process to the lowest vibrational level of S_1 ($S_{1,0}$) causing an emission shift to lower energies (Stoke shift). From the $S_{1,0}$ state electrons either relax back to the ground state S_0 by emission of a photon or molecules undergo a spin conversion to the first triplet state T_1 called intersystem crossing. Emission from T_1, termed phosphorescence, lasts several orders of magnitude longer than fluorescence due to the shift to lower energy.

The fluorescence lifetime τ_D describes the time an electron remains in the excited state before relaxation to the ground state and is defined by the following equation:

$$\tau_D = \frac{1}{k_F + k_{IC} + k_{IS}}$$

with k_F being the fluorescence emission and, k_{IC} (internal conversion) and k_{IS} (intersystem crossing) being non-radiative transitions.

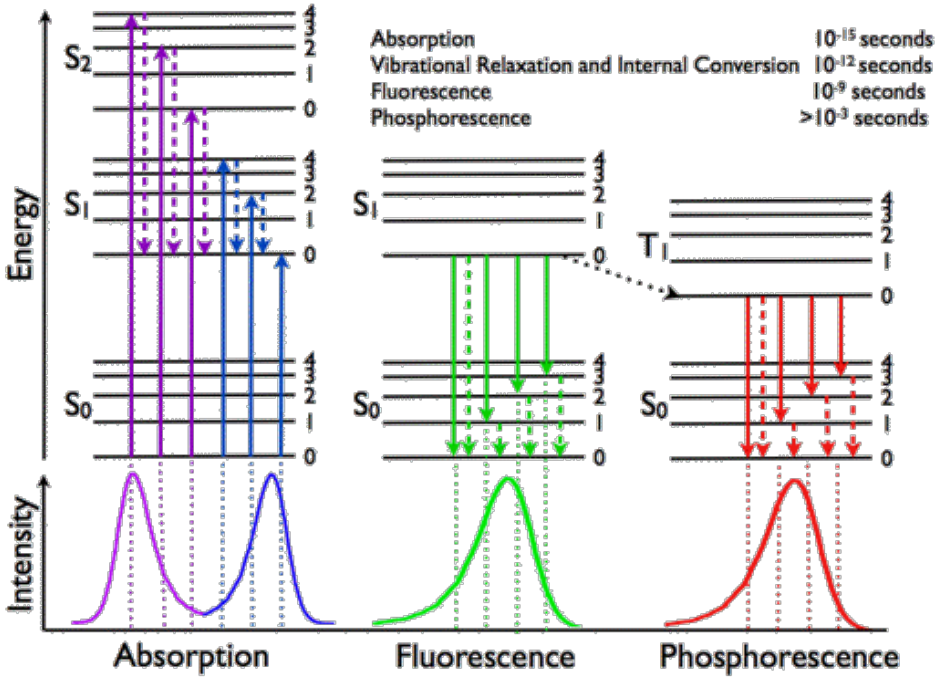

Figure 9: Jablonski diagram. Following light absorption electrons from the ground state S_0 are excited to a higher vibrational level of the first two excited singlet states S_1 and S_2 (solid, blue arrows). Due to internal conversion molecules relax to the lowest vibrational level of $S_{1,0}$ (dashed, blue arrows). From the S1,0 state molecules either emit a photon and relax back to the ground state (solid, green arrows) or undergo a non-radiative intersystem-crossing transition (dashed, black arrow) leading to phosphorescence (solid, red arrows) (http://photobiology.info/Visser-Rolinski_files/Fig4.png; 30.08.2016).

1.4.2. FRET/FLIM

Förster resonance energy transfer (FRET) is a powerful research tool to detect intermolecular interactions and measure distinct conformational states by using the property of non-radiative energy transfer between two fluorescent proteins/fluorophores that are in close proximity to each other. For this, the emission spectrum of the donor fluorophore needs to overlap with the excitation spectrum of the acceptor fluorophore. FRET is non-radiative process, meaning that it does not result from reabsorption of donor emission by the acceptor, occurs in the excited state of a fluorophore and only depends on dipole-dipole interactions of donor and acceptor. The efficiency of energy transfer is dependent on the donor fluorescence lifetime τ_D, the Förster radius R_0 of the FRET pair and the distance r between donor and acceptor. The extent of the energy transfer k_{FRET} is given by:

$$k_{FRET} = \frac{1}{\tau_D}\left(\frac{R_0}{r}\right)^6$$

The Förster radius R_0 of a FRET pair represents the distance between donor and acceptor at which the FRET efficiency is half-maximal. Commonly used FRET pairs exhibit a R_0 of around 5-6 nm that can be calculated by the following equation:

$$R_0 = 0.211\ (\kappa^2 n^{-4} Q_D J(\lambda))^{1/6}$$

where *n* is the refractive index of the medium, Q_D the quantum yield of the donor, J(λ) the spectral overlap integral between donor emission and acceptor absorption and κ^2 the dipole-dipole orientation factor that is usually assumed to be 2/3. Parallel dipole-dipole orientation would allow for maximum FRET, whereas perpendicular orientation prevents FRET. To create a high dynamic range for a FRET measurement, the distance r between donor and acceptor needs to be close to R_0 (**Fig.10**), so that minimal changes in the distance or orientation can lead to a substantial decrease or increase in FRET efficiency. The FRET efficiency E is given by:

$$E = \frac{R_0^6}{R_0^6 + r^6}$$

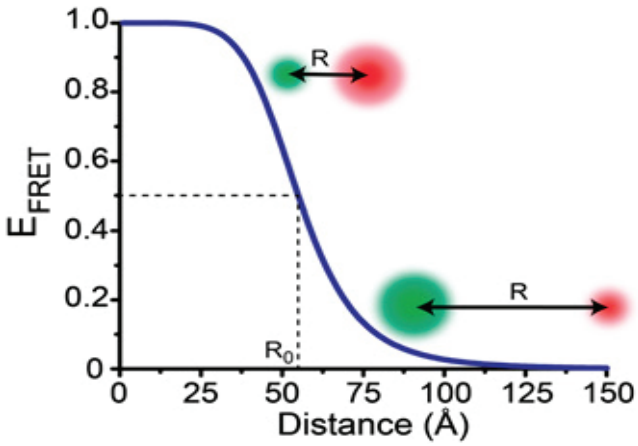

Figure 10: FRET efficiency. The FRET efficiency (E_{FRET}) as a function of the distance between donor (green sphere) and acceptor fluorophore (red sphere). R_0 indicates the distance where $E_{FRET} = 0.5$ [93].

FRET k_{FRET} decreases the excited state lifetime τ_D of the donor as an additional non-radiative process and is added to the sum of transition rates:

$$\tau_D = \frac{1}{k_{FRET} + k_F + k_{IC} + k_{IS}}$$

The FRET efficiency can be determined experimentally by measuring the donor fluorescence intensity (I) or lifetime (τ) in the presence and absence of acceptor:

$$E = 1 - \frac{I_{DA}}{I_D} = 1 - \frac{\tau_{DA}}{\tau_D}$$

Both, intensity-based and fluorescence lifetime imaging techniques have been developed to detect FRET. Intensity-based measurements range from acceptor photobleaching, ratiometric imaging or sensitized emission, whereas lifetime measurements can be performed by time-domain FLIM and frequency-domain FLIM[94]. FLIM is independent of donor concentrations, robust to intensity fluctuations and allows the calculation of the donor fraction that undergoes FRET, but its trade-off is the low temporal resolution due to the long acquisition time.

1.4.3. Optical sensors obtain RTK activity and conformation

The development of optical sensors based on one fluorescent protein/fluorophore or FRET between two fluorescent proteins/fluorophores produced a massive toolbox to measure location, concentration, activity or conformation of key players in cellular signaling including lipids, ions and enzymes[95]. This was achieved by using a variety of fluorescent proteins that can be genetically encoded in a protein of interest, preferentially at the N- or C-terminal end, or by attaching small organic fluorophores to a protein via SNAP- or CLIP-tags, cysteine motifs or using genetic code expansion in conjunction with bioorthogonal labeling chemistry[96–100]. In combination with high-end microscopy, this nowadays enables monitoring of cellular responses with high spatial and temporal precision. A couple of FRET-based biosensors have been designed that either approach to investigate the enzymatic activity of RTKs or aim to monitor different conformational states of RTKs. The development of biosensors measuring substrate phosphorylation, for example the Picchu[101] and the FLAME sensor[102], revealed information about the spatial-temporal phosphorylation profiles of EGFR. In addition, conformational sensors detecting intramolecular movements e.g. in the extracellular domain of EGFR, the C-terminal tail of EGFR, the juxtamembrane segment of EphA2 or key structural elements in the FGFR TKD provided insight in the activation mechanisms of these RTKs, which have been proposed by structural studies[103–106]. Such conformational sensors allow relating the conformational state of a given RTK to its activity thereby enabling a better understanding

of the collective activation dynamics especially when the monitored regions are involved in the regulation of kinase activity.

1.4.4. Genetic code expansion as a tool for protein labeling

The incorporation of genetically encoded unnatural amino acids (UAA) at defined sites into proteins of bacteria, yeast, mammalian cells, *C.elegans*, *D.melanogaster* and the mouse brain has emerged as a useful biological tool in recent years[107–110]. Genetic code expansion requires an orthogonal tRNA synthetase/ tRNA pair such as the pyrrolysyl-tRNA synthetase/ tRNA pair from *Methanosarcina* species that incorporates an UAA in the polypeptide chain during mRNA translation, in response to an amber codon (UAG) placed at a user-defined site in a gene of interest (**Fig.11**).

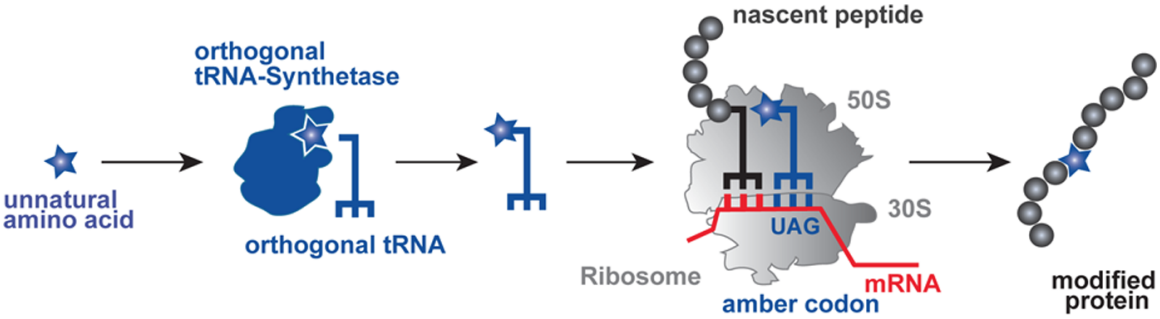

Figure 11: Genetic code expansion. The incorporation of an unnatural amino acid into a protein of interest requires an orthogonal tRNA synthetase/tRNA system. In response to an amber codon (UAG) at a user-defined site in a gene of interest the unnatural amino acid is incorporated into the polypeptide chain during translation[111].

To date more than 100 UAA have been developed for different applications including UAAs with post-translational modifications[112,113], light-inducible, photocaged UAAs[114–117], or UAAs that can be labeled with fluorophores via fast bioorthogonal reactions. For example, labeling of the UAA bicycle[6.1.0]nonyne-lysine (BCNK) incorporated in intracellular proteins was shown to be highly specific using superresolution microscopy[118]. BCNK contains a strained alkyne functional group, which is capable of undergoing an inverse electron-demand Diels-Alder cycloaddition with a tetrazine-fluorophore conjugate in an efficient and biocompatible way, enabling protein labeling in living cells[119] (**Fig.12**). The advantage in using UAA incorporation and bioorthogonal chemistry to attach a fluorophore lies in their small size as compared to larger fluorescent proteins allowing fluorescence labeling at nearly any site in a protein of interest even in key functional regions of protein kinases such as FGFR[106].

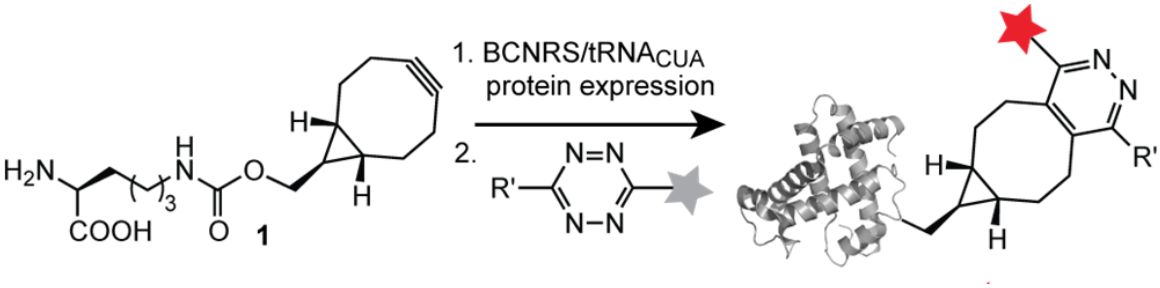

Figure 12: Fluorogenic labeling of unnatural amino acids. The strained alkyne functional group of BCNK reacts with a tetrazine-fluorophore conjugate in a fast bioorthogonal reaction (inverse-electron-demand Diels-Alder cycloaddition)[119].

2. Objectives

Autocatalytic EGFR activation enables diverse, context-dependent responses to extracellular cues, but its trade-off is the generation of uncontrolled autonomous EGFR phosphorylation even in the absence of ligand[35,49]. Autonomous EGFR activation occurs if a subpopulation of receptors overcomes structural auto-inhibition and adopts an active conformation resulting in receptor phosphorylation due to transient interactions especially at high receptor densities. These auto-phosphorylation events can trigger an autocatalytic activation mechanism when they stabilize an active conformation of the EGFR TKD. Y845 phosphorylation was suggested to stabilize the active conformation, but the exact molecular mechanism of autocatalytic EGFR activation is unclear. Moreover, extrinsic safeguard mechanisms that regulate autocatalytic EGFR activity are required to suppress spontaneous, uncontrolled EGFR activation while still permitting robust responses to growth factors. One way to regulate autonomous EGFR activity would be to control its spatial distribution through regulation of vesicular trafficking, since ligand-activated internalized EGFR is efficiently dephosphorylated by ER-anchored PTP1B, which exhibits its highest activity in pericentriolar areas[67]. The following goals will be addressed to investigate the autocatalytic activation mechanism and the regulation of autonomously, autocatalytic activated EGFR:

1. Structural and molecular dynamics studies captured snapshots of active and inactive EGFR conformations and identified an allosteric activation mechanism, but it is unclear how autocatalytic activation enhances EGFR activation. To gain more insight in EGFR autocatalysis a FRET-based EGFR sensor will be developed to monitor conformational states of the EGFR TKD and relate them to EGFR activity and self-association. I will investigate which EGFR species mediates autocatalytic activation and if Y845 phosphorylation affects the autocatalytic amplification.

2. To date it is unclear how autonomous autocatalytic EGFR activity is regulated. Therefore, I investigate the role of vesicular trafficking in the regulation of autonomously activated EGFR, how a cell differentiates between autonomous and ligand-dependent activated EGFR and which factors are important for differential sorting of activated EGFR.

3. Material and Methods

3.1. Materials

3.1.1. Chemicals and reagents

Ammonium persulfate (APS)	SERVA Electrophoresis GmbH
BCNK	Synaffix
2'-deoxyadenosine-5'-triphosphate (dATP)	Invitrogen™ Life Technologies
2'-deoxycytidine-5'-triphosphate (dCTP)	Invitrogen™ Life Technologies
2'-deoxyguanosine-5'-triphosphate (dGTP)	Invitrogen™ Life Technologies
2'-deoxythymidine-5'-triphosphate (dTTP)	Invitrogen™ Life Technologies
Dimethylsulfoxid (DMSO)	SERVA Electrophoresis GmbH
Dithiothreitol (DTT)	Fluka® Analytical
2log DNA ladder	New England Biolabs
Epidermal growth factor (EGF)	Sigma-Aldrich®
EGF-Alexa647	Michael Sonntag, AG Brunsveld, TU Eindhoven, Netherlands
Ethanol	J.T.Baker
Ethylenediaminetetracetic acid (EDTA)	Fluka® Analytical
Fetal bovine serum (FBS) Sera Plus	PAN™ Biotech
Fluorescein isothiocyanate	EGA-Chemie
Glycine	Carl Roth GmbH
Hydrogenperoxid (H_2O_2)	Merck
Immobilon-FL PVDF	Millipore, Merck KGaA
Isopropanol	J.T.Baker
L-glutamine	PAN™ Biotech
Methanol	AppliChem GmbH
2-Mercapto-ethanol	SERVA Electrophoresis GmbH
Non-essential amino acids (NEAA)	PAN™ Biotech
Phosphatase inhibitor cocktail 2 + 3	Sigma-Aldrich®
Poly-Lysine	Sigma-Aldrich®
Precision plus protein ladder	Bio-Rad
RedSafe	Chembio Ltd

Sodium dodecyl sulfate (SDS)	SERVA Electrophoresis GmbH
sodium orthovanadate	Sigma-Aldrich®
N,N,N',N'-Tetramethylene-diamine (TEMED)	Sigma-Aldrich®
tet5-Atto590 (Atto590-NH_2-Ester (Sigma))	Amit Sachdeva (LMB Cambridge)
TetraSpecks	Life Technologies GmbH
Tris-base	Carl Roth GmbH
Tris-HCl	J.T.Baker
Triton X-100	SERVA Electrophoresis GmbH
Trypsin-EDTA	PAN^{TM} Biotech
Tween-20	SERVA Electrophoresis GmbH
UltraPure^{TM} Agarose	Invitrogen^{TM} Life Technologies

3.1.2. Buffers and media

Cell lysis buffer	9803, Cell Signaling Technology
DMEM	PAN^{TM} Biotech
DNA sample buffer	50% glycerol
	0.1% Orange F
	0.1 M EDTA
DPBS	PAN^{TM} Biotech
HBSS	PAN^{TM} Biotech
LB medium	10 g/l Bacto-Trypton
	5 g/l yeast extract
	10 g/l NaCl
	pH7.4
MOPS buffer	50 mM 3-(N-morpholino)propanesulfonic acid
	50 mM Tris-base
	0.1% SDS
	1 mM EDTA
	pH7.7
Odyssey® Blocking Buffer	LI-COR Biosciences
OptiMEM	Gibco® by LifeTechnologies
4% Paraformaldehyde (PFA)	4 g Paraformaldehyde in 100 ml PBS

SDS running buffer	25 mM Tris-base
	192 mM glycine
	0,1% SDS
5x SDS sample buffer	60 mM Tris-HCl (pH6.8)
	25% glycerol
	2% SDS
	14.4 mM 2-mercapto-ethanol
	0.1% bromo-phenolblue
SOC medium	20 g/l Bacto-Trypton
	5 g/l Bacto-yeast extract
	0.5 g/l NaCl
	2.5 mM KCl
	10 mM $MgCl_2$
	20 mM glucose
TAE buffer	40 mM Tris-acetate
	1 M EDTA
	20 mM NaOAc
TBS	100 mM Tris-HCl
	150 mM NaCl
TBS-T	100 mM Tris-HCl
	150 mM NaCl
	0.1% Tween 20
transfer buffer	25 mM Tris-base
	192 mM glycine
	20% methanol

3.1.3. Antibodies

Primary antibodies:

mouse anti-a-Tubulin	Sigma Aldrich
rabbit anti-EGFR	4267, Cell Signaling Technology
goat anti-EGFR	AF231, R&D Systems
mouse anti-GFP	632681, Clontech
rabbit anti-GFP	632593, Clontech

mouse pY845	558381, BD Biosciences
rabbit pY1045	2237, Cell Signaling Technology
rabbit pY1068	3777, Cell Signaling Technology
mouse pY1068	2236L; Cell Signaling Technology
rabbit pY1173	2244S, Cell Signaling Technology
mouse anti-phosphotyrosine (PY72)	P172.1, InVivo Biotech Services
rabbit anti-Rab11	3539, Cell Signaling Technology
mouse anti-Rab11	610656, BD Biosciences
anti-GAPDH	2118, Cell Signaling Technolgy

Secondary antibodies western blots:

IRDye 800 donkey anti-rabbit IgG	LI-COR Biosciences
IRDye 680 donkey anti-mouse IgG	LI-COR Biosciences
IRDye 800 donkey anti-goat IgG	LI-COR Biosciences
IRDye 680 donkey anti-rabbit IgG	LI-COR Biosciences

Secondary antibodies immunofluorescence:

Alexa Fluor® 647 chicken anti-rabbit IgG	Life Technologies
Alexa Fluor® 647 donkey anti-mouse IgG	Life Technologies
Alexa Fluor® 555 donkey anti-goat IgG	Life Technologies
Alexa Fluor® 488 donkey anti-mouse IgG	Life Technologies
Alexa Fluor® 546 goat anti-rabbit IgG	Life Technologies
Alexa Fluor® 546 goat anti-mouse IgG	Life Technologies

3.1.4. Enzymes

AccuPrime *Pfx* DNA polymerase	Invitrogen™ Life Technologies
Calf Intestinal Alkaline Phosphatase	Invitrogen™ Life Technologies
PfuUltra™ HF polymerase	Agilent
Restriction enzymes	New England Biolabs
T4-DNA ligase	Invitrogen™ Life Technologies
T4 DNA polymerase I	New England Biolabs

3.1.5. Kits

Roti®-Prep Plasmid MINI	Carl Roth GmbH
NucleoBond® Xtra Midi Plus EF	Macherey-Nagel
Micro BCA™ Protein Assay Kit	Thermo Scientific
Nucleoseq Columns	Macherey-Nagel
Zymoclean™ Gel DNA Recovery Kit	Zymo Research
FuGENE® HD Transfection Reagent	Promega
Lipofectamine® Transfection Reagent	Invitrogen

3.1.6. Plasmids

EGFR-mCitrine	Encoding ErbB1 with C-terminally fused mCitrine
EGFR-mCherry	Encoding ErbB1 with C-terminally fused mCherry
pcDNA3.1+	Invitrogen
tagBFP-Rab11a	Encoding human Rab11a with N-terminally fused tagBFP
Rab5-mCherry	Encoding human Rab5 with C-terminally fused mCherry
c-Cbl-mCherry	Encoding human c-Cbl with C-terminally fused mCherry
tagBFP-PTP1B	Encoding human PTP1B with N-terminally fused tagBFP
PTB-mCherry	Encoding human phospo tyrosine binding domain (PTB) with C-terminally fused mCherry
mCherry-PTP1B-D181A	Encoding PTP1B D181A mutant with N-terminally fused mCherry
EGFR-paGFP	Encoding human EGFR with C-terminally fused paGFP
YHT-Synthetase-NES (VB8.2)	Encoding tRNA synthetase tagged with a NES and 4 copies of tRNA (gift from Jason Chin)
eRF1 E55D	Encoding eukaryotic release factor 1 E55D mutant (gift from Jason Chin)

3.1.7. Instruments and equipment

'Vortex Genie I' touch mixer	Scientific Industries
1.5 mm 10- and 15-well combs	Invitrogen™ Life Technologies
1.5 mm cassettes for western blots	Invitrogen™ Life Technologies
35 mm MatTek petri dishes	MatTek Corporation
35 mm µ-Dish high Glass Bottom	ibidi

4-well LabTek chambers	Nunc by Thermo Fischer
8-well LabTek chambers	Nunc by Thermo Fischer
BioRad Power Pac HC	Bio-Rad Laboratories
Cell scraper 16cm 2-Pos.-blade	Sarstedt AG and Co.
Centrifuge 5415R	Eppendorf
Centrifuge 5810R	Eppendorf
Centrifuge RC 26 Plus	Sorvall®
Eppendorf safe lock tubes (0.5/1.5/2 ml)	Eppendorf
Falcon tubes (15/50 ml)	BD Falcon™
Heatable magnetic stirrer 'IKMAG®RCT'	IKA®Labortechnik
Incubation box for western blots	LI-COR Biosciences
MilliQ water	Millipore
Mini and Midi agarose gel chamber	Carl Roth GmbH
Molecular Imager Gel Doc XR	Bio-Rad Laboratories
Multiscan Ascent	Thermo Fischer
Nanodrop® ND-1000 spectrophotometer	Peqlab Biotechnologie GmbH
Nuaire™ Cellgard Class II Biolog. Safety Cabinet	Integra Biosciences
NuPage 4-12% Bis-Tris Gel	Novex by Life Technologies
Odyssey Infrared Imager	Licor® Biosciences
Parafilm®	Pechiney Plastic Packaging
PCR cycler	Eppendorf
Pherastar FS	BMG Labtech
T25 tissue culture flask	Sarstedt
Tissue culture plates (6-well)	BD Falcon™
Tissue culture plates (24-well)	Biofil
Typhoon Trio Variable Mode Imager	GE Healthcare
Vacuum centrifuge	Eppendorf
XCell II™ Blot Module	Invitrogen™ Life Technologies
XCell SureLock™ Mini-Cell Electrophoresis Sys.	Invitrogen™ Life Technologies

3.1.8. Software

Adobe Illustrator CS4	Adobe Systems
DNASTAR Navigator v2.2.1.1	DNASTAR

Fiji	http://fiji.sc/Fiji
GraphPad Prism	GraphPad Software Inc.
ImageJ	http://imagej.nih.gov/
Igor Pro	Wavemetrics
MacPymol	http://www.pymol.org/
Matlab R2010b/R2014	Mathworks

3.2. Molecular biology

3.2.1. Polymerase chain reaction (PCR)

The polymerase chain reaction (PCR) was used for the amplification of DNA fragments[120]. DNA polymerases complete single-stranded template from a starting point that is determined by a primer. For normal DNA amplification the accuprime *Taq* polymerase from *Thermus aquaticus* and for mutagenesis PCR reactions the *Pfu* polymerase from *Pyrococcus furiosus* was used. The following composition and program were used for a standard PCR:

25-50 ng DNA		*95°C*	*2 min*
1,5 µl primer fwd		*95°C*	*30 sec*
1,5 µl primer rev	*30x*	*50/55/62°C*	*30 sec*
5 µl Accuprime buffer		*68°C*	*1 min per 1 kb*
1 µl Accuprime polymerase		*68°C*	*10 min*
add 50 µl A. dest.		*8°C*	∞

Mutagenesis PCR was carried out using the following PCR mix and cyclic parameters:

50 ng DNA		*95°C*	*2 min*
1 µl dNTPs		*95°C*	*30 sec*
1,25 µl primer fwd	*16x*	*50/55/62°C*	*30 sec*
1,25 µl primer rev		*72°C*	*1 min per 1 kb*
3 µl DMSO		*72°C*	*10 min*
5 µl 10x Pfu Polymerase buffer		*8°C*	∞
1 µl Pfu Polymerase			
add 50 µl A. dest.			

3.2.2. Agarose gel electrophoresis

The agarose gel electrophoresis utilizes an electric field to separate DNA fragments according to their molecular size. DNA fragments migrate to the anode, because of the negative charge of the nucleic acids. The smaller the DNA fragment, the faster it migrates to the anode.

Agarose gels were prepared with 1xTAE buffer supplemented with the DNA binding reagent RedSafe (5 µl/100 ml). Addition of RedSafe allows the visualization of the DNA fragments using UV light. RedSafe has two excitation maxima, one at 309 nm and the other at 419 nm, and exhibits its emission maximum at 537 nm. Electrophoresis was performed for 30 min at 120 V in a gel chamber filled with 1xTAE buffer. To detect DNA fragments the agarose gel was transferred into a gel documentation chamber.

For sample preparation, DNA samples were mixed with 10x DNA sample buffer. The DNA marker 2log was used as a molecular weight standard.

3.2.3. Digest

Cleavage of double stranded DNA was performed using specific restriction endonucleases. These enzymes recognize specific DNA sequences and hydrolyse phosphodiesterbonds leading to double strand breaks. The following reaction mix was set up for 3 hr at 37°C:

5 µl	*buffer (10x)*
3-5 µg	*DNA*
1 µl	*restriction enzyme*
add. 50 µl	*A. dest.*

3.2.4. Vector dephosphorylation

Dephosphorylation of the 5'ends of vector DNA prevents vector religation. Therefore, 1 µl of Calf Intestinal Alkaline Phosphatase (CIAP) was added to the digestion sample and incubated for 15 min at 37°C. Inactivation of CIAP was achieved by incubation for 10 min at 75°C.

3.2.5. Calculation of DNA concentration

The DNA concentration of PCR products and vector DNA was photometrically determined using Nanodrop1000 by measuring the absorption at 260 nm. An $OD_{260\,nm}$ of 1.0 corresponds to 50 µg/ml of double-stranded DNA.

3.2.6. DNA Ligation

DNA ligation was performed using the T4-DNA ligase from Invitrogen™ Life Technologies. The ligase covalently connects the 3'-hydroxy- and 5'phosphate-ends of double-stranded DNA. Both 'blunt ends' and two complementary overhangs ('sticky ends') can be ligated. A ratio of 1:4 of vector DNA to insert DNA was used for the ligation reaction. The required amount of insert DNA was calculated using the following formular:

$$\text{Amount insert (ng)} = \frac{amount\ vector\ (ng)\ x\ insert\ size\ (bp)}{vector\ size\ (bp)}$$

The calculated amount of insert DNA was mixed with the vector DNA (25-50 ng), 4 µl T4-DNA ligase buffer and 1 µl T4-DNA ligase in a total volume of 20 µl. The ligation was performed for 1 hr at RT or overnight at 16°C. Inactivation of the ligase was achieved by incubation for 10 min at 65°C.

3.2.7. Ligation independent cloning (LIC)

LIC allows the insertion of DNA fragments at nearly any position in a vector. Therefore, vector DNA is made linear using restriction enzyme digestion and insert DNA is PCR amplified. The PCR amplified DNA fragments contain 10-20 complementary base pairs in both directions to the insertion site in the vector. The 3'→5' exonuclease activity of the T4-DNA polymerase I creates complementary overhangs between vector and insert DNA that can form a stable association. This allows transformation of the plasmid without any additional ligation step.

T4-DNA polymerase I treatment

To generate 5'-overhangs the linear vector DNA and the insert DNA were treated for 1 hr at 22°C with T4-DNA polymerase using the following reaction mix:

2 µl buffer 2
2 µl BSA
500 ng DNA
0.3 µl T4-DNA polymerase I
add. 20 µl A. dest.

To inactivate the T4-DNA polymerase I the sample was incubated for 20 min at 75°C.

Annealing

Ligation of vector and insert DNA was carried out in the presence of T4-DNA ligase buffer using the following composition:

2 µl T4-DNA ligase buffer
50 ng vector DNA
200 ng insert DNA
add. 10 µl A. dest.

After 30 min incubation at RT the DNA mix was used for transformation in chemical competent *E. coli* XL10 Gold cells.

3.2.8. Transformation of chemical competent E.coli cells

100 µl of chemical competent *E. coli* XL10 gold cells were mixed with 3.5 µl 2.25 M DTT and DNA. After 30 min incubation on ice DNA transformation was performed using a heatshock for 1 min at 42°C. Cells were kept on ice for 2 min, mixed with 400 µl SOC media and incubated for 1 hr at 37°C and 200 rpm. Cells were centrifuged for 1 min at 13000 rpm, the supernatant was discarded and the pellet was resuspended in 100 µl SOC media. Subsequently, cells were plated out on LB agar plates supplemented with the appropriate antibiotica and incubated overnight at 37°C. On the next day, 5 ml LB media (mini plasmid preparation) or 200 ml (midi plasmid preparation) with the appropriate antibiotica were inoculated with single colonies of *E. coli* cells picked from LB agar plates and bacterial cultures were grown overnight at 37°C and 200 rpm before DNA preparation.

3.2.9. DNA sequencing

All plasmids generated in this thesis were completely sequenced using the GATC sequencing service or the 'In house MPI' sequencing service. For 'in house' sequencing, the following PCR mix and PCR program were used to amplify DNA fragments:

3 µl	*Big dye buffer*		*96°C 1 min*
2 µl	*Big dye*		*96°C 10 sec*
0.5 µl	*primer*	*25x*	*50°C 5 sec*
250 ng	*DNA*		*60°C 4 min*
add. 20 µl	*A. dest.*		*8°C* ∞

DNA fragments were cleaned from PCR reagencies using Nucleoseq columns and dried using a vacuum centrifuge for 45 min at 45°C.

3.3. Cell culture

3.3.1. Cell lines

The following mammalian cell lines were used in this thesis:

COS7: fibroblast like cell line, kidney tissue from African Green Monkey

HEK293T: human embryonic kidney cells

3.3.2. Culture of mammalian cells

Mammalian cells were cultured in DMEM supplemented with 10% FBS, 1% L-Glutamine and 1% NEAA in T25 or T75 tissue culture flasks and incubated at 37°C and 5% CO_2. When cells were 90-100% confluent, they were detached and seeded in new tissue culture flasks. To split mammalian cells the media was discarded, cells were washed once with PBS and Trypsin-EDTA was added to detach cells. After 5-10 min incubation at 37°C media was added to the cells and cell density was measured using the cell counter. Subsequently, cells were seeded in new tissue culture flasks or plated in Labteks, Matteks or tissue culture plates for further experiments. Eventually, Labteks or Matteks were coated with poly-L-lysine (0,01%) prior to seeding the cells.

3.3.3. Transfection

Transfection of mammalian cells with plasmid DNA was achieved using Fugene®6 according to the manufacturers protocol. Mixing of these cationic lipid reagents with plasmid DNA produces liposomes that fuse to the cell membrane and thereby deliver their content to the cytoplasm. 3 µl Fugene were incubated in 100 µl serum-free media for 5 min before addition of 1 µg DNA to generate a 3:1 ratio of Fugene to DNA. After 10 min incubation the transfection mix was added dropwise to one well in a 6-well dish. 4-well

Labteks were transfected with 25 µl and 8-well Labteks with 12.5 µl and the appropriate amount of DNA and Fugene.

3.3.4. siRNA transfection

Transfection of Rab11a siRNA from Santa Cruz was done using siRNA transfection reagent in transfection medium. Rab11a siRNA (sc- 36340-SH; Santa Cruz Biotechnology) or scrambled non-targeting control siRNA (sc-37007; Santa Cruz Biotechnology) were used at a final concentration of 50 nM for 72 hr. 1,25 µl Rab11a or scrambled non-targeting siRNA were mixed with 25 µl transfection media. In parallel, 1,5 µl transfection reagent was incubated in 25 µl transfection media for 5 min. Both solutions were mixed and incubated for 30 min at RT. Cells were washed once with 200 µl transfection media before addition of the transfection mix. Media was changed to normal growth media with 20% FBS 6 hr after transfection and then changed again every 24 hr to normal growth media. Cells were eventually transfected with additional plasmid DNA after 48 hr siRNA transfection.

Transfection of Rab11a/b siRNA from Qiagen was achieved using Lipofectamine 3000 Transfection Reagent. Rab11a and Rab11b isoforms were simultaneously knocked down using double-stranded small interfering RNAs (siRNAs) targeted against the following target sequences 5´(AATGTCAGACAGACGCGAAAA)-3´ for Rab11a and 5´(AAGCACCTGACCTATGAGAAC)-3´ for Rab11b at a final concentration of 40 nM for 72 hr. Scrambled non-targeting control siRNA (1027281, Qiagen) was used at a final concentration of 40 nM. Rab11a/b or scrambled non-targeting siRNA were incubated for 5 min in serum-free media in a total volume of 50 µl. In parallel, 1,25 µl Lipofectamine 3000 and 1 µl P3000 were incubated with 47,75 µl serum-free media. Both solutions were mixed, incubated for 25 min at RT and added to the cells. Media was changed after 6 hr and then every 24 hr. Transformation of plasmid DNA was eventually performed after 48 hr siRNA transfection.

3.3.5. Site specific labeling of EGFR

4-6 hr after transfection media was removed and replaced with media containing 1 mM BCNK. After overnight incubation at 37°C with 5% CO_2 cells were washed with media every 15 min for at least 1 hr. Labeling was performed using 400 nM of the tetrazine (tet)-

fluorophore conjugate in DMEM for 20 min at RT. The washout of unbound tet-fluorophore conjugate was carried with media out for at least 2 hr every 15-20 min.

3.4. Protein biochemistry

3.4.1. Cell lysis

For cell lysis, cells were seeded in 6-well or 24-well cell culture dishes and incubated overnight at 37°C with 5% CO_2. On the next day cells were transfected and 6-8 hr after transfection starved overnight in DMEM with 1% L-glutamine, 1% NEAA and 0.5% FBS. Untreated, EGF-stimulated or PV-treated cells were washed once with ice-cold DPBS before adding ready-made Cell Lysis Buffer or RIPA buffer supplemented with Complete Mini EDTA-free protease inhibitor and phosphatase inhibitor cocktail 2 and 3. After 10 min incubation on ice, cells were scrapped with a cell-scraper and transferred in a pre-cooled 1.5 ml Eppendorf tube. Cells were centrifuged for 10 min at 13000 rpm and 4°C and supernatants were transferred into a new pre-cooled 1.5 ml Eppendorf tube. Protein concentrations were determined using BCA protein assay. Lysates were either subsequently boiled at 95°C for 5 min with 5x SDS sample buffer and used for SDS-page analysis or stored at -20°C until further use. In case of in-gel fluorescence analysis samples were only mixed with 4xLDS Nupage sample buffer, but not boiled to do not destroy the fluorophore.

3.4.2. Calculation of protein concentration

Protein concentrations were measured using the Micro BCA™ Protein Assay Kit from Thermo Scientific according the manufacturers protocol. The assay allows accurate determination of protein concentrations between 0.5 to 20 μg/ml by measuring the absorption at 562 nm in a 96-well plate. 4 μl of the protein sample were mixed with 80 μl BCA reaction mix and incubated for at least 30 min at 37°C. Protein concentrations were measured and calculated using the Multiscan Ascent.

3.4.3. SDS gel page

Denaturing sodiumdodecylsulfate-polyacrylamide gel electrophoresis (SDS-PAGE) was performed to separate proteins according to their molecular weight in whole cell lysate

samples. Proteins were denatured and homogenously negatively charged by the SDS[121]. This allowed separating the proteins by their relative molecular mass during migration through the electric field. The smaller the proteins, the faster they migrate to the anode. For SDS-PAGE SDS gels of 1.5 mm thickness and with 10 lanes were prepared directly before usage following the below described protocol:

Separating gel (8%)		Stacking gel	
4.6 ml	A. dest	3.4 ml	A. dest
2.7 ml	30% acrylamide	0.83 ml	30% acrylamide
2.5 ml	1.5 M Tris (pH 8.8)	0.63 ml	1 M Tris (pH6.8)
0.1 ml	10% SDS	0.05 ml	10% SDS
0.1 ml	APS	0.05 ml	10% APS
0.006 ml	TEMED	0.005 ml	TEMED

Protein samples were mixed with 5xSDS sample buffer, boiled for 5 min to denature proteins and centrifuged for 1 min at 13000 rpm. Protein gels were loaded with protein samples and ran for 2 hr at 120 V (Invitrogen) in SDS running buffer. Precision plus protein ladder was used as a protein standard. To visualize protein bends SDS gels were used for western blot analysis.

Alternatively, precasted 4-12% Bis-Tris gels from NuPage or self-cast 10% Bis-Tris gels were used for SDS gel analysis. Protein samples were mixed with 4xLDS sample buffer and centrifuged for 1 min at 13000 rpm. Protein gels were loaded with protein samples and ran for 1 hr at 180 V in MOPS buffer. Precision plus protein ladder was used as a protein standard. To visualize fluorescence and protein bends Bis-Tris gels were used for In-gel fluorescence analysis and western blot analysis.

3.4.4. In-gel fluorescence

Bis-Tris gels were imaged with the Typhoon reader to detect fluorescently labeled proteins. Atto590 was excited using a 532 nm laser line and fluorescence emission was detected with a 610/30 BP filter (Atto590). The resolution was set to 100 microns.

3.4.5. Western blot

Proteins were transferred on a PVDF membrane using the 'wet transfer' Invitrogen system. To transfer proteins on a PVDF membrane the blot sandwich was assembled as follows from bottom-up: Cathode, 2xsponge, Whatman paper, gel, PVDF membrane, Whatman paper, 3xsponge, anode. The blot sandwich was plugged in the XCell SureLock^{TM} Mini-Cell Electrophoresis System filled with transfer buffer. The transfer was done applying 40 V for 60-70 min. Subsequently, the PVDF membrane was incubated for 1 hr in Licor blocking buffer or in TBST supplemented with 5% milk powder to block the remaining binding sites on the membrane. Primary antibodies that specifically detect immobilized proteins were added on the PVDF membrane in Licor buffer or TBST with 5% milk and incubated overnight. On the next day PVDF membranes were washed 3x with TBST, 1 hr incubated with secondary antibodies in Licor blocking buffer or in TBST supplemented with 5% milk powder and washed again 3x with TBST. Detection was performed using the Licor Odyssey Dual Colour Scanner or the Biorad ChemiDoc^{TM} XRS+.

3.5. Immunohistochemistry

3.5.1. Immunofluorescence

Cells were fixed with 4% PFA in PBS (pH7.4) for 10 min at RT and then rinsed thrice with TBS. Subsequently, cells were permeabilized with 0.1% Triton-X in TBS for 5 min at RT and rinsed three times with TBS. Blocking was performed for 1 hr at RT or overnight at 4°C in Odyssey® Blocking Buffer to reduce background staining. Primary antibodies were applied for 1-2 hr at RT or overnight at 4°C. After washing three times with TBS, secondary antibodies were applied for 1 hr at RT. Cells were washed again thrice with TBS and imaged in TBS at 37°C.

3.6. Fluorescence microscopy

3.6.1. Confocal laser-scanning microscopy (LSM)

Confocal images of fixed or living cells were obtained with the LeicaSP5, Olympus FV1000 or LeicaSP8 confocal laser-scanning microscopes.

<u>LeicaSP5</u>

The LeicaSP5 was equipped with a HCX PL APO 63x/1.4 NA oil objective and an incubation chamber at 37°C. Fluorophores or fluorescent proteins were excited, using a

405 nm Cube laser, 488 nm and 514 nm Argon line, a 561 nm DPSS laser and a 633 nm Helium-Neon laser line. Fluorescence emission was sequentially selected with an Acousto-optical Beam Splitter (AOBS) for the following fluorophores/fluorescent proteins – mTagBFP (415-458 nm), mCitrine (525-551 nm), mCherry (571-623 nm) and Alexa647 (643-680 nm). All images were 3x line averaged and acquired with a frequency of 400 Hz. The pinhole was half-opened (2,5 airy units). Live cells were imaged in imaging media and stimulated with either 100 ng/ml EGF or 5 ng/ml EGF-Alexa647.

Olympus FV1000

Confocal images at the Olympus FV1000 equipped with a 60x/1.35 NA oil objective and a temperature controlled incubation chamber were acquired in sequential mode frame by frame. mTagBFP was excited with a 405 nm Diode-UV laser, mCitrine/Alexa488 with a 488 nm Argon laser, mCherry/Alexa555/Atto590/Cy3.5 with a 561 nm DPPS laser and Alexa647 with a 633 nm Helium-Neon laser using the DM405/488/561/633 dichroic mirror. Blue fluorescence (mTagBFP) was collected using a bandwidth of 425-478 nm and through a SDM490 emission beam splitter. Yellow fluorescence was detected between 498-551 nm using the SDM560 beam splitter. Red fluorescence was detected in the bandwidth of 575-623/675 nm depending on the presence of a far-red fluorophore and separated from the far-red emission using a SDM640 beam splitter. All images were 2x line averaged and acquired with a half-open pinhole (2,5 airy units). Live cells were imaged in imaging media and stimulated with EGF or PV, whereas fixed cells were imaged in PBS/TBS.

LeicaSP8

The LeicaSP8 was equipped with a HC PL APO CS2 60x/1.4 NA oil objective and an environmental-controlled chamber at 37°C. mCitrine and mCherry/Atto590 were excited at 488 nm or 561 nm using a 470-670 nm white light laser. Detection of fluorescence emission was restricted with an Acousto-optical Beam Splitter to the following bandwidth – mCitrine (498-551 nm) and mCherry (575-675 nm). Images were obtained in sequential mode and the pinhole was set to 250 μm. Live cells were imaged in imaging media and stimulated with 100 ng/ml EGF or 0.33 mM PV.

3.6.2. Fluorescence lifetime imaging microscopy (FLIM)

Time-domain FLIM, the technique used in this work, enables to monitor protein dynamics and protein-protein interactions at a high spatial-temporal resolution. In time-domain FLIM the sample is excited with a very short pulse of light that is much shorter than the decay time τ of the sample. Following the excitation pulse the decay time is calculated using the slope of a plot of log I(t) versus the time t, or from the time the intensity decreases to 1/e of the intensity at t=0. To avoid effects of rotational diffusion and anisotropy on the decay time, the intensity decays are measured through a polarizer oriented in an angle of 54.7° from the vertical axis (**Fig.15**).

The above described excitation with a very short pulse of light results in the excitation of an initial population (n_0) of molecules in the excited state. The decay rate of excited fluorophores n(t) depends on the emissive rate Γ and the nonradiative rate k_{nr} according to:

$$\frac{dn(t)}{dt} = (\Gamma + k_{nr})n(t)$$

Because emission is a random event and each fluorophore possesses equal probabilities to emit a photon in a certain time the exponential decay of the excited state population can be given by:

$$n(t) = n_0 exp(-t/\tau)$$

where n_0 is the number of molecules at t=0 and τ is the inverse of the total decay rate, $\tau = (\Gamma + k_{nr})^{-1}$. The inverse of the total decay rate can be considered as the sum of all rates that depopulate the excited state. As the fluorescence intensity is proportional to n(t), the decay rate of the excited fluorophore population can also be described using the fluorescence intensity. Substitution of the number of molecules by the intensity results in the usual expression for a single exponential decay:

$$I(t) = I_0 \exp(-t/\tau)$$

where I_0 is the intensity at t=0 and τ is the inverse of the total decay rate , $\tau = (\Gamma + k_{nr})^{-1}$.

Time-domain FLIM is mostly performed using time-correlated single-photon counting (TCSPC). In TCSPC, less than one photon is detected per laser pulse by either high-speed microchannel plates (MCPs), photomultiplier tubes (PMTs) or avalanche photodiodes

(APDs). The time between excitation pulse and photon detection is named as the decay time and stored in a histogram, where the x-axis shows the time difference between excitation and detection and the y-axis represents the number of photon counts per time difference. To complete the histogram this process is repeated multiple times using a pulsed laser. However, nowadays all TCSPS measurements are performed in the 'reverse mode'. Thereby the measurement starts upon photon detection and ends with the next excitation pulse. This mode is preferred, because it speeds up the measurement.

In FRET measurements we collect a mixture of different decay profiles requiring a multiexponential decay model to fit the data. A multiexponential decay is the sum of several single exponential decays:

$$I(t) = \sum_{i=1}^{n} a_i \exp\left(-\frac{t}{\tau}\right) + B$$

with the background B, the number of decay times n, the amplitudes of the components α_i and the fluorescence decay times τ_i. If we have two different lifetimes from donor only molecules and donor molecules interacting with acceptor molecules in a certain conformation the fraction (α) of interacting molecules within each pixel can be calculated according to:

$$\alpha(x,y) = \frac{A_F(x,y)}{A_D(x,y) + A_F(x,y)}$$

where A_D is the amplitude of the donor only molecules and A_F the amplitude of the acceptor-bound donor molecules.

FLIM data were obtained on the Olympus FV1000 laser scanning microscope equipped with an external unit, PicoQuant's compact FLIM and FCS upgrade kit for laser scanning microscopes. Pulsed lasers are coupled to the FV1000 through an independent port and controlled by a driver that can be digitally modulated (PicoHarp 300). Detection of photons was achieved using a single photon avalanche diode, and transferred to the PicoHarp 300 data acquisition unit. Pulsed lasers where controlled via the Sepia II software and detected with an APD. Image integration time was approximately 2-3 min per image to reach a total photon count of 3-5 x 10^6 photons per image. mCitrine was excited by a 507 nm pulsed laser (at 67%) through a DM 440/510 dichroic mirror. The fluorescence of mCitrine was detected by APDs with a 537/26 bandpass filter. Following

data acquisition, the fluorescence lifetimes τ and fractions (α) of interacting molecules are calculated by fitting the decay histograms to any model that accounts for or excludes the instrument response function (IRF). In this work, all FLIM data were analyzed using the global analysis code described in [122].

To quantify the mean spatial coincidence between areas with high EGFR-PTP1B D181A interactions and areas in the vicinity of the Rab11-positive pericentriolar REs those areas were first identified by tri-level or bi-level thresholding using Otsu's method for multi-level thresholding and subsequently the overlap between both areas was calculated and represented as a percentage from the total area of high EGFR-PTP1B D181A interactions. A more detailed description of this analysis can be found in [123].

3.6.3. Widefield anisotropy

Anisotropy measurements use polarized light for the photoselective excitation of fluorophores. Photon absorption by fluorophores is favored, when the electric vector of a photon is aligned parallel to the transition moment of the fluorophore. Thus excitation of randomly orientated fluorophores in an isotropic solution with polarized light selectively excites fluorophores whose absorption transition dipole is parallel to the electric vector of the excitation light. The fluorescence anisotropy (r) is given by:

$$r = \frac{I_{\parallel} - I_{\perp}}{I_{\parallel} + 2I_{\perp}}$$

where ($I_{\parallel}$) and ($I_{\perp}$) are the fluorescence intensities of the parallel ($I_{\parallel}$) and perpendicular ($I_{\perp}$) polarized emission. Rotational diffusion displaces the emission dipole of the fluorophore and decreases the fluorescence anisotropy. Usually, molecules rotate within 50 to 100 ps; a time that is far below fluorescence lifetimes, which range from 1 to 10 ns. An additional process that lowers fluorescence anisotropy is the depolarization of the emission light caused by the Förster resonance energy transfer (FRET). FRET between identical fluorophores is named homoFRET and can be measured with anisotropy. Thus, anisotropy measurements allow the detection of homo-dimerization and oligomerization of proteins tagged with a fluorophore.

Anisotropy microscopy was performed on an Olympus IX81 inverted microscope equipped with a 20x/0.7 NA air objective using an Orca CCD camera and an incubation chamber at 37°C and 5% CO_2. The fluorescent proteins mCitrine and mCherry and the fluorophore Atto590 were excited using a MT20 illumination system. A linear dichroic polarizer was implemented in the illumination path of the microscope, and two identical

polarizers were placed in an external filter wheel at orientations parallel and perpendicular to the polarization of the excitation light. For each field of view two images were taken, one with the emission polarizer oriented parallel to the excitation polarizer ($I_{\parallel}$) and one with the emission polarizer oriented perpendicular to the excitation polarizer ($I_{\perp}$). To calculate the anisotropy (r^i) in each pixel *i* the following equation was used:

$$r^i = \frac{G_i I_{\parallel} - I_{\perp}}{G_i I_{\parallel} + 2 I_{\perp}}$$

To determine the G-factor (G_i) parallel and perpendicular images of the fluorophore fluorescein were taken in solution. Fluorescein's anisotropy is close to zero and therefore allows calculating G_i by building the ratio of the perpendicular over the parallel intensities. Live cells were imaged in vitamin-free media at 37°C and 5% CO_2 and stimulated with either 100 ng/ml EGF or 0.33 mM pervanadate.

3.6.4. Total internal reflection fluorescence (TIRF) microscopy

TIRF microscopy was done on an Olympus IX81 microscope equipped with a 60x/1.8 NA TIRFM APOCHROMAT oil objective and a incubation chamber at 37°C. paGFP and mCherry were excited with 488 nm and 561 nm laser lines through a Triple-pass 69000-ET-DAPI/FITC/TRITC filter set. Laser light passed through a condenser to allow manipulation of the incident angle of the light on the sample. EGFR-paGFP at the basal membrane of COS-7 cells was photoactivated using the 405 nm laser line for 500 ms and fluorescence emission of EGFR-paGFP and Rab5-mCherry was acquired over time under TIRF conditions as well as by wide-field illumination with a focus adjusted 2 μm above the glass-surface. Live cells were imaged in imaging media and stimulated with 100 ng/ml EGF or 0.33 mM pervanadate.

4. Results

4.1. A conformational sensor based on genetic code expansion reveals autocatalytic EGFR activation

To study the autocatalytic activation mechanism of EGFR we developed multiple FRET-based conformational EGFR indicator (CONEGI) variants with the donor, mCitrine, always genetically encoded in the same, fixed region of the TKD and the acceptor, Atto590, attached to different flexible TKD regions that undergo conformational changes upon activation, using genetic code expansion and bioorthogonal labeling chemistry (**Fig.13**). This design enables reporting of the conformational state of different key structural elements in the EGFR TKD, which then can be related to EGFR activity and self-association. The FRET efficiency will differ due to changes in the distance and/or orientation between mCitrine and Atto590 thereby reflecting conformational dynamics of the receptor. mCitrine was selected as donor because of its mono-exponential fluorescence profile [124,125] and the membrane-permeable fluorophore Atto590 as acceptor because of its high extinction coefficient (ε: 120.000), high quantum yield (QY: 0.8) and spectral overlap with mCitrine. Using CONEGI, we aimed to address whether the autocatalytic activation mechanism is based on the stabilization of EGFR monomers in an active conformation or the promotion of dimerization, and if Y845 phosphorylation is involved in EGFR autocatalysis.

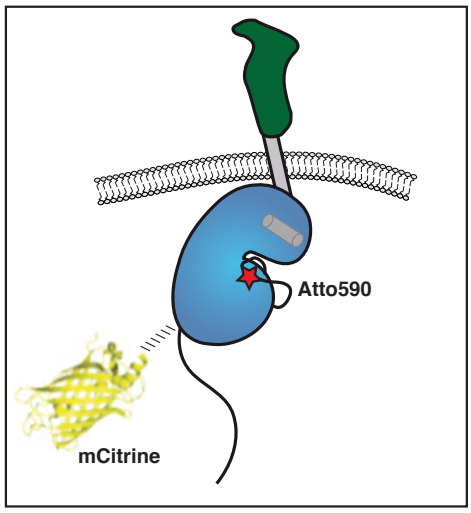

Figure 13: Design of CONEGI. Schematic representation of CONEGI. EGFR consists of an extracellular ligand binding domain (green), a single-pass transmembrane domain (grey) and an intracellular kinase domain (blue) followed by a C-terminal tail (black). CONEGI harbors mCitrine fused to the C-terminal end of the TKD using a coiled-coil linker (dashed line) and Atto590 site-specifically attached to the kinase domain (exemplary in the activation loop).

4.1.1. Exploiting structural data for the development of CONEGI

To design the conformational EGFR biosensor CONEGI, the crystal structure of the inactive EGFR TKD (PDB: 2GS7) was used to identify regions for mCitrine insertion (**Fig.14A**). Criteria for the mCitrine insertion included surface exposure, no interference with the dimerization interface and avoidance of TKD sites that are crucial for kinase activity such as the activation loop, the P loop and α helices. Hence, the loop between β-sheet 2 and 3 (kinase loop 2), a loop in proximity to the αC-helix and a region at the end of the EGFR TKD were selected as potential insertion sites for mCitrine. Two linkers, both with a helical (LAAAYSSILSS) and a short flexible region (NLSSDS) forming a coiled coil helix were used for mCitrine insertion into EGFR (LAAAYSSILSSNLSSDS-mCitrine-SDSSLNSSLISSYAAAL) to constrain the orientation of mCitrine and minimize perturbation of protein folding. This type of linker was previously established for fluorescent protein (FP) insertion into Eph receptors in our lab[105]. After an initial larger screen (data not shown), EGFR variants with mCitrine insertion between amino acids E712 and K713 (EGFR-EK-mCitrine), A726 and T727 (EGFR-AT-mCitrine) and Q958 and G959 (EGFR-QG-mCitrine) were used for further characterization. EGFR-EK-mCitrine and EGFR-AT-mCitrine showed endoplasmatic reticulum localization resulting in low phosphorylation levels after EGF stimulation on the Grb2-binding site Y1068[126] as determined by confocal fluorescence microscopy and Western blot analysis. EGFR-QG-mCitrine exhibited PM localization and a similar phosphorylation profile on Y1068 in response to EGF as compared to C-terminally tagged EGFR (EGFR-mCitrine) (**Fig.14B-D**), which was shown to follow the localization and activity of endogenous EGFR[44]. We thus selected EGFR-QG-mCitrine for the development of the conformational EGFR biosensor.

Because the QG site does not undergo conformational changes upon EGFR activation thereby serving as a rigid anchor point, Atto590 needs to be incorporated at a site that alters its conformation between active and inactive state. Therefore, we used genetic code expansion in combination with bioorthogonal labeling chemistry to site-specifically incorporate the UAA BCNK into EGFR and label it with a tetrazine (tet)-Atto590 conjugate. This technique allows attaching a small fluorophore in the EGFR TKD even in critical regions including the αC-helix and activation loop with only minimal perturbation of protein structure.

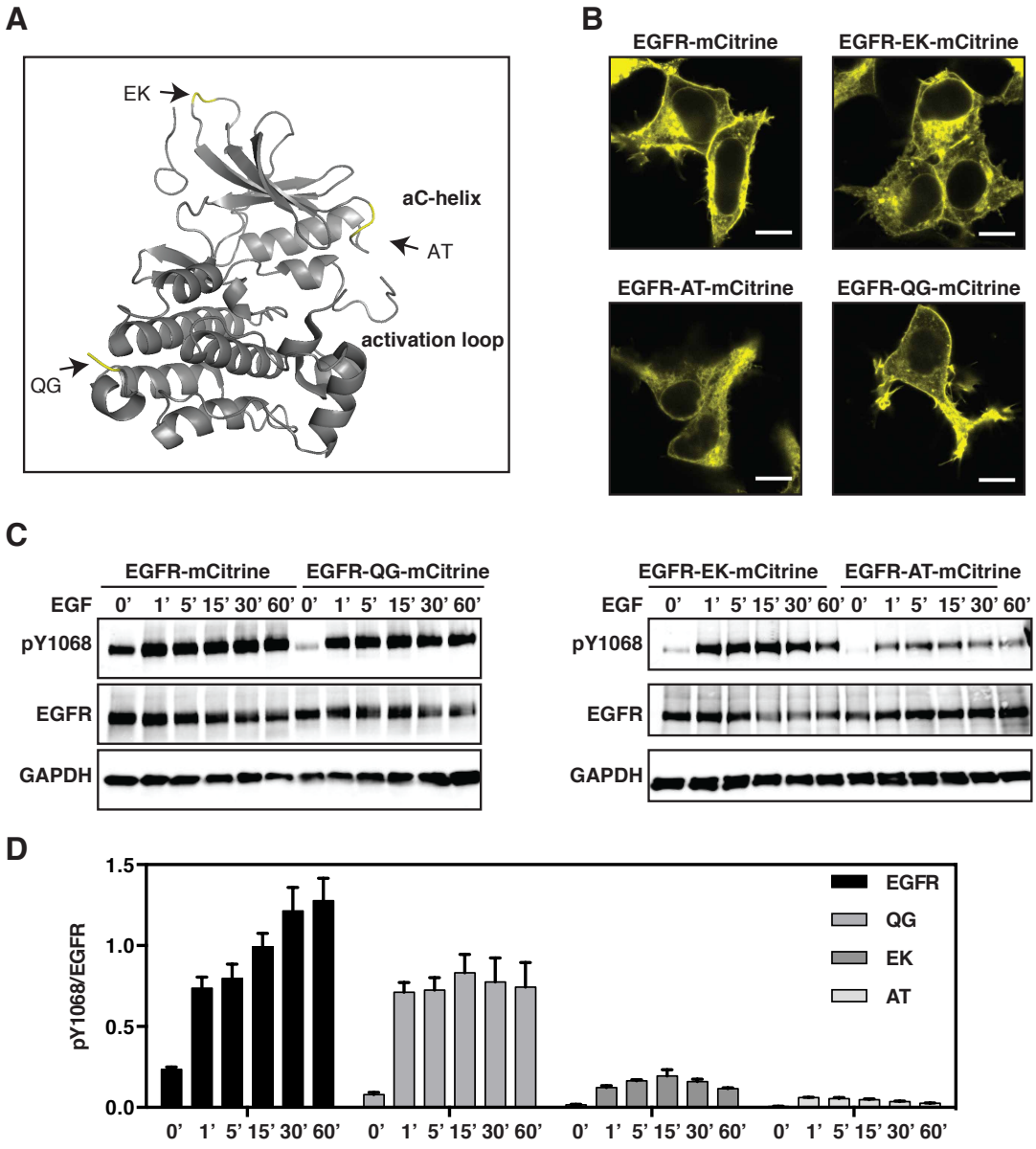

Figure 14: mCitrine insertion in different regions of the EGFR TKD. A. Crystal structure of the inactive (cyan; PDB: 2GS7) EGFR TKD. mCitrine has been inserted between amino acids (aa) E712 and K713 in kinase loop 2, aa A726 and T727 close to the αC-helix or aa Q958 and G959 at the end of the TKD. **B.** Representative fluorescence images of EGFR-mCitrine, EGFR-EK-mCitrine, EGFR-AT-mCitrine and EGFR-QG-mCitrine. n=10 cells/variant. Scale bars: 10 µm. **C.** Western blot analysis of EGFR-mCitrine, EGFR-EK-mCitrine, EGFR-AT-mCitrine and EGFR-QG-mCitrine upon EGF stimulation. Blots were probed for anti-EGFR, anti-pY1068 and anti-GAPDH. **D.** Relative Y1068 phosphorylation (pY1068/EGFR) of EGFR-mCitrine, EGFR-QG-mCitrine, EGFR-EK-mCitrine and EGFR-AT-mCitrine upon EGF stimulation. n=3. Error bars: SEM. EGF stimulation: 100 ng/ml.

To label EGFR-QG-mCitrine with Atto590 in the construction of the conformational EGFR sensor we used the well-established BCNK, which contains a strained alkyne functional group and is capable of undergoing an inverse electron-demand Diels-Alder cycloaddition with a tet-fluorophore conjugate[119]. Such a cycloaddition reaction is efficient and biocompatible, and allowed derivatization of EGFR with tet-Atto590 in living cells.

The incorporation of BCNK and attachment of a small sized organic fluorophore Atto590 is supposed to only minimally perturb the functionality of the TKD thereby allowing the incorporation of BCNK in any surface-exposed position of EGFR.

By aligning representative inactive (cyan; PDB: 2GS7) and active (red; PDB: 2J5F) crystal structures of the EGFR TKD we identified three regions in the EGFR kinase domain that undergo substantial conformational changes between the inactive and active conformation (**Fig.15**). Hence, the amber codon either replaced K713 in the kinase loop 2, K730 and D737 in the αC-helix or K843 and K851 in the activation loop or was positioned between amino acids E712 and K713.

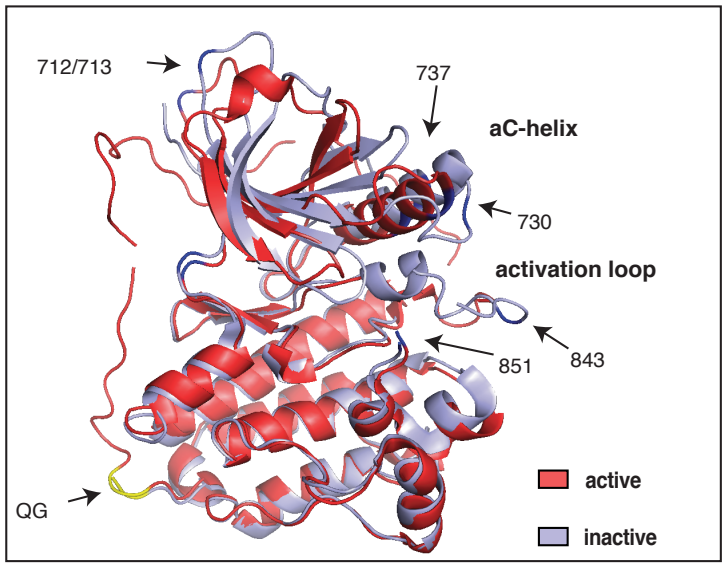

Figure 15: Alignment of active (red; PDB: 2J5F) and inactive (cyan; PDB: 2GS7) crystal structure of the EGFR TKD. mCitrine was inserted in the rigid QG site (yellow) at the C-terminal end of the TKD and BCNK at different sites (E712K713, K713, K730, D737, K843, K851) (blue) in TKD regions that undergo substantial conformational changes upon activation.

To determine whether the distances between mCitrine and Atto590 are sufficiently close to the Förster radius (R_0 ~5.89 nm) of the employed FRET pair to obtain FRET we measured the distances (R) between the QG site and each BCNK insertion site in the active and inactive conformation using the program PyMOL and calculated the FRET efficiencies (E_{FRET}) by $E_{FRET} = \frac{{R_0}^6}{{R_0}^6+R^6}$. The obtained distances of ~7.4-8.5 nm including the maximum length of the coiled coil linker (3.44 nm) resulted in FRET efficiencies of ~10-21% for the different CONEGI variants when assuming the orientation factor κ^2 to be 2/3 (**Table 1**), while keeping in mind that the crystal structures of the active and inactive EGFR TKD are only snapshots of non-full-length EGFR fragments taken in a non-physiological environment. We attached Atto590 at the desired site in the EGFR TKD in a two-step

process to create CONEGI's. In the first step, we expressed each EGFR(TAG)-QG-mCitrine gene using a derivative of the pyrrolylsyl-tRNA synthetase/$tRNA_{CUA}$ pair from *Methanosarcina mazei* to direct the incorporation of BCNK at the desired positions[119,127]. In a second step, we labeled each EGFR(BCNK)-QG-mCitrine variant with tet-Atto590 via an inverse electron-demand Diels Alder reaction, thereby creating the corresponding CONEGI variants.

Table 1: Distances and FRET efficiencies of the CONEGI variants. Linker length (~34.4 Å) is included in distances and for calculation of the FRET efficiencies the orientation factor κ^2 and the refractive index were assumed to be 2/3 and 1.4.

	Distance inactive (Å)	FRET $efficiency_{inact}$
712/713	45.7	0.14
713	45.7	0.14
730	50.8	0.1
737	45.3	0.14
843	47.5	0.12
851	39.3	0.21

4.1.2. BCNK-dependent expression and specific labeling of CONEGI's in living cells

To investigate the expression level of the different EGFR(BCNKXXX)-QG-mCitrine variants (where XXX indicates the position of BCNK incorporation) HEK293T cells were co-transfected with a derivative of the pyrrolylsyl tRNA synthetase/$tRNA_{CUA}$ pair from *Methanosarcina mazei*, a modified eukaryotic release factor 1 (eRF1 E55D mutant) to increase the expression efficiency and either one of the EGFR(BCNKXXX)-QG-mCitrine variants or the control EGFR-QG-mCitrine in the presence or absence of BCNK. Labeling with tet-Atto590 created the different CONEGI-XXX variants where XXX indicates the position of BCNK incorporation. EGFR-QG-mCitrine expression was independent of BCNK, whereas expression of the CONEGI variants was dependent on the presence of BCNK as detected by Western blot analysis. EGFR(BCNK851)-QG-mCitrine exhibited a comparable expression level to that of EGFR-QG-mCitrine, whereas all other EGFR(BCNKXXX)-QG-mCitrine variants showed a lower expression (**Fig.16A**, quantification in the upper right chart). Specific labeling of the EGFR(BCNKXXX)-QG-mCitrine variants was observed by fluorescence imaging of cell lysates following SDS

PAGE, while EGFR-QG-mCitrine was not labeled (**Fig.16A**, quantification in the lower right chart). We also obtained specific Atto590-labeling at the PM and at intracellular compartments of the CONEGI variants as judged by co-localization between mCitrine and Atto590 fluorescence by confocal microscopy, while EGFR-QG-mCitrine was not specifically labeled (**Fig.16B**).

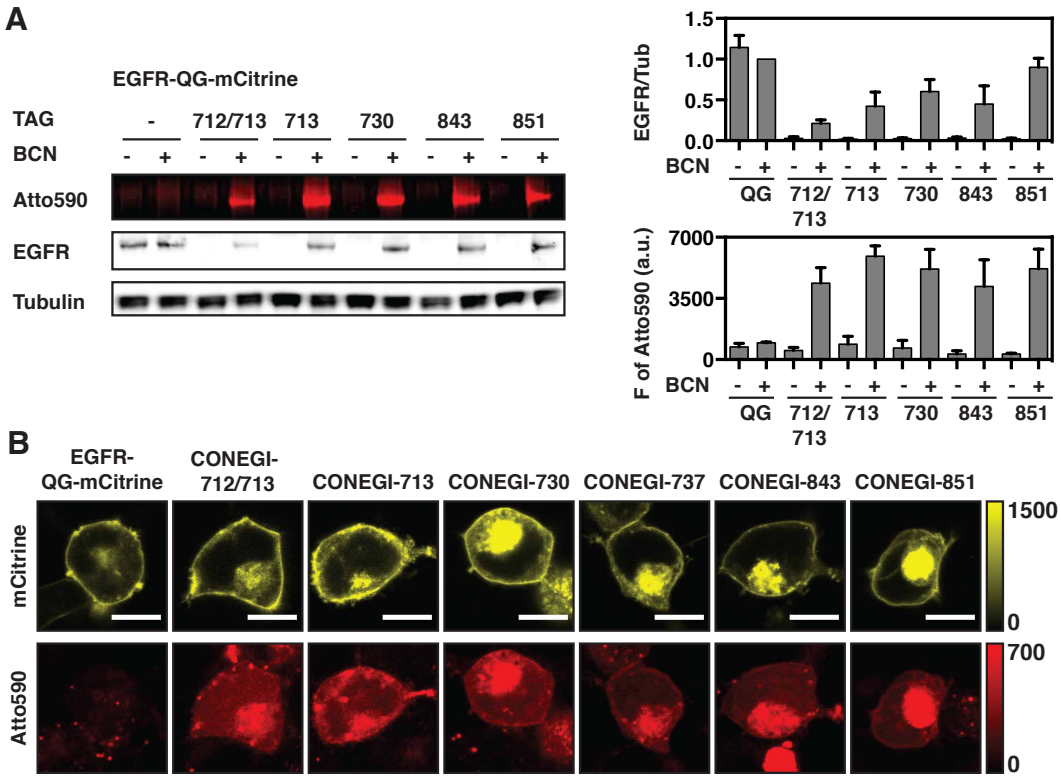

Figure 16: BCNK-dependent expression of CONEGI variants and specific labeling with tetrazine-Atto590. A. HEK293T cells ectopically expressing EGFR-QG-mCitrine or EGFR(BCNKXXX)-QG-mCitrine variants were grown in the absence or presence of 1 mM BCNK. Cells were labeled for 20 min with tetrazine-Atto590. Left panel: Atto590 fluorescence of resulting lysates visualized by fluorescence gel analysis and blots were probed for anti-EGFR and anti-tubulin. Upper right panel: Relative EGFR expression level (EGFR/Tub) of EGFR-QG-mCitrine and CONEGI's. Lower right panel: Intensity of Atto590 fluorescence (F of Atto590) of EGFR-QG-mCitrine and CONEGI's after 20 min tetrazine-Atto590 labeling. n=3. Error bars: SEM. **B.** Representative mCitrine and Atto590 fluorescence images of EGFR-QG-mCitrine and CONEGI's. Scale bars: 10 μm.

4.1.3. EGFR(BCNKXXX)-QG-mCitrine variants exhibit FRET between mCitrine and Atto590

To experimentally determine whether the labeling of the EGFR(BCNKXXX)-QG-mCitrine variants results in FRET we measured the fluorescence lifetime (τ) of mCitrine over time after addition of tet-Atto590 to cells by FLIM. For all variants we observed a substantial decrease in mCitrine τ from 3.02 ± 0.004 ns to a range from 2.59 ± 0.023 ns to

2.70 ± 0.022 ns depending on the variant over a time course of 20 min after addition of tet-Atto590 (**Fig.17A,B**). This indicated occurrence of FRET between mCitrine and Atto590 conjugated with the BCNK moiety in the CONEGI variants. With a reaction time clearly below 5 min, EGFR(BCNK712/713)-QG-mCitrine exhibited the fastest labeling kinetics, most likely because of the high accessibility of this site. Addition of tet-Atto590 to cells co-expressing EGFR-QG-mCitrine and the BCNK incorporation system did not lead to an alteration in τ of mCitrine over 20 min in the presence of BCNK (**Fig.17B**). This control experiment demonstrated that the observed changes in τ of mCitrine in the CONEGI variants result from specific FRET between the BCNK-bound Atto590 and mCitrine and not because non-specific Atto590 binding to the EGFR or the PM.

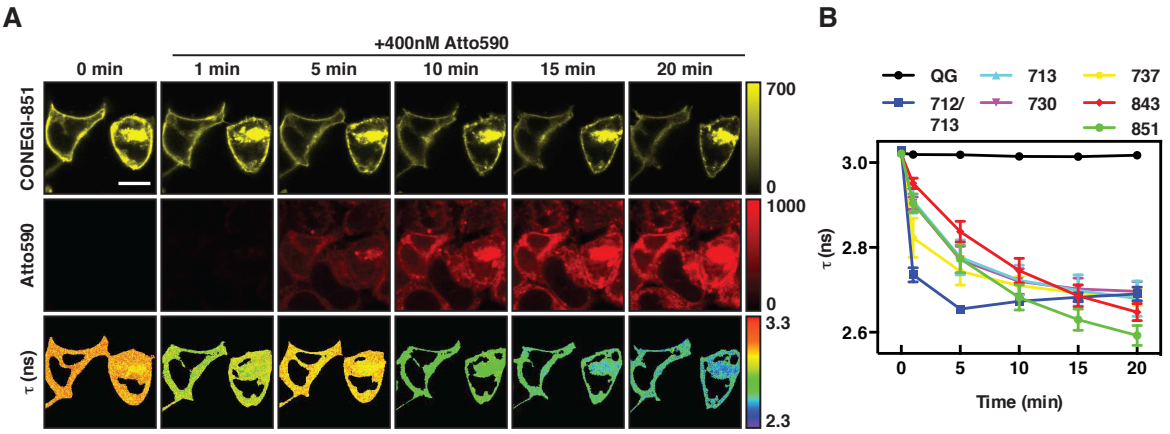

Figure 17: Labeling of EGFR(BCNKXXX)-QG-mCitrine variants with tetrazine-Atto590 lowers τ of mCitrine. A. HEK293T cells expressing EGFR(BCNK851)-QG-mCitrine upon tetrazine-Atto590 addition. Representative mCitrine and Atto590 fluorescence images of CONEGI-851 upon Atto590-labeling and corresponding τ images. Scale bar: 10 µm. **B.** Mean τ of EGFR(BCNK)-QG-mCitrine variants (n=6-17 cells/variant) and EGFR-QG-mCitrine (n=10) upon tetrazine-Atto590 labeling. Error bars: SEM.

To address whether unbound tet-Atto590 affects τ of the CONEGI variants, we removed free, unbound tet-Atto590 after labeling of the EGFR(BCNKXXX)-QG-mCitrine variants. We observed that the washout did not abolish the decrease in τ of mCitrine in the CONEGI variants confirming that the conjugation of tet-Atto590 to BCNK is stable (**Fig.18A,B**). In addition, we obtained negative correlations between τ of mCitrine and the Atto590 fluorescence intensity per cell for all CONEGI variants (**Fig.18C**). Specificity in the FRET between mCitrine and Atto590 was further confirmed by (1) saturation of the binding curves at high Atto590 intensities, (2) the absence of a change in τ (~3 ns) for EGFR-QG-mCitrine upon Atto590 addition (**Fig.18C**) and (3) the increase in τ of each CONEGI variant to mCitrine donor only lifetimes following Atto590 photobleaching (**Fig.18D,E**).

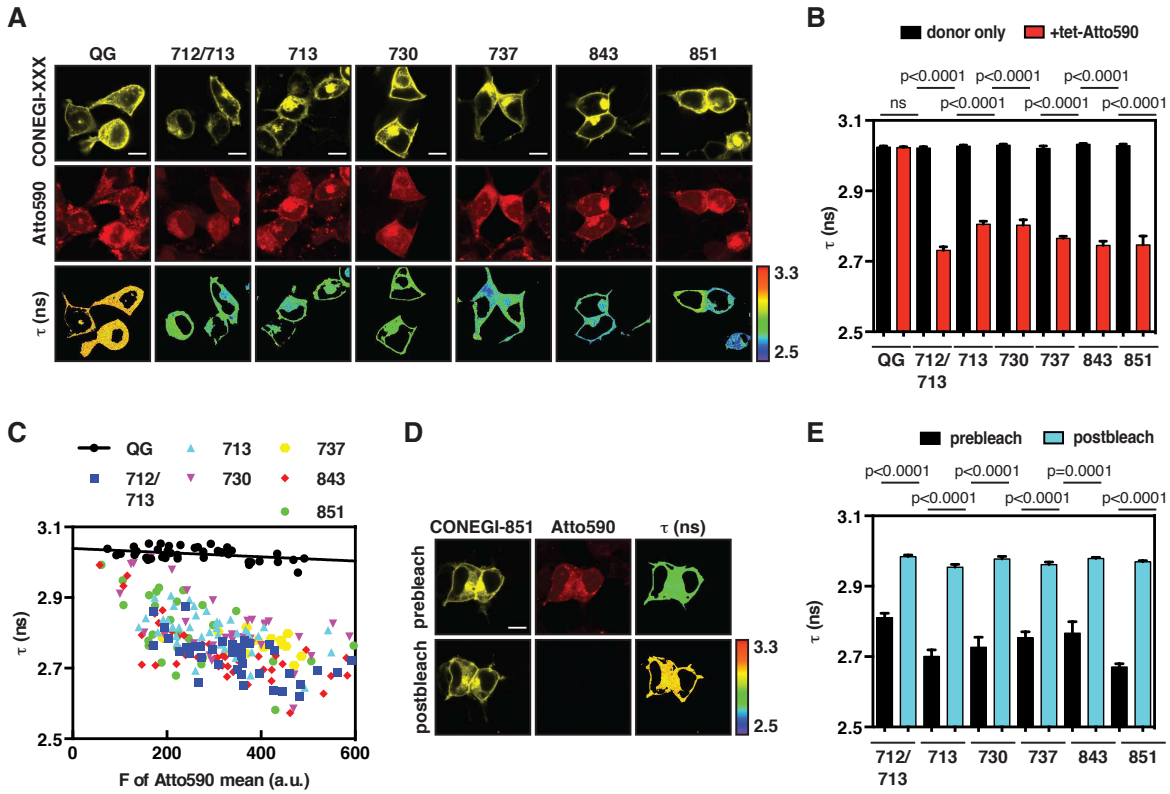

Figure 18: CONEGI variants exhibit specific FRET between mCitrine and Atto590. A. Representative mCitrine and Atto590 fluorescence images of CONEGI's and Atto590-labeled EGFR-QG-mCitrine and corresponding τ images. **B.** Mean τ of EGFR-QG-mCitrine and EGFR(BCNKXXX)-QG-mCitrine variants and their corresponding CONEGI's (unlabeled: n=9-14 cells/variant; Atto590-labeled: n=31-44). **C.** Dependency of τ of EGFR-QG-mCitrine (n=42 cells/variant) and CONEGI's (n=31-44) on the mean fluorescence intensity of Atto590 in individual cells. **D.** Representative mCitrine and Atto590 fluorescence images of CONEGI-851 before and after acceptor photobleaching and corresponding τ images. **E.** Mean τ of CONEGI's (n=8-9 cells/variant) before and after Atto590 photobleaching. Scale bars: 10 μm. Error bars: SEM.

4.1.4. CONEGI reports on conformational changes of TKD upon activation

To examine whether the CONEGI variants report on conformational changes in the TKD upon EGFR activation, CONEGI variants were stimulated with EGF in HEK293T cells and τ of mCitrine was followed over time by FLIM. τ of CONEGI-712/713 significantly increased and τ of CONEGI-737, -843 and -851 significantly decreased upon EGF stimulation as compared to that of EGFR-QG-mCitrine, whereas τ of mCitrine in CONEGI-713 and -730 was unaffected by EGF addition (**Fig.19B-G,I**). τ of mCitrine in EGFR(BCNK851)-QG-mCitrine in the absence of Atto590 and EGFR-QG-mCitrine upon Atto590 addition did not change upon EGF addition precluding photo physical effects that change the τ of mCitrine upon EGF stimulation (**Fig.19A,H,I**). We conclude that an active EGFR conformation correlates with a lower τ of mCitrine in CONEGI-737, -843 and -851

and with a higher τ of mCitrine in CONEGI-712/713 suggesting that these CONEGI variants report distinct EGF-induced conformational changes of the TKD.

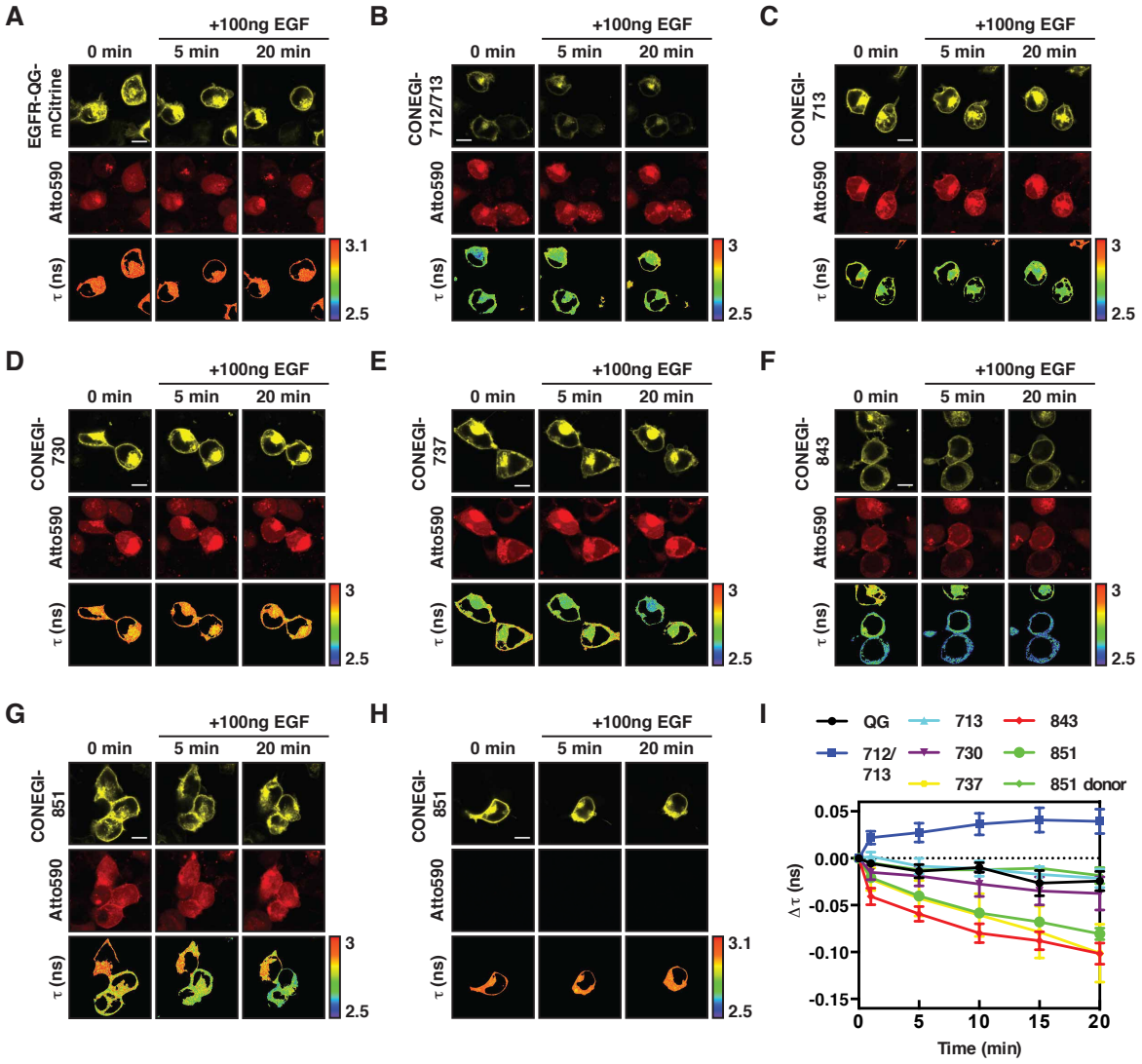

Figure 19: CONEGI reports on conformational changes of the EGFR TKD upon EGFR activation. A.-H. Representative mCitrine and Atto590 fluorescence images of Atto590-labeled EGFR-QG-mCitrine (**A**), CONEGI's (**B-G**) or EGFR(BCNK851)-QG-mCitrine (**H**) and corresponding τ images upon EGF stimulation. Scale bars: 10 μm. **I.** Change in mean τ of CONEGI's (n=4-10 cells/variant), Atto590-labeled EGFR-QG-mCitrine (n=5 cells) and EGFR(BCNK851)-QG-mCitrine upon EGF stimulation. Error bars: SEM.

To examine whether the EGFR(BCNKXXX)-QG-mCitrine variants retain their activity upon BCNK incorporation we quantified the phosphorylation on Y1086 and Y1148 by measuring the recruitment of mCherry-tagged phospotyrosine-binding domain (PTB-mCherry) to EGFR(BCNKXXX)-QG-mCitrine upon EGF stimulation by FLIM[41,102]. We observed recruitment of PTB-mCherry to EGFR(BCNK843)-QG-mCitrine and EGFR(BCNK851)-QG-mCitrine and a consistent decrease in τ of mCitrine in both variants following EGF stimulation, which was comparable to that of EGFR-QG-mCitrine

(**Fig.20F-H**). In contrast, EGF stimulation had only marginal effects on the τ of the other EGFR(BCNKXXX)-QG-mCitrine variants (712/713, 713, 730, and 737) (**Fig.20A-E,H**).

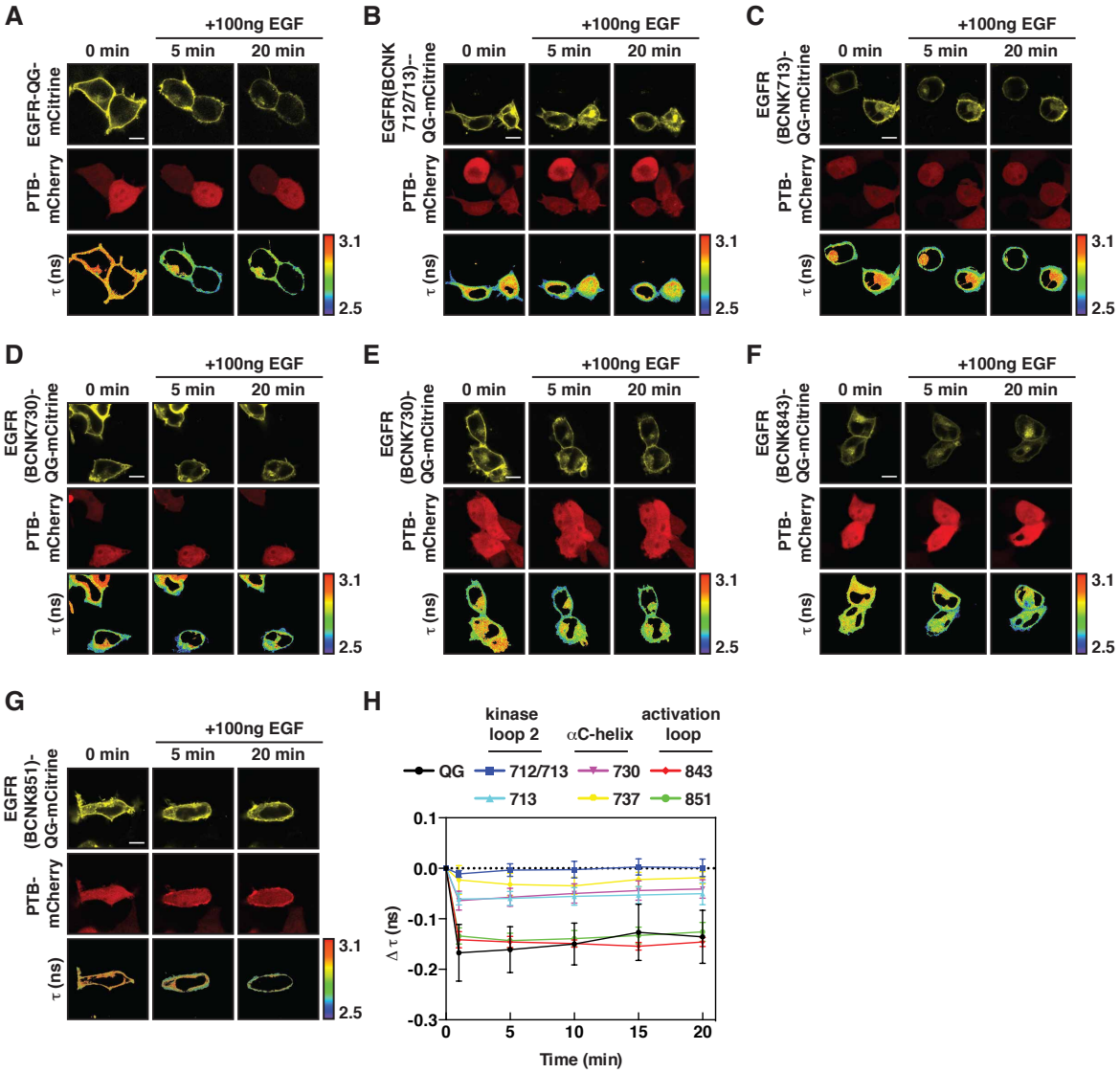

Figure 20: PTB recruitment to EGFR(BCNKXXX)-QG-mCitrine variants upon EGF stimulation. A.-G. Representative fluorescence images of PTB-mCherry and EGFR-QG-mCitrine (**A**) or EGFR(BCNK)-QG-mCitrine variants (**B-G**) and corresponding τ images upon EGF stimulation. Scale bars: 10 μm. **H.** Change of mean τ of mCitrine in CONEGI's (n=5-8 cells/variant) or EGFR-QG-mCitrine (n=4) upon EGF-mediated PTB-mCherry recruitment. Error bars: SEM.

To investigate whether BCNK incorporation and Atto590 labeling affect other EGFR phosphorylation sites we also quantified the relative phosphorylation (pY/EGFR) of the CONEGI variants on the Grb2-binding site Y1068 by Western blot analysis[126]. Consistent with the PTB recruitment, CONEGI-843 and -851 exhibited a similar fold-change in phosphorylation upon EGF stimulation compared to EGFR-QG-mCitrine. The other CONEGI's responded only marginally to EGF (712/713, 713, 730 or 737) (**Fig.21A,B,C**). These observations showed that the EGF-induced formation of a functional asymmetric

receptor dimer is compatible with BCNK incorporation and tet-Atto590 labeling at sites 843 and 851 in the activation loop.

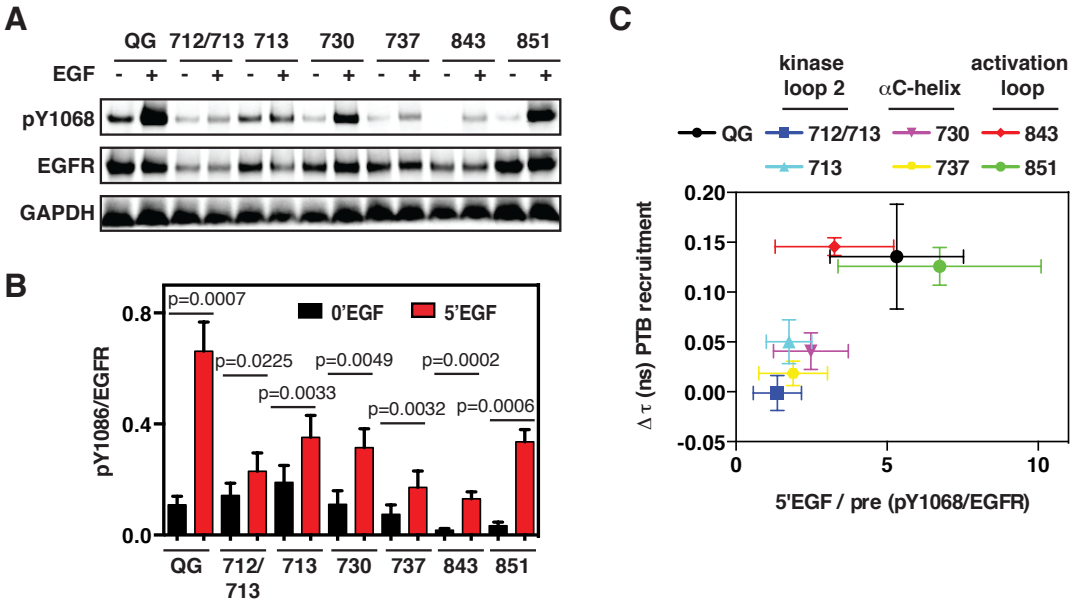

Figure 21: Phosphorylation of CONEGI variants upon EGF stimulation. A. HEK293T cells ectopically expressing CONEGI's or EGFR-QG-mCitrine were stimulated with EGF before lysis. Blots were probed with antibodies against EGFR, pY1068 and GAPDH. **B.** Relative Y1068 phosphorylation level (pY1068/EGFR) of EGFR-QG-mCitrine and CONEGI's before and after 5 min EGF stimulation. n=5. **C.** Fold change in Y1068 phosphorylation (5'EGF/pre) (quantified from **B**) versus change in mean τ of mCitrine upon PTB recruitment following EGF stimulation (quantified from **Fig.21H**) for each CONEGI and EGFR-QG-mCitrine. Error bars: SEM. EGF stimulation: 100 ng/ml.

We thus proceeded with CONEGI-851, because it exhibited the highest expression level, a large change in τ upon EGFR activation and the highest phosphorylation upon EGF stimulation, as well as a fold-change in phosphorylation following EGF addition that was comparable to that of EGFR-QG-mCitrine (**Fig.16A, 19, 21C**). In immunofluorescence stainings against pY1068 in fixed HEK293T cells expressing EGFR(BCNK851)-QG-mCitrine or EGFR-QG-mCitrine we obtained a comparable EGF-induced phosphorylation level at the PM and a slightly reduced autonomous phosphorylation level for EGFR(BCNK851)-QG-mCitrine as compared to EGFR-QG-mCitrine (**Fig22A,B**). This suggests that EGFR(BCNK851)-QG-mCitrine is fully functional and properly folded at the PM, whereas it might be partially unfolded due to protein instability in the cell interior resulting in the lower phosphorylation on Y1068 for whole cell populations (**Fig.21B**). Moreover, we found that neither autonomous nor ligand-dependent phosphorylation of EGFR(BCNK851)-QG-mCitrine was affected by tet-Atto590 labeling (**Fig.22C,D**).

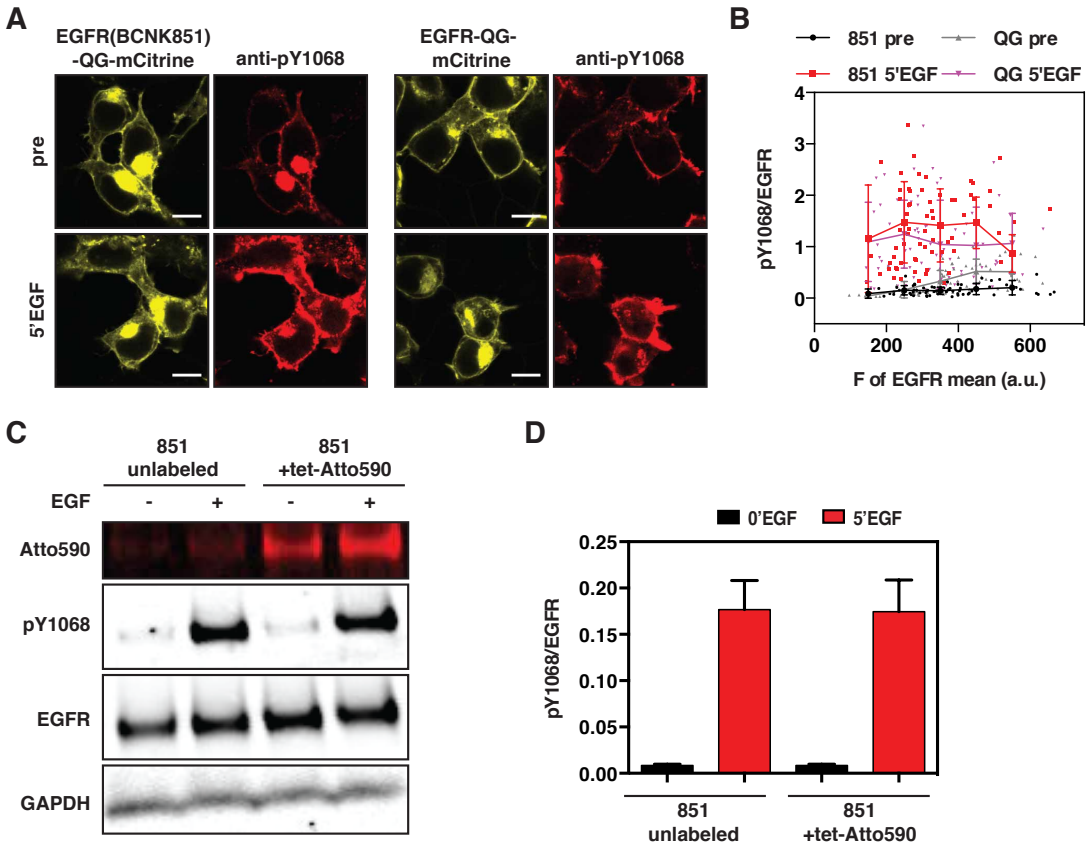

Figure 22: Autonomous and EGF-mediated phosphorylation of CONEGI-851. A. HEK293T cells expressing EGFR(BCNK851)-QG-mCitrine (left panel) or EGFR-QG-mCitrine (right panel) before and after 5 min EGF stimulation were immunostained against pY1068. **B.** Relative Y1068 phosphorylation level (pY1068/EGFR) as quantified from immunofluorescence versus expression level of EGFR-QG-mCitrine and EGFR(BCNK851)-QG-mCitrine before and 5 min after EGF stimulation (n=67-74 cells/condition) in individual cells. Lines connect mean values of binned data. **C.** HEK293T cells ectopically expressing EGFR(BCNK851)-QG-mCitrine were either left unlabeled or labeled for 20 min with tet-Atto590 and stimulated with EGF for 5 min before lysis. Atto590 fluorescence of resulting lysates visualized by in gel fluorescence analysis. Blots were probed with anti-EGFR, anti-pY1068 and anti-GAPDH. **D**. Relative Y1068 phosphorylation level (pY1068/EGFR) of unlabeled and Atto590-labeled EGFR(BCNK851)-QG-mCitrine before and after 5 min EGF stimulation. n=3. Error bars: SEM. EGF stimulation: 100 ng/ml.

4.1.5. CONEGI-851 reports on intramolecular conformational changes in the TKD

To investigate whether FRET and the change in FRET upon EGFR activation detected in CONEGI-851 originates from intra- or intermolecular FRET we measured τ of EGFR-QG-mCitrine (donor only) upon co-expression with an EGFR(BCNK851) variant lacking mCitrine that was labeled with Atto590 (acceptor only). τ of EGFR-QG-mCitrine in the presence of Atto590-labeled EGFR(BCNK851) (2.983 ± 0.008) was comparable to that of EGFR-QG-mCitrine in the presence (3.021± 0.009) or absence (3.038± 0.001) of Atto590, but significantly higher as compared to that of CONEGI-851 (2.746 ± 0.025) (**Fig.23A,B**). EGF induced dimerization of EGFR-QG-mCitrine and Atto590-labeled EGFR(BCNK851)

did not change τ of mCitrine indicating that FRET in CONEGI-851 is intramolecular and not intermolecular due to EGFR self-association (**Fig23C,D**).

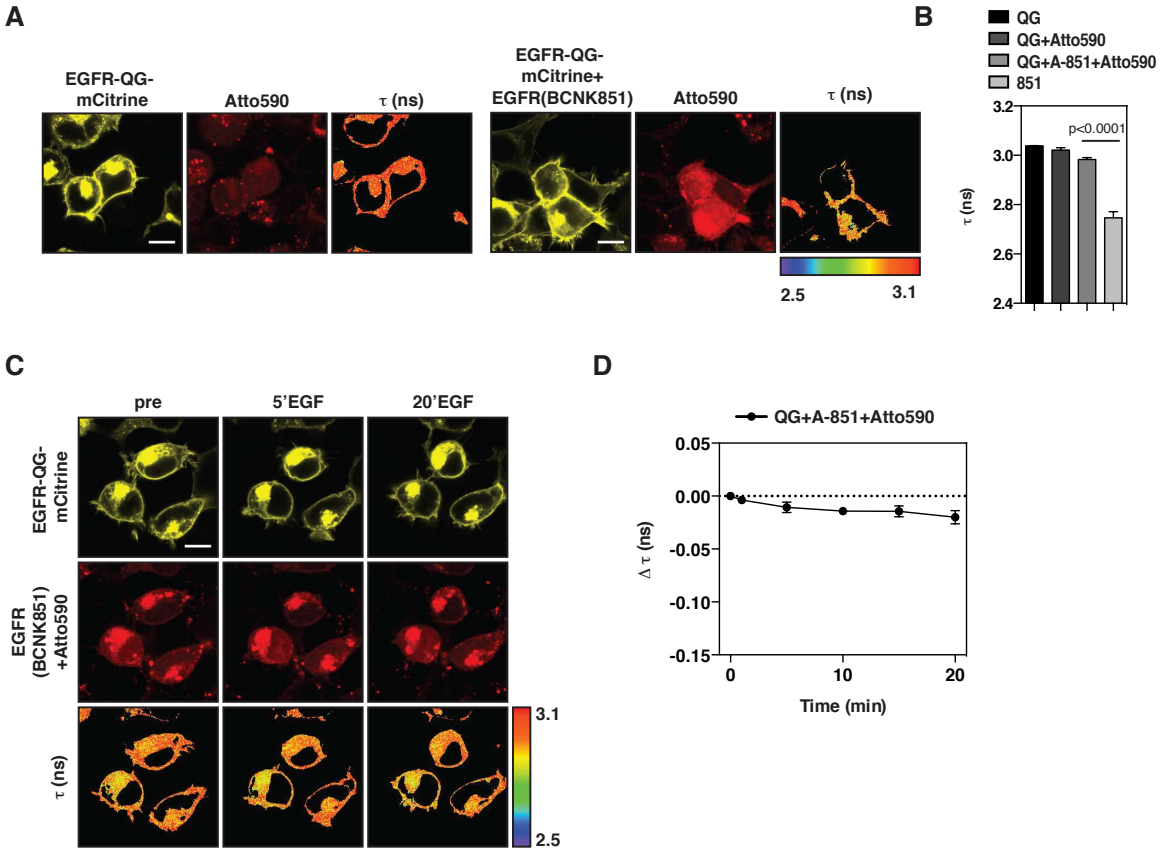

Figure 23: Intramolecular FRET in CONEGI-851. A. Representative mCitrine and Atto590 fluorescence images and corresponding τ of EGFR-QG-mCitrine upon Atto590 addition (left) and EGFR-QG-mCitrine in presence of Atto590-labeled EGFR(BCNK851) (right). **B.** Mean τ of EGFR-QG-mCitrine in absence (QG) or presence of tetrazine-Atto590 (QG+Atto590), EGFR-QG-mCitrine in presence of Atto590-labeled EGFR(BCNK851) (QG+A-851+Atto590) and CONEGI-851 (n=6-36 cells/condition). **C.** Representative mCitrine and Atto590 fluorescence images and corresponding τ of EGFR-QG-mCitrine and Atto590-labeled EGFR(BCNK851) upon EGF stimulation. **D.** Change in mean τ of EGFR-QG-mCitrine (n=7 cells) in presence of Atto590-labeled EGFR(BCNK851) upon EGF stimulation. Scale bars: 10 μm. Error bars: SEM. EGF stimulation: 100 ng/ml.

4.1.6. EGFR monomers can adopt an active conformation

We investigated whether self-association of EGFR is required to induce and stabilize the active conformation in CONEGI-851. Therefore, we compared the self-association of EGFR as well as the conformational state of the TKD in CONEGI-851 upon autonomous activation induced by the phosphatase inhibitor pervanadate (PV) to that upon EGF stimulation[128]. The self-association of EGFR at the PM was determined by measuring homo-FRET between mCitrine using fluorescence anisotropy[129] and the TKD conformation was obtained by FLIM.

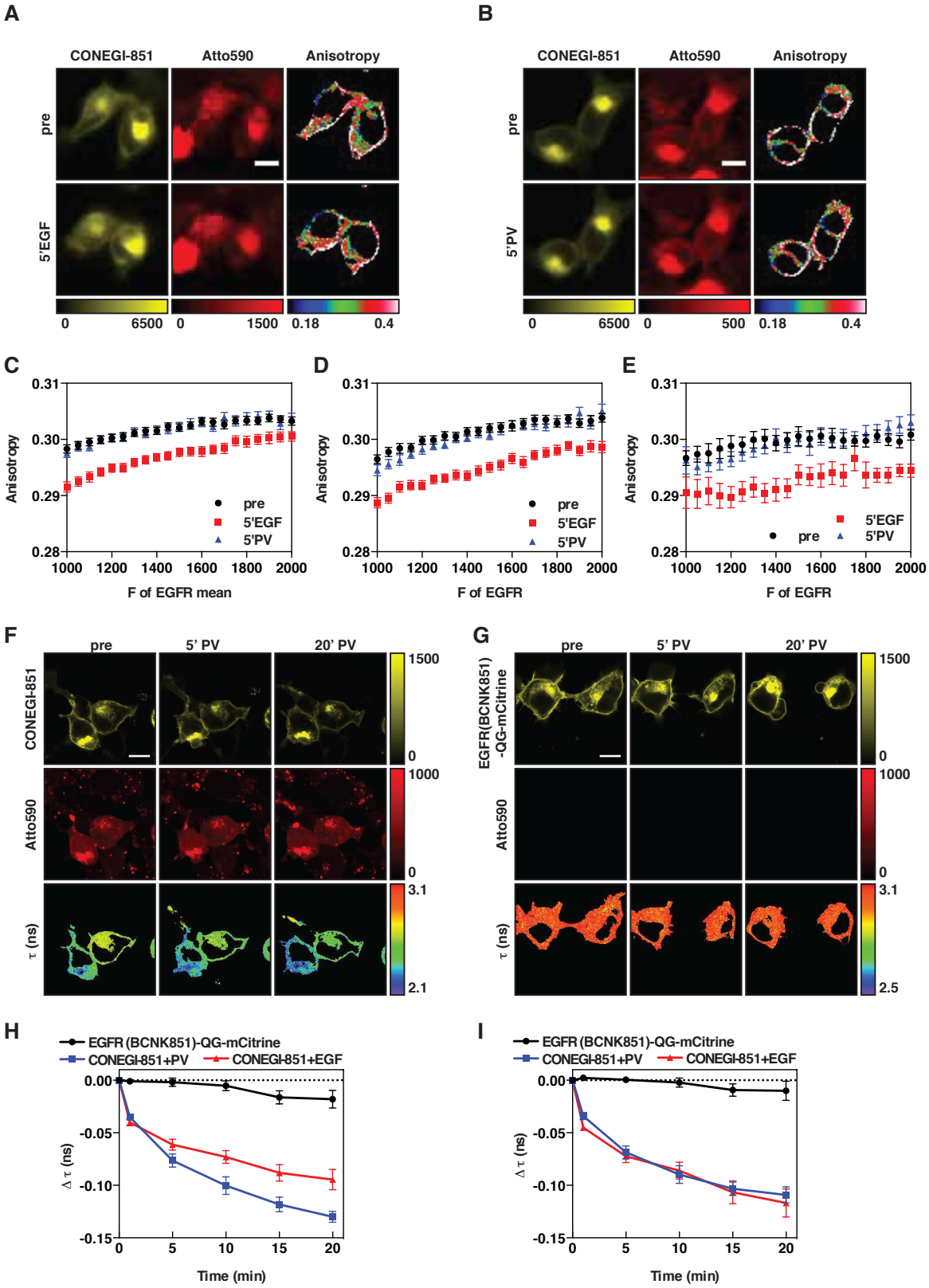

Figure 24: EGFR monomers can adopt an active conformation. A. and B. Representative mCitrine and Atto590 fluorescence images of CONEGI-851 and corresponding mCitrine anisotropy images upon EGF (**A**) or PV (**B**) treatment. **C.-E.** Anisotropy of CONEGI-851 (**C**), EGFR(BCNK851)-QG-mCitrine (**D**) or EGFR-QG-mCitrine (**E**) versus its binned mean fluorescence intensity (F of EGFR) per pixel before (black), after EGF (red) or PV (blue) treatment. **F. and G.** Representative fluorescence images of CONEGI-851 (**F**) or EGFR(BCNK851)-QG-mCitrine (**G**) and corresponding τ upon PV stimulation. Scale bars: 10 µm. **H. and I.** Change in mean τ of EGFR(BCNK851)-QG-mCitrine (n=4 cells) and CONEGI-851 (n=10) upon PV

treatment and of CONEGI-851 (n=20) upon EGF stimulation over whole cells (**H**) or PM (**I**). Error bars: SEM. EGF stimulation: 100 ng/ml. PV treatment: 0.33 mM.

EGF stimulation resulted in a drop of anisotropy for CONEGI-851, EGFR(BCNK851)-QG-mCitrine and EGFR-QG-mCitrine showing that anisotropy is a good measure for dimerization of CONEGI-851 (**Fig24A,C-E**). This also demonstrated that tet-Atto590 labeling does not affect dimerization of CONEGI-851. In contrast, the anisotropy of CONEGI-851, EGFR(BCNK851)-QG-mCitrine and EGFR-QG-mCitrine remained unchanged upon PV-induced EGFR phosphorylation (**Fig.24B-E**). These data demonstrate that the bulk of autonomously activated EGFR is in a monomeric state[123,130]. The comparable change in τ of mCitrine in CONEGI-851 upon EGF and PV treatment that was dependent on the presence of Atto590 (**Fig.24F-I**) suggests that active monomeric and active dimeric receptors sample a similar active conformation. However, the decrease in τ of mCitrine in CONEGI-851 upon PV addition over whole cells was larger as compared to that upon EGF stimulation, which can be explained by EGFR activation at all membranes in the cell upon PV treatment, whereas EGF initially activates the receptor only at the PM.

4.1.7. Conformational changes in CONEGI-851 depend on EGFR kinase activity

To investigate whether kinase activity is necessary to induce and maintain an active conformation in CONEGI-851 we measured the conformational state of the TKD upon EGF and PV treatment in the presence of the EGFR inhibitor AG1478 that binds to the catalytic site of the TKD and blocks EGFR activity[131]. The presence of 1 μM AG1478 nearly abolished the change in τ of mCitrine in CONEGI-851 upon EGF and PV treatment and the residual drop in τ was comparable to that upon AG1478 treatment alone (**Fig.25A,B**). This confirmed that measuring τ in CONEGI-851 enables to distinguish between an active and inactive TKD conformation. Phosphorylation of Y845 and Y1068 was suppressed upon EGF stimulation in the presence of 1 μM EGFR inhibitors (AG1478, Lapatinib, Gefitinib or Erlotinib)[132–134], whereas Y845 and to a lesser extent Y1068 was phosphorylated upon PV stimulation in the presence of EGFR inhibitors (**Fig.25C-F**). PV-induced Y845 phosphorylation in the presence of inhibitor was significantly lower as compared to that in the absence of inhibitor indicating that the EGFR kinase activity substantially contributes to Y845 phosphorylation. However, this also shows that Y845 phosphorylation alone is not sufficient to stabilize an active conformation and that other kinases (e.g. Src) can phosphorylate Y845[135].

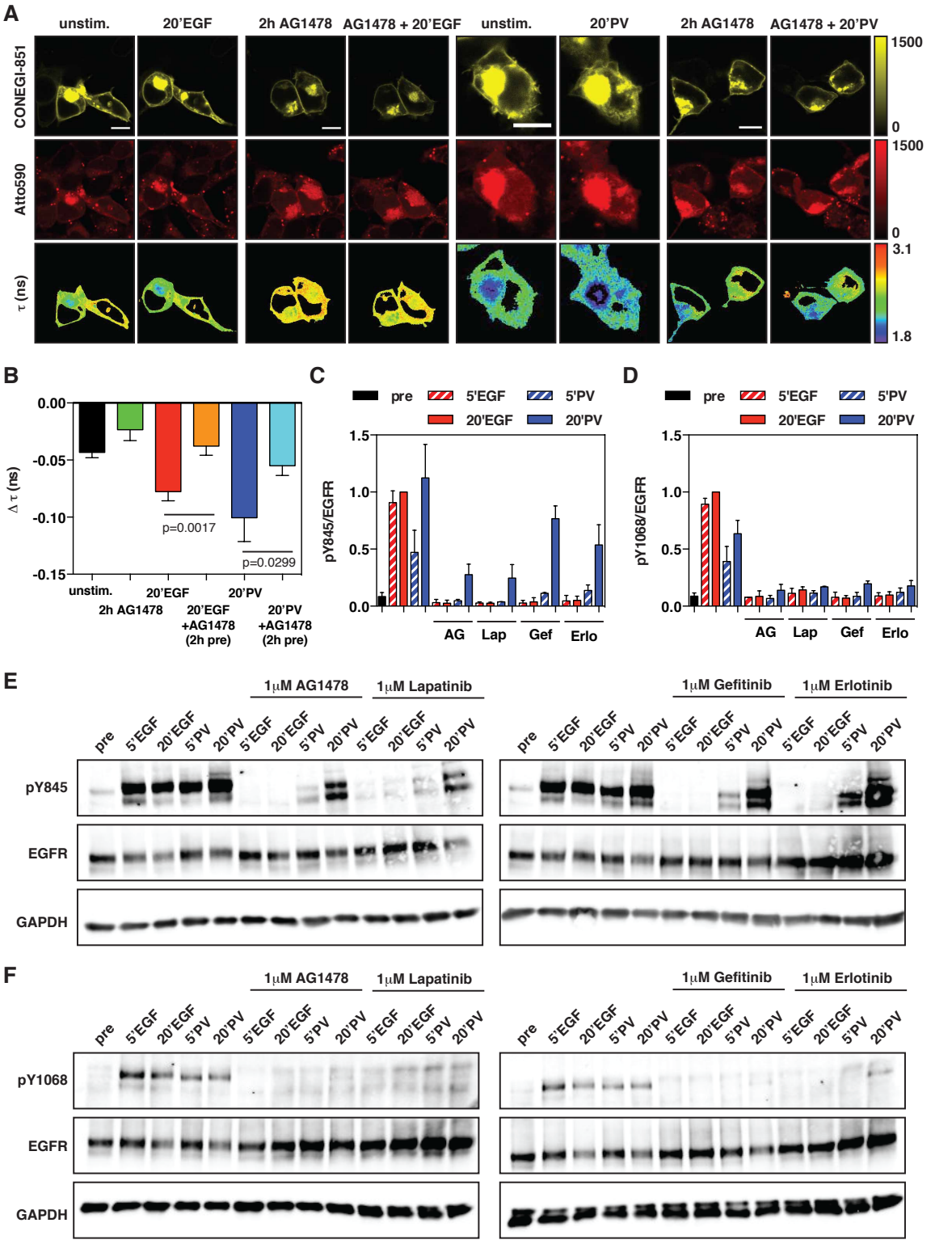

Figure 25: The stabilization of an active conformation in CONEGI-851 depends on its kinase activity. **A.** Representative mCitrine and Atto590 fluorescence images CONEGI-851 and corresponding τ upon EGF or PV treatment in absence or presence of 1 μM AG1478. Scale bars: 10 μm. **B.** Change in mean τ of CONEGI-851 either left untreated, incubated with 1 μM AG1478 or upon 20 min EGF or PV treatment in absence or presence (2 h pre-incubation) of 1 μM AG1478 (n=6-27 cells/condition). **C. and D.** Relative phosphorylation level on Y845 (**C**) or Y1068 (**D**) (pY/EGFR) of CONEGI-851 before and after 5 min and 20 min EGF or PV stimulation in absence or presence (2 h pre-incubation) of 1 μM EGFR inhibitor (AG1478, Lapatinib, Gefitinib and Erlotinib). n=3. Error bars: SEM. **E. and F.** HEK293T cells ectopically expressing CONEGI-851 were either left untreated or stimulated for 5 min and 20 min with EGF or PV in absence or

presence (2 h pre-incubation) of 1 μM EGFR inhibitor (AG1478, Lapatinib, Gefitinib and Erlotinib). EGFR expression was detected by an anti-EGFR antibody and EGFR phosphorylation by an anti-pY845 (**E**) or anti-pY1068 (**F**) antibody. GAPDH was used as a loading control. EGF stimulation: 100 ng/ml. PV treatment: 0.33 mM.

4.1.8. Dependence of autonomous, autocatalytic EGFR activation on Y845 phosphorylation

To examine the dependency of autonomous, autocatalytic activation on Y845 phosphorylation we compared the conformational state of the TKD and phosphorylation on Y1068 of CONEGI-851 WT (CONEGI-WT) and a CONEGI-851 Y845F mutant (CONEGI-Y845F). This was performed for single cells by FLIM and immunofluorescence staining against pY1068 and for cell populations by Western blot analysis. CONEGI-WT exhibited a lower τ of mCitrine and was more prone to auto-phosphorylation on Y1068 at all EGFR concentrations as compared to CONEGI-Y845F (**Fig.26A,B,C**). Furthermore, Y1068 phosphorylation increased in an EGFR concentration-dependent manner (**Fig.26A**). These results indicated that phosphorylation of Y845 stabilizes the TKD in an active conformation of EGFR monomers resulting in auto-phosphorylation on Y1068. To uncouple autonomous, autocatalytic activation of EGFR from dephosphorylation by phosphatases, we used PV to inhibit phosphatase activity. The change in τ of CONEGI-WT and phosphorylation on Y1086, following addition of PV, was significantly higher for CONEGI-WT compared to CONEGI-Y845F (**Fig.26D,E**). This corroborates that Y845 phosphorylation in EGFR monomers stabilizes an active conformation resulting in autocatalytic amplification of EGFR activity and also shows that autocatalytic EGFR activation is counterbalanced by dephosphorylation of Y845 at the PM in steady state. However, the detection of a change in FRET of CONEGI-Y845F upon PV and an increase in its Y1068 phosphorylation indicated that an additional posttranslational modification or allosteric interaction is involved in the autocatalytic activation mechanism.

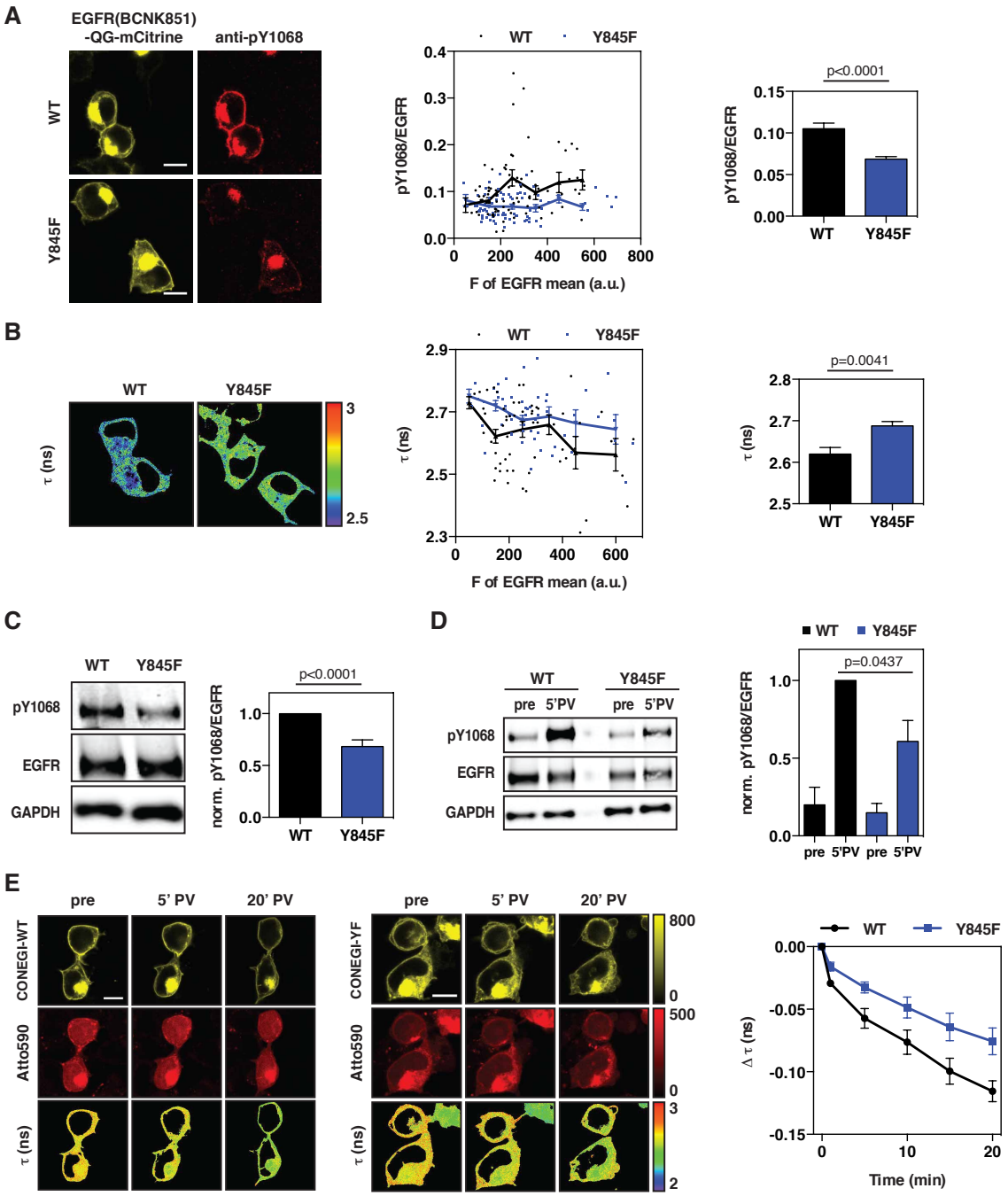

Figure 26: Y845 phosphorylation enhances autonomous EGFR activity. A. HEK293T cells expressing EGFR(BCNK851)-QG-mCitrine-WT or -Y845F were immunostained against pY1068. Fluorescence images of EGFR(BCNK851)-QG-mCitrine-WT or -Y845F and anti-pY1068 (left). Dependency of relative Y1068 phosphorylation (pY1068/EGFR) on mean expression level of EGFR(BCNK851)-QG-mCitrine-WT (n=80 cells) and -Y845F (n=81) in individual cells. Lines connect mean values of binned data (middle). Relative Y1068 phosphorylation (pY1068/EGFR) of EGFR(BCNK851)-QG-mCitrine-WT and -Y845F (right). **B.** Representative τ images of mCitrine in CONEGI-WT or -Y845F (left). Dependency of τ of mCitrine on mean expression level of CONEGI-WT (n=64 cells) and -Y845F (n=56) in individual cells. Lines connect mean values of binned data (middle). Mean τ of mCitrine in CONEGI-WT and -Y845F (right). **C.** HEK293T cells ectopically expressing CONEGI-WT or -Y845F were used for Western blot analysis. Blots were probed for anti-EGFR, anti-pY1068 and anti-GAPDH (left). Relative Y1068 phosphorylation level (pY1068/EGFR) of CONEGI-WT or -Y845F in absence of ligand (right). n=15. **D.** HEK293T cells ectopically expressing CONEGI-WT or -Y845F were stimulated with PV before lysis. Blots were probed for anti-EGFR, anti-pY1068 and anti-GAPDH (left). Relative Y1068 phosphorylation level (pY1068/EGFR) of CONEGI-WT or -Y845F before and after 5 min PV stimulation (right). n=3. **E.** Representative mCitrine and Atto590 fluorescence images and corresponding τ of CONEGI-WT (left) or –Y845F (middle) upon PV stimulation.

Change in mean τ of CONEGI-WT (n=11 cells) and -Y845F (n=11) upon PV treatment (right). Scale bars: 10 μm. Error bars: SEM. PV treatment: 0.33 mM.

4.1.9. Dependence of EGF-mediated, autocatalytic EGFR activation on Y845 phosphorylation

To investigate whether EGFR activation upon EGF stimulation only relies on asymmetric dimer formation or also on the autocatalytic activation mechanism, we stimulated CONEGI-WT and CONEGI-Y845F with increasing EGF concentrations and compared the phosphorylation on the Shc-binding site Y1173[136] and the Grb2-binding site Y1068 by Western blot analysis. We observed lower phosphorylation and obtained a decrease in EGF potency for CONEGI-Y845F (Y1173: EC_{50}: 17.80 ng/ml; Y1068: EC_{50}: 9.363 ng/ml) as compared to CONEGI-WT (Y1173: EC_{50}: 10.81 ng/ml; Y1068: EC_{50}: 9.265 ng/ml) for both phospho-sites (**Fig.27A-D**). This suggested that ligand-bound dimeric EGFR can activate EGFR monomers by stabilizing an active conformation thereby promoting autocatalytic activation.

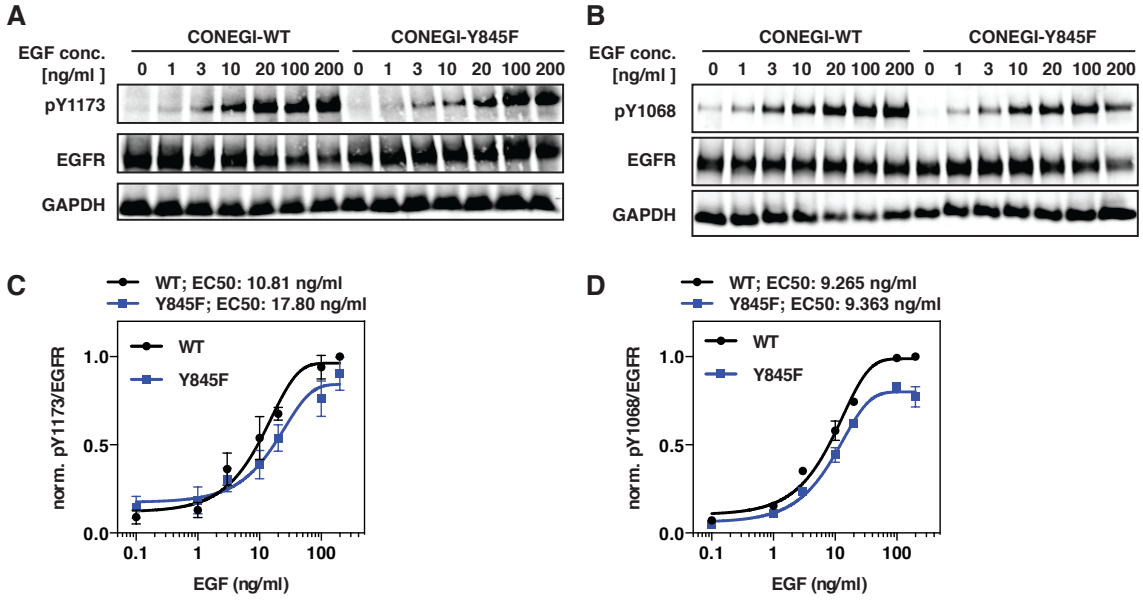

Figure 27: EGF-dose-dependent phosphorylation on Y1068 and Y1173 of CONEGI-851. A. and B. HEK293T cells ectopically expressing CONEGI-WT or -Y845F were stimulated with increasing doses EGF for 10 min before lysis. Blots were probed for anti-EGFR, anti-pY1173 (**A**) or anti-pY1068 (**B**) and anti-GAPDH. **C. and D.** Relative phosphorylation level (**C**: pY1173/EGFR; **D**: pY1068/EGFR) of CONEGI-WT and CONEGI-Y845F upon stimulation with increasing doses EGF for 10 min. pY1173: n=4 blots; pY1068: n=3. Error bars: SEM.

To further investigate the dependence of autocatalytic activation on the EGF dose we compared the temporal profile of Y1068 phosphorylation by Western blot analysis of CONEGI-WT and CONEGI-Y845F upon stimulation with a high, saturating EGF

concentration (100 ng/ml) and a low, non-saturating concentration (20 ng/ml). We used this experimental design to compare EGFR phosphorylation of monomeric autocatalytically activated EGFR at low EGF doses to that of ligand-bound allosterically activated dimeric EGFR upon saturating EGF concentrations. CONEGI-WT similar increased in phosphorylation on Y1068 upon 20 ng/ml EGF as compared to that of CONEGI-WT and CONEGI-Y845F upon stimulation with 100 ng/ml EGF, but phosphorylation on Y1068 was higher compared to that of CONEGI-Y845F upon stimulation with 20 ng/ml EGF (**Fig.28E,F,H**). These data demonstrate that Y845 phosphorylation is necessary to induce autocatalytic monomer activation by EGF-bound EGFR dimers at low ligand doses to amplify EGFR phosphorylation. To address whether ligand-activated EGFR can directly activate EGFR monomers by Y845 phosphorylation we monitored the conformational state of the TKD of CONEGI-WT and CONEGI-Y845F upon 20 ng/ml and 100 ng/ml EGF over time (**Fig.28A-D,G**). CONEGI-WT exhibited a similar change in τ upon 20 or 100 ng/ml EGF stimulation, indicating that the autocatalytic activation of EGFR monomers at sub-saturating EGF concentrations generates a similar fraction of EGFR molecules adopting an active conformation to saturating EGF concentrations when EGFR exists primarily as an asymmetric dimer. Following 100 ng/ml EGF stimulation, the change in τ of mCitrine of CONEGI-Y845F was similar to that induced for CONEGI-WT. However, upon 20 ng/ml EGF the change in τ was significantly lower than for CONEGI-WT, demonstrating that the active conformation in monomers of CONEGI-Y845F cannot efficiently be stabilized by liganded dimers due to the lack of Y845 phosphorylation.

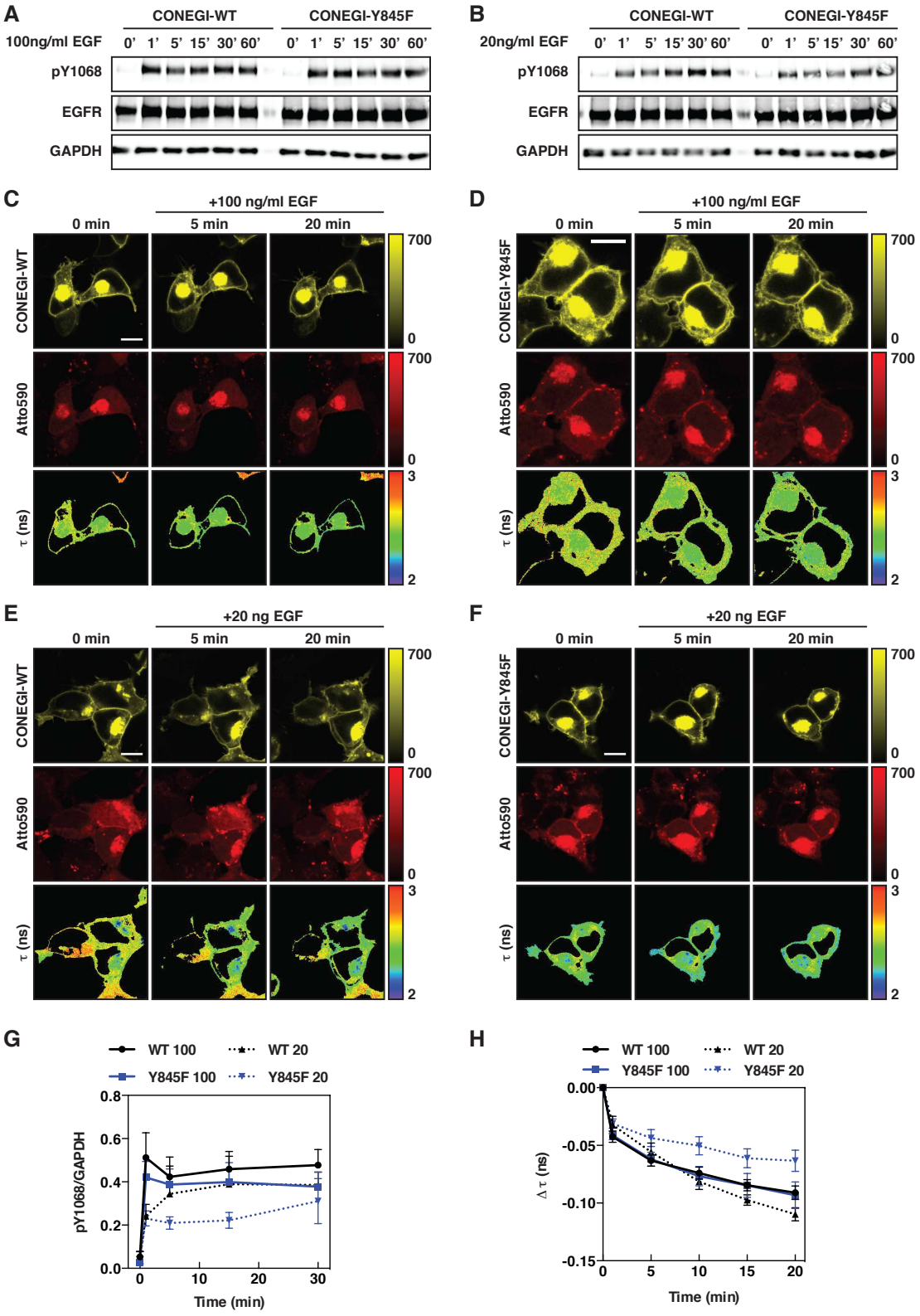

Figure 28: Autocatalytic EGFR activation depends on Y845 phosphorylation. A. and B. CONEGI-WT or -Y845F upon stimulation with 100 ng/ml (A) or 20 ng/ml (B) EGF. Blots were probed for anti-EGFR, anti-pY1068 and anti-GAPDH. **C.-F.** Representative mCitrine and Atto590 fluorescence images and corresponding τ of CONEGI-WT (C and E) or -Y845F (D and F) upon stimulation with 100 ng/ml (**C and D**) or 20 ng/ml (**E and F**) EGF. Scale bars: 10 µm. **G.** Relative Y1068 phosphorylation (pY1068/EGFR) of CONEGI-WT and -Y845F upon stimulation with 20 ng/ml or 100 ng/ml EGF. n=3. **H.** Change in mean τ of mCitrine in CONEGI-WT and -Y845F upon stimulation with 20 ng/ml (WT: n=7 cells; Y845F: n=8) or 100 ng/ml EGF (WT: n=16; Y845F: n=16). Error bars: SEM.

4.2. Spatial regulation of EGFR activity by vesicular trafficking

Thermal fluctuations that overcome auto-inhibitory structural features allow autonomous EGFR phosphorylation at high receptor concentrations even in the absence of ligand. This can promote autocatalytic amplification of EGFR activation resulting in uncontrolled EGFR phosphorylation. Protein tyrosine phosphatases (PTPs) such as PTP1B were shown to counterbalance phosphorylated, internalized EGFR with highest activity in pericentriolar areas upon EGF stimulation[67]. Hence, we investigated whether vesicular trafficking is involved in the regulation of autonomous, autocatalytic EGFR activity to suppress uncontrolled EGFR activation in the absence of ligand.

4.2.1. Dependence of autonomous EGFR phosphorylation on EGFR expression

The autocatalytic activation mechanism of EGFR results in self-activation at high cell surface concentrations even in the absence of ligand. To investigate the dependency of the EGFR activity on its concentration at the PM, the phosphorylation of the autocatalytic Y845, the c-Cbl docking site Y1045 and the signaling site Y1068 were measured using a broad range of receptor expression levels achieved by ectopic expression of EGFR-mCitrine. The expression level of EGFR is represented as the n-fold expression of the endogenous EGFR expression level, which was determined in a separate experiment (data not shown)[123]. Immunofluorescence antibody staining against the three tyrosine residues was performed to measure EGFR phosphorylation in single cells (**Fig.29A**). In the absence (black dots) of ligand, auto-phosphorylation varied between individual cells with similar expression levels. Despite this cell-to-cell variance, the average phosphorylation of the different phosphorylation sites increased with higher EGFR expression for all tyrosine residues. The increase in phosphorylation was more pronounced for Y845 (-sixfold) and Y1068 (-eightfold) as compared to Y1045 (-twofold). EGF stimulation (red dots) elevated the phosphorylation level of all tyrosine residues. For Y845 and Y1068 the phosphorylation level increased in an EGFR concentration-dependent manner, whereas phosphorylation on Y1045 increased independent of EGFR density (**Fig.29B**). To compare autonomous phosphorylation levels between the different tyrosine residues, the ratio of the relative EGFR phosphorylation (pY/EGFR) before and after EGF stimulation was calculated for each site. This ‘ratio’ (pre/2’EGF) gives a comparable measure of autonomous phosphorylation levels for the different tyrosine residues independent of antibody affinities for the phosphorylated tyrosine residues. Analysis revealed that the

autocatalytic site Y845 and the signaling site Y1068 are more prone to autonomous phosphorylation than the Cbl-docking site Y1045 in EGFR-mCitrine expressing cells (**Fig.29C**).

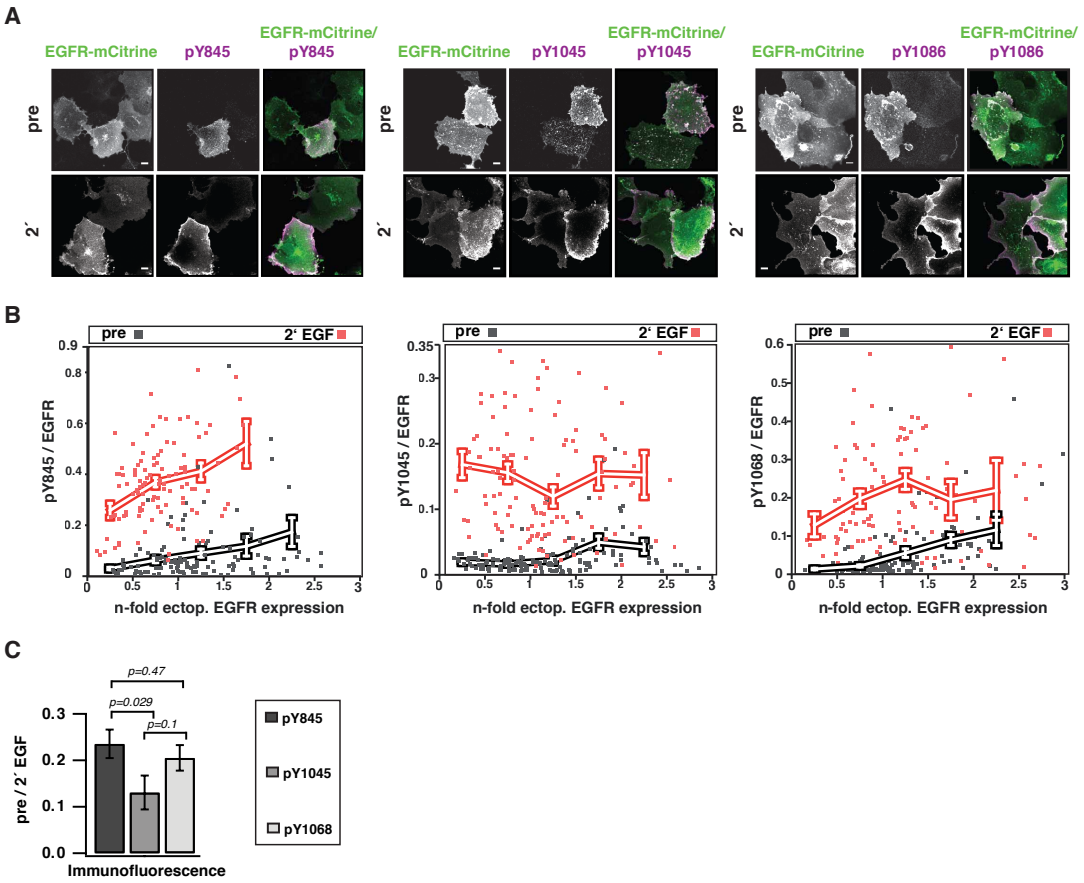

Figure 29: Dependency of Y845, Y1045 and Y1068 phosphorylation on EGFR expression. **A.** Representative fluorescence images of Cos7 cells ectopically expressing EGFR-mCitrine stained with antibody against pY845 (left), pY1045 (middle) or pY1068 (right) and corresponding green/magenta overlays before and after 2 min EGF stimulation. Scale bars: 10 µm. **B.** Relative phosphorylation level of pY845, pY1045 and pY1068 (pY/EGFR) versus EGFR expression level (n-fold ectopic EGFR expression). Data points represent individual Cos7 cells (black: pre; red: 2'EGF; n=87-145). Lines connect mean values of binned data. **C.** Relative phosphorylation level (pY/EGFR) of pY845, pY1045 and pY1068 before EGF stimulation normalized to the relative phosphorylation level (pY/EGFR) after 2 min EGF stimulation. Error bars: SEM. EGF stimulation: 100 ng/ml. (Experiments were performed by Dr. Georgia Xouri and analysed by Martin Baumdick with the help of Malte Schmick).

Population-based Western blot analysis of lysates of Cos7 cells transfected with increasing amounts of EGFR-mCitrine cDNA (0.5 µg, 1.5 µg, 3 µg) to control EGFR expression levels showed the same positive correlation between relative phosphorylation (pY/EGFR) and receptor expression for all three tyrosine residues (**Fig.30A,B**). Here, the relative EGFR phosphorylation increased with receptor concentration for both autonomous and EGF-dependent activation at all tyrosine residues. Calculation of the 'ratio' of relative EGFR phosphorylation (pY/EGFR) before and after EGF stimulation allowed the comparison of autonomous phosphorylation between the individual tyrosine residues, and

displayed a similar phosphorylation profile to that observed by immunofluorescence. Y845 and Y1068 exhibited significantly higher phosphorylation than the Cbl-docking site Y1045 (**Fig.30C**).

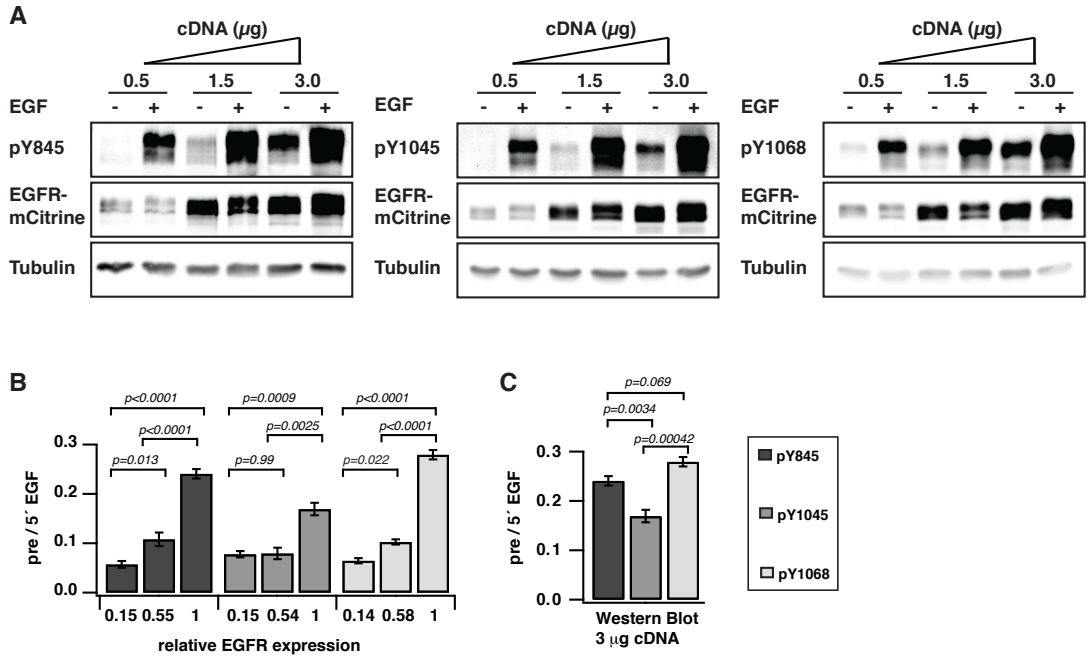

Figure 30: Dependency of Y845, Y1045 and Y1068 phosphorylation on EGFR expression levels. A. Cos7 cells transfected with increasing cDNA amounts of EGFR-mCitrine were lysed before or after 5 min EGF stimulation and used in Western blot analysis. Blots were probed for anti-GFP (EGFR), anti-tubulin and anti-pY845, anti-pY1045 or anti-pY1068. **B.** Relative phosphorylation level (pY/EGFR) on Y845, Y10145 and Y1068 for different EGFR expression levels before EGF stimulation normalized to the relative phosphorylation after 5 min EGF stimulation. The ordinate represents the fraction of EGFR band over tubulin relative to 3 μg that was set to 1. Y845: n=5; Y1045 and Y1068: n=3. **C.** Relative phosphorylation level (pY/EGFR) of pY845, pY1045 and pY1068 in absence of ligand over its relative phosphorylation level (pY/EGFR) upon EGF stimulation. Data correspond to the highest level of EGFR-mCitrine expression (3 μg). Error bars: SEM. EGF stimulation: 100 ng/ml.

The magnitude of EGFR phosphorylation depends on both its kinase activity and the counterbalancing phosphatase activity. To disentangle kinase from phosphatase activity, the thiol-reactive agent PV was used to induce EGFR phosphorylation through inhibition of PTP activity. In this way, the phosphorylation level reflects the intrinsic catalytic efficiency of the EGFR kinase for the three tyrosine residues. Western blot analysis of Cos7 cell lysates expressing EGFR-mCitrine showed that the ratio of relative EGFR phosphorylation (pY/EGFR) after 5 min PV treatment over pre stimulation revealed a 10-times increase at Y845, a 6-fold increase at Y1045 and a 5-fold increase at Y1068 (**Fig.31A,B**). This shows that PTP activity constitutively suppresses EGFR phosphorylation on all three tyrosines in the absence of ligand, but also indicates that Y845 requires higher PTP activity to be suppressed as compared to the other two tyrosines. Moreover, the similar PTP activity acting on Y1045 and Y1068 reveals that the lower

autonomous phosphorylation of Y1045 as compared to Y1068 originates from a lower catalytic efficiency of the kinase for this site as opposed to having a greater sensitivity to PTP-mediated dephosphorylation. Calculation of the ratio of relative EGFR phosphorylation after 5 min PV treatment as compared to 5 min EGF stimulation (5'PV/5'EGF) revealed that the autocatalytic Y845 was 2.5 times more phosphorylated by PV, whereas Y1045 and Y1068 showed similar increases in phosphorylation for PV and EGF (**Fig.31C**). These data indicate that also EGF-induced Y845 phosphorylation is significantly suppressed by PTPs. This is necessary to control autocatalytic activation, because Y845 phosphorylation stabilizes the active conformation of the TKD and thereby would amplify EGFR phosphorylation resulting in uncontrolled activation.

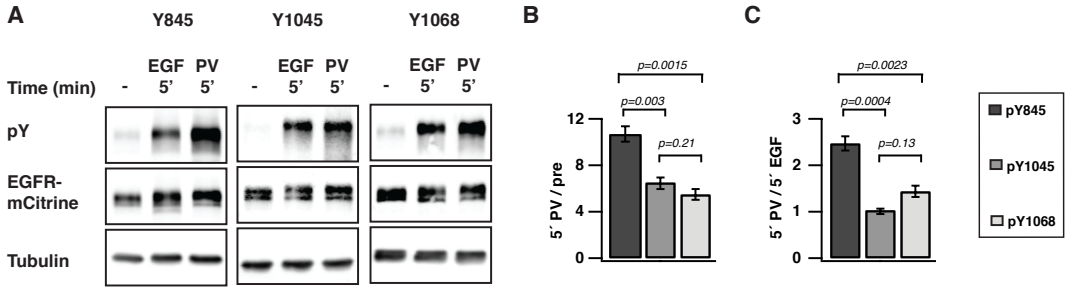

Figure 31: EGFR phosphorylation upon PTP inhibition by PV. A. Cos7 cells ectopically expressing EGFR-mCitrine were stimulated with EGF or PV for 5 min and the resulting lysates were used in Western blot analysis. Blots were probed for anti-GFP (EGFR), anti-tubulin and anti-pY845, anti-pY1045 or anti-pY1068. **B.** Relative EGFR phosphorylation (pY/EGFR) on Y845, Y1045 and Y1068 upon 5 min PV normalized to relative phosphorylation level (pY/EGFR) before PV stimulation. n=3. **C.** Relative EGFR phosphorylation (pY/EGFR) upon 5 min PV treatment normalized to relative EGFR phosphorylation (pY/EGFR) upon 5 min EGF stimulation. Error bars: SEM. EGF stimulation: 100 ng/ml. PV treatment: 0.33 mM. (Performed and analyzed together with Yannick Brüggemann).

4.2.2. Autonomously activated EGFR remains in a monomeric state

To relate the distinct phosphorylation pattern of autonomously and ligand-activated EGFR to the self-association state of EGFR, we performed fluorescence anisotropy microscopy to detect homo-FRET of EGFR-mCitrine. Since EGFR-mCitrine exhibited no homo-FRET upon EGF-induced receptor clustering (data not shown) we used the EGFR-QG-mCitrine construct established for the CONEGI development that also displayed a similar phosphorylation response to EGF in Cos7 cells as compared to EGFR-mCitrine (**Fig.32A,B**).

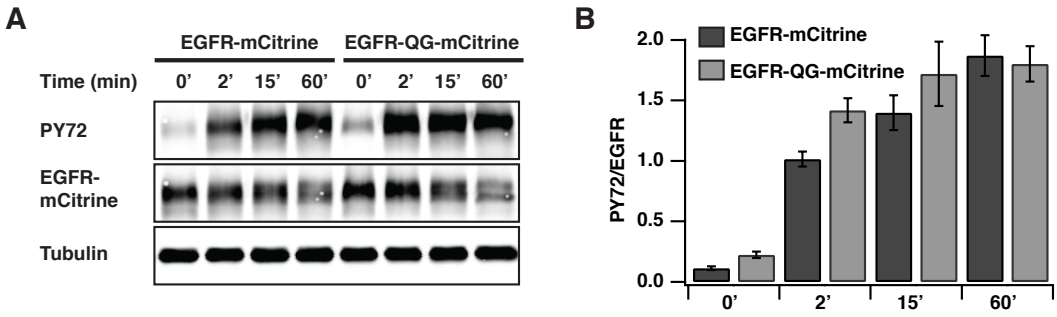

Figure 32: Phosphorylation of EGFR-QG-mCitrine compared to EGFR-mCitrine. A. Cos7 cells ectopically expressing EGFR-mCitrine or EGFR-QG-mCitrine were stimulated with EGF and the resulting lysates were used in western blot analysis. Blots were probed for anti-EGFR, anti-PY72 and anti-tubulin. **B.** Relative phosphorylation level (pY/EGFR) of EGFR-mCitrine and EGFR-QG-mCitrine upon EGF stimulation. Error bars: SEM. EGF stimulation: 100 ng/ml.

We found that EGFR-QG-mCitrine displayed high anisotropy independent of its expression level in the absence of ligand, which was decreased upon EGF stimulation (**Fig.33A,B**). To measure EGFR phosphorylation within the same experiment, we co-expressed PTB-mCherry. This allowed analyzing the co-localization between EGFR and PTB by measuring the fluorescence intensities of EGFR-QG-mCitrine and PTB-mCherry in the cell periphery before and after EGF stimulation. The recruitment factor R was calculated by the following equation:

$$R = \frac{F\ of\ EGFR^{pre} * F\ of\ PTB^{post}}{F\ of\ EGFR^{post} * F\ of\ PTB^{pre}}$$

An increase in phosphorylation was observable at low EGFR-mCitrine expression levels indicated by an increase in co-localization, whereas EGFR was already phosphorylated at high expression levels in the absence of ligand (**Fig.33C**). While PTP inhibition by PV produced similar or even higher EGFR phosphorylation as compared to EGF stimulation (**Fig.31A,C**), EGFR-QG-mCitrine remained in a monomeric state following PV treatment exhibiting high anisotropy (**Fig.33D,E**), demonstrating that autonomously activated EGFR is distinct from ligand-activated, self-associated EGFR.

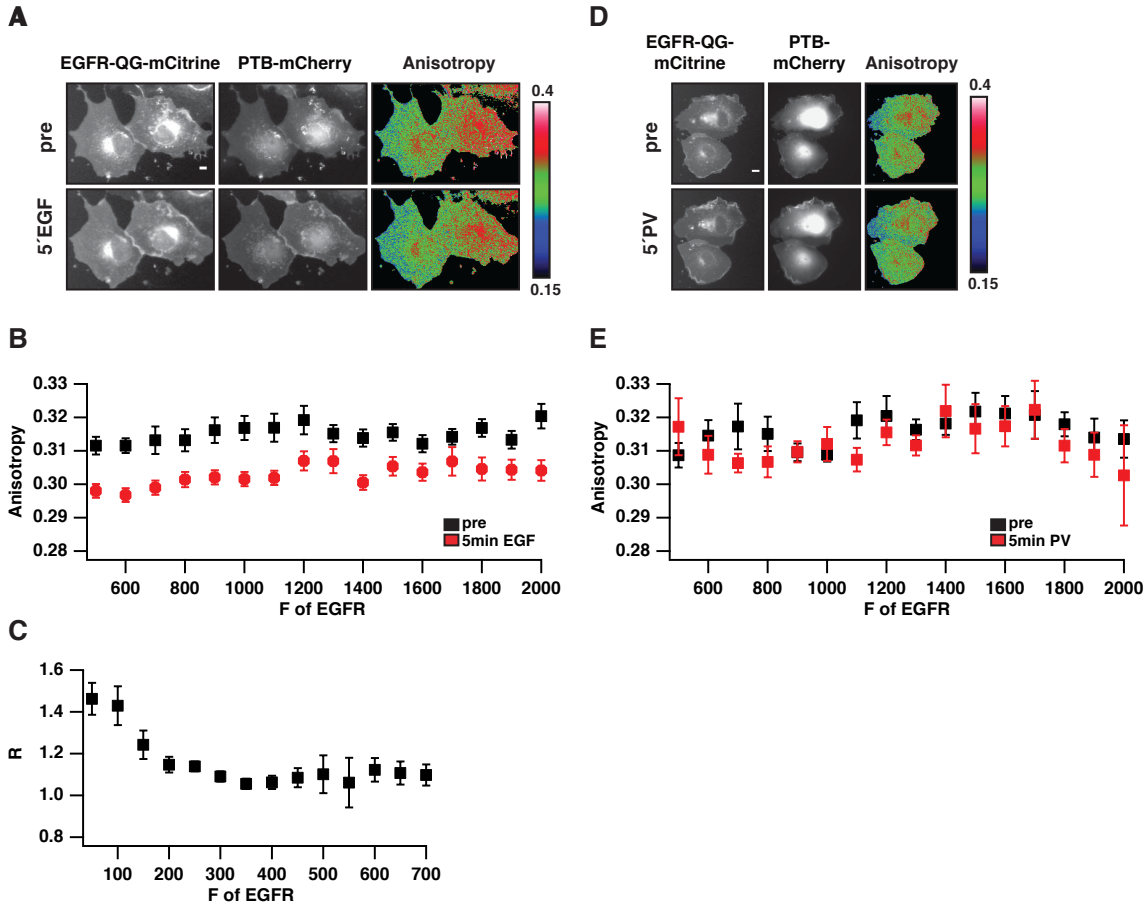

Figure 33: Dependency of EGFR-QG-mCitrine anisotropy on EGFR expression levels. **A.** Representative fluorescence images of Cos7 cells ectopically expressing EGFR-QG-mCitrine and PTB-mCherry and corresponding mCitrine anisotropy upon EGF stimulation. **B.** Anisotropy of EGFR-QG-mCitrine versus binned mean fluorescence intensity (F of EGFR) before and after 5 min EGF stimulation. **C.** Recruitment (R) of PTB-mCherry to EGFR versus binned mean fluorescence intensity (F of EGFR). **D.** Representative fluorescence images of Cos7 cells ectopically expressing EGFR-QG-mCitrine and PTB-mCherry and corresponding mCitrine anisotropy upon PV stimulation. **E.** Anisotropy of EGFR-QG-mCitrine versus binned mean fluorescence intensity (F of EGFR) before and after PV treatment. Scale bars: 10 µm. Error bars: SEM. EGF stimulation: 100 ng/ml. PV treatment: 0.33 mM. (Experiments performed by Dr. Georgia Xouri and analyzed by Martin Baumdick).

4.2.3. Continuous vesicular recycling of monomeric EGFR between the PM and the pericentriolar RE

To examine whether spontaneously phosphorylated, monomeric EGFR is continuously recycled to control autonomous phosphorylation and maintain a constant EGFR concentration at the PM, we investigated whether EGFR partitions in the Rab11-positive pericentriolar RE. Immunofluorescence staining revealed co-localization between endogenous EGFR and Rab11, which was enhanced upon ectopic expression of EGFR-mCitrine and BFP-Rab11a (**Fig.34A,B**). As Rab11a is involved in the biogenesis of the pericentriolar RE[83], ectopic expression of Rab11a-BFP increases this compartment and shifts the distribution of EGFR from the PM to the RE.

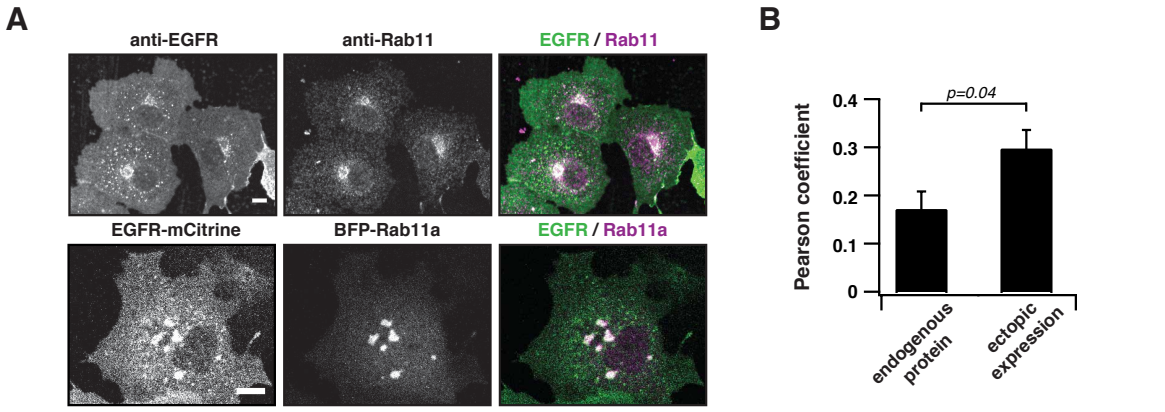

Figure 34: Co-localization of EGFR with Rab11. A. Upper panel: Immunofluorescence staining of endogenous EGFR and Rab11 in Cos7 cells and corresponding green/magenta overlay. Lower panel: Fluorescence images of Cos7 cells ectopically expressing EGFR-mCitrine and BFP-Rab11a and corresponding green/magenta overlay. Scale bars: 10 µm. **B.** Quantification of co-localization between EGFR and Rab11 (endogenous: n=15 cells; ectopic expression: n=12) using Pearson's correlation coefficient. Error bars: SEM.

Fluorescence Loss after Photoactivation (FLAP) and Fluorescence Recovery after Photobleaching (FRAP) were performed to examine the extent of continuous EGFR recycling between the RE and the PM (**Fig.35**). EGFR-mCherry was co-expressed in FLAP experiments to identify the pericentriolar RE and used for normalization in the analysis. The fluorescence loss of EGFR-paGFP at the RE (τ=273±15 s) and the coincident increase at the PM (τ=167±33 s) upon EGFR photoactivation at the RE indicated that EGFR is recycled from the RE to the PM (**Fig.35A**). The difference in τ stems from the difference in surface area of the RE and the PM that determines the rate of PM-association and the RE-dissociation. By fitting the FLAP data to a two-compartment model we estimated the residence of EGFR at the RE to be ~7.4min (k_{off}=2.22 10^{-3} s^{-1}). From the fluorescence recovery after photobleaching EGFR-mCitrine at the RE we concluded that EGFR also traffics to the RE (**Fig.35B**). Both, FLAP and FRAP data showed that EGFR continuously recycles to and from the pericentriolar RE. Our collaborators at the LMB in Cambridge found that EGFR that enters the RE at steady state originates from the PM[123] confirming that the EGFR distribution between PM and RE is maintained through continuous recycling, with the majority of EGFR being at the PM. EGF stimulation resulted in a switch of vesicular EGFR trafficking to LAMP1-positive lysosomes, where the receptor is degraded[123].

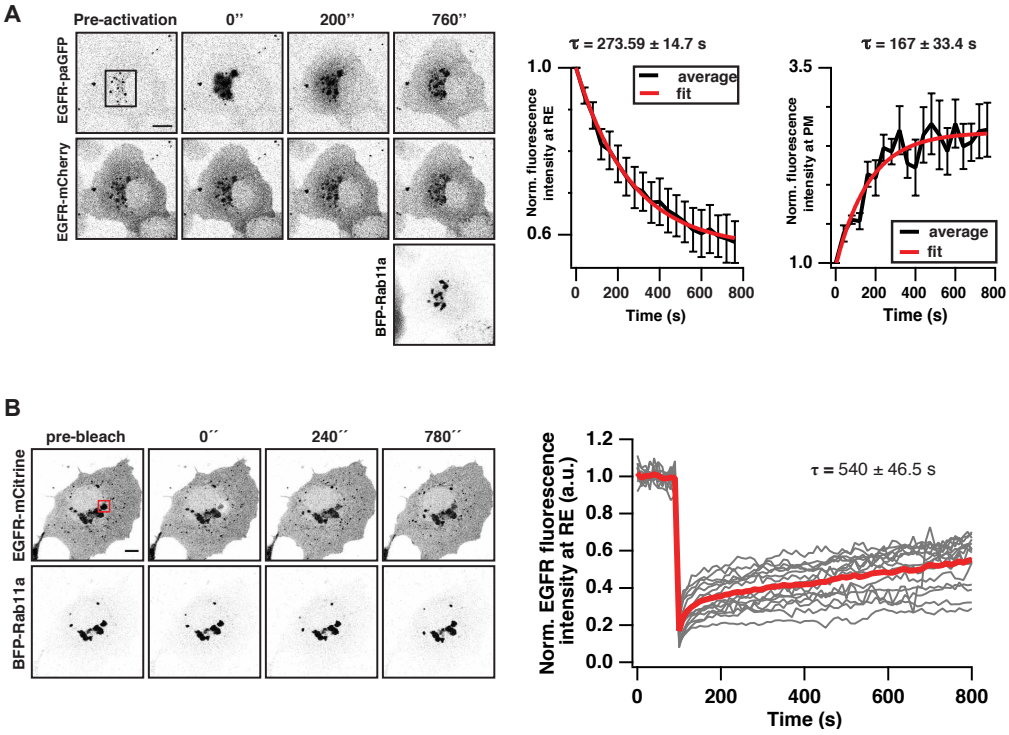

Figure 35: Continuous recycling of EGFR to and from the pericentriolar RE. A. Fluorescence redistribution of EGFR-paGFP upon photoactivation on the recycling endosome. Fluorescence images of EGFR-paGFP (photoactivation in the rectangle of the pre-activation image), EGFR-mCherry and BFP-Rab11 (left). Loss of EGFR-paGFP fluorescence on the RE normalized to the EGFR-mCherry fluorescence intensity. Mean values were fitted to an exponential function to calculate time constants (τ) (middle). Gain of EGFR-paGFP fluorescence at the PM normalized to EGFR-mCherry fluorescence intensity. Mean values were fitted to an exponential function to calculate time constants (τ) (right). n=6 cells. **B.** Fluorescence recovery of EGFR-mCitrine on the RE after photobleaching. Fluorescence images of EGFR-mCitrine and BFP-Rab11a. Red rectangular shows the area of photobleaching (left). Normalized mean fluorescence intensity of bleached area plotted as function of time (right; red line: average curve; grey lines: individual cells). n=10 cells. Scale bars: 10 µm. Error bars: SEM. (Experiments performed by Dr. Georgia Xouri and analyzed by Martin Baumdick).

4.2.4. Vesicular trafficking of EGFR through early endosomes

To examine where the switch from continuous recycling into directed trafficking to lysosomes occurs, we investigated the co-localization of EGFR and Rab5, a marker protein for early endosomes (EE). Immunofluorescence stainings of Cos7 cells showed co-localization of endogenous EGFR with Rab5, which was increased upon EGF stimulation, but only marginally upon PTP inhibition by PV (**Fig.36A,B**). Similar results were obtained upon ectopic expression of EGFR-mCitrine and Rab5-mCherry (**Fig.36C,D,E**). This confirmed that ligand-activated receptors transit the EEs, but also suggests that autonomously activated, monomeric EGFR traffics through EEs.

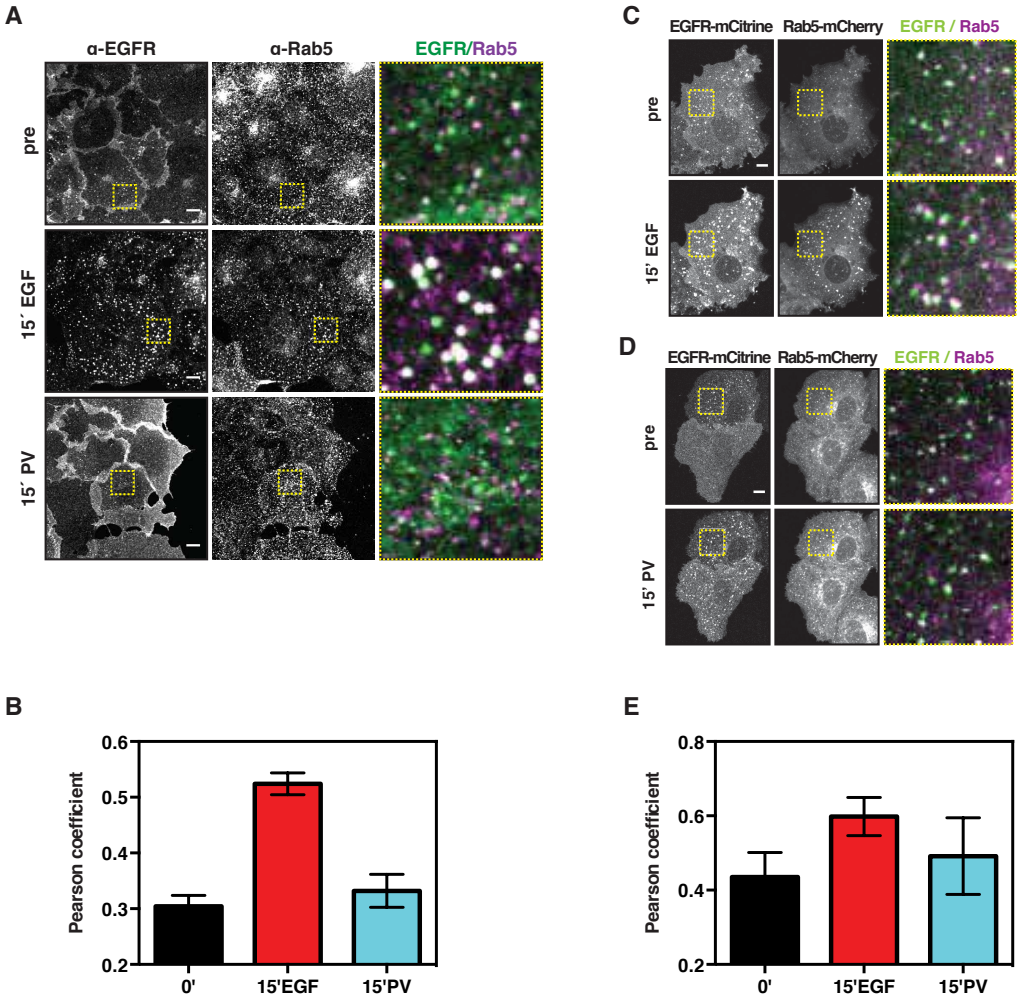

Figure 36: Co-localization of EGFR with Rab5. A. Immunofluorescence stainings of endogenous EGFR and Rab5 in Cos7 cells and corresponding green/magenta overlay of selected ROIs (dotted yellow rectangular) in steady state, after 15 min stimulation with EGF or PV. (Experiment performed by Ola Sabet and analysed by Martin Baumdick) **B.** Co-localization between EGFR and Rab5 before stimulation, after EGF stimulation and PV treatment using Pearson's correlation coefficient. **C. and D.** Fluorescence images of Cos7 cells expressing EGFR-Citrine, Rab5-mCherry and corresponding green/magenta overlay of selected ROIs (dotted yellow rectangular) in steady state, after 15 min stimulation with EGF (**C**) or PV (**D**). **E.** Co-localization between EGFR-mCitrine and Rab5-mCherry in steady state, after EGF (n=5 cells) and PV treatment (n=7) using Pearson's correlation coefficient. Scale bars: 10 µm. Error bars: SEM. EGF stimulation: 100 ng/ml. PV treatment: 0.33 mM.

To directly address whether monomeric EGFR transits via EEs to the pericentriolar RE, we photo-activated EGFR-paGFP at the basal membrane using TIRF microscopy and monitored its appearance in Rab5-mCherry positive EEs in widefield mode. Co-localization between EGFR-paGFP and Rab5-mCherry was observed 5 min after photoactivation confirming that vesicular recycling of monomeric EGFR from the PM to the pericentriolar RE transits through EEs (**Fig.37A,B**). This showed that the differential vesicular trafficking of autonomously activated, monomeric and ligand-activated, self-associated EGFR occurs after entry in the EEs.

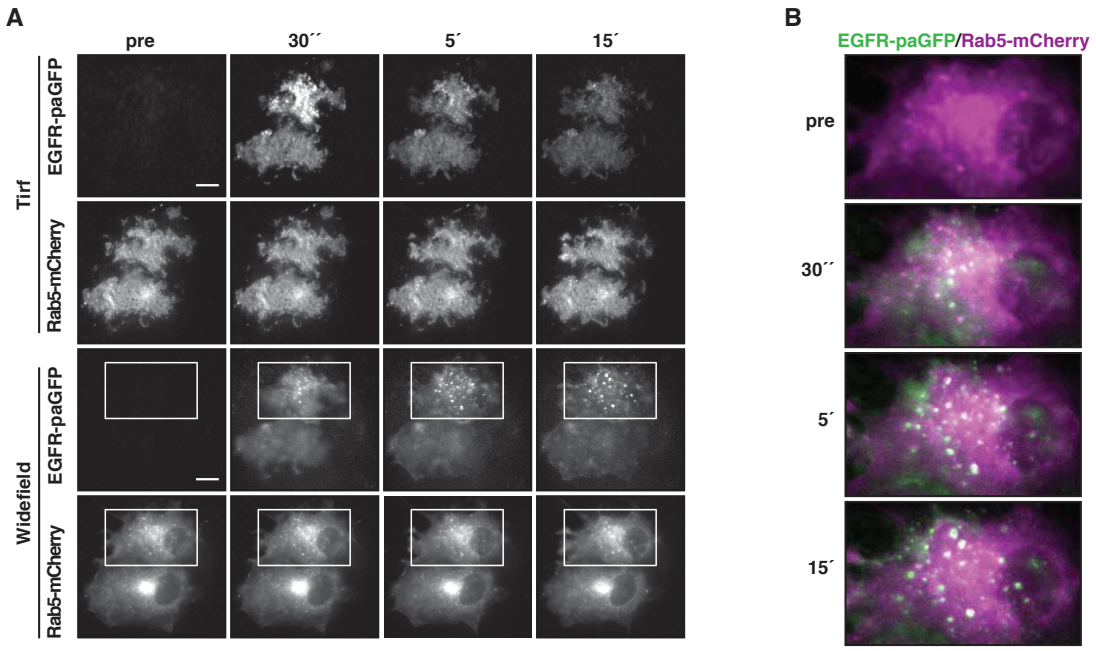

Figure 37: Autonomously activated EGFR traffics through early endosomes. A. Fluorescence redistribution of photoactivated EGFR-paGFP. Representative fluorescence images of Cos7 cells ectopically expressing EGFR-paGFP and Rab5-mCherry. EGFR-paGFP was photoactivated at the basal membrane in TIRF microscopy and its appearance on Rab5-positive endosomes was followed over time in TIRF and widefield microscopy. Scale bars: 10 μm. **B.** Green/magenta overlay of EGFR-paGFP and Rab5-mCherry from the indicated areas (white rectangular) in **A.**

4.2.5. Vesicular recycling suppresses autonomous EGFR activation

To examine whether trafficking of EGFR through the pericentriolar RE contributes to the regulation of EGFR activity, the effect of knockdown and overexpression of Rab11 was investigated. To decrease RE biogenesis, Cos7 cells were treated with two different Rab11 siRNAs. Cells were transfected with EGFR-mCitrine on the next day and immunostained against pY845, pY1045 and pY1068. Phosphorylation of EGFR-mCitrine on Y845 (-3fold) and Y1045 (-1.5fold) were significantly increased after Rab11 knockdown as compared to cells treated with control siRNA, whereas no change in phosphorylation was detected on Y1068 (**Fig.38A,B,C**). We observed the opposite effect, when the RE biogenesis was increased by ectopic BFP-Rab11a expression resulting in lowered phosphorylation on Y845 and Y1045 in Cos7 cells, whereas the phosphorylation level of Y1068 was not altered in the presence of BFP-Rab11a (**Fig.38D**). The spatial phosphorylation profile of Y845 showed that this tyrosine residue is mostly phosphorylated at the PM and its dephosphorylation happens in perinuclear areas (**Fig.38D**). This is consistent with FLIM data of Cos7 cells transfected with EGFR-mCitrine, PTB-mCherry and BFP-Rab11a showing that EGFR phosphorylation as judged by the fraction of interaction (α) between EGFR and PTB is significantly higher at the PM

as compared to the RE (**Fig.38E**). This demonstrated that spontaneous EGFR phosphorylation occurs at the PM and that EGFR is mostly dephosphorylated in perinuclear areas by continuous recycling through the Rab11-positive RE.

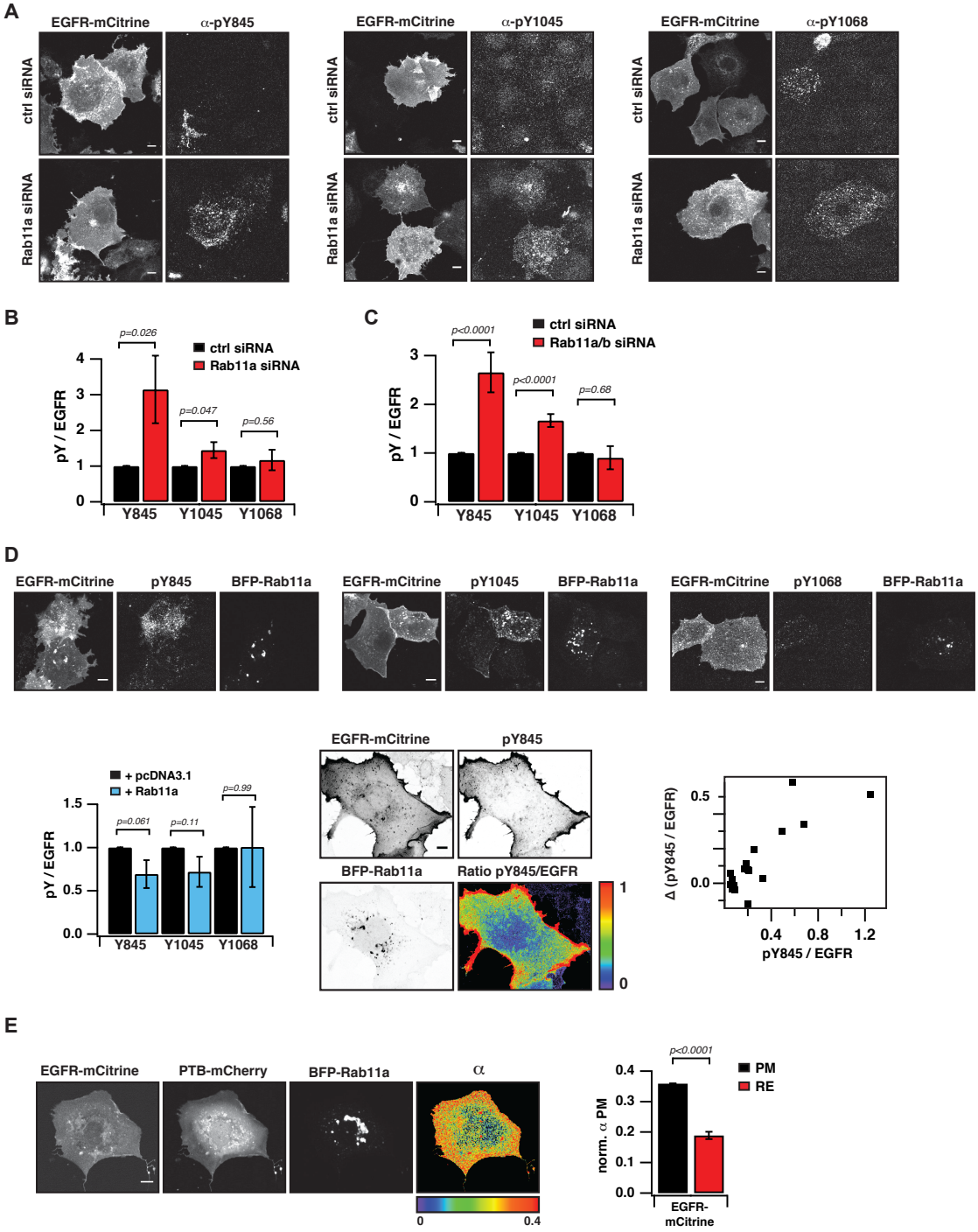

Figure 38: Suppression of autonomously, autocatalytic activated EGFR by vesicular recycling. A. Cos7 cells expressing EGFR-mCitrine were immunostained for pY845, pY1045 and pY1068 after transfection with non-targeting siRNA or Rab11a siRNA. **B. and C.** Relative EGFR phosphorylation (pY/EGFR) on specific tyrosines upon siRNA-mediated Rab11a (**B**) or Rab11a/b (**C**) knockdown normalized to relative EGFR phosphorylation (pY/EGFR) upon transfection with non-targeting siRNA. n=69-83 cells. **D.** Fluorescence images of Cos7 cells ectopically expressing EGFR-mCitrine and BFP-Rab11 were immunostained for pY845, pY1045 and pY1068 (upper panel). Relative EGFR phosphorylation (pY/EGFR) on specific tyrosines upon ectopic BFP-Rab11a expression normalized to relative EGFR phosphorylation

(pY/EGFR) upon transfection with pcDNA3.1 (lower left panel). Fluorescence images of EGFR-mCitrine, pY845 immunostaining and BFP-Rab11a and the ratio of pY845/EGFR show the spatial distribution of spontaneous EGFR phosphorylation on Y845 (lower middle panel). Relative Y845 phosphorylation level (pY/EGFR) against difference in relative Y845 phosphorylation level (pY/EGFR) between PM and RE (lower right panel). For BFP-Rab11a ectopic expression: n=34-52 cells. For pcDNA 3.1 expression: Y845: n=110-138 cells. **E.** Fluorescence images of EGFR-mCitrine, PTB-mCherry and BFP-Rab11a and the corresponding map of the fraction of phosphorylated receptor (α). Fraction of phosphorylated receptor at the PM versus the pericentriolar area (RE). n=12 cells. Scale bars: 10 µm. Error bars: SEM.

We used CONEGI-851 to investigate the conformational state of EGFR in the Rab11a-positive RE. Comparison of the τ of CONEGI-851 between the PM versus the pericentriolar RE showed a slightly higher τ of mCitrine at the RE suggesting that a lower fraction of EGFR samples an active conformation in the pericentriolar RE as compared to the PM (**Fig.39A,B**). The control EGFR-QG-mCitrine revealed no difference in mCitrine τ between RE and PM. This suggested that recycling suppresses EGFR activity by dephosphorylation of Y845 to prevent the stabilization of an active conformation.

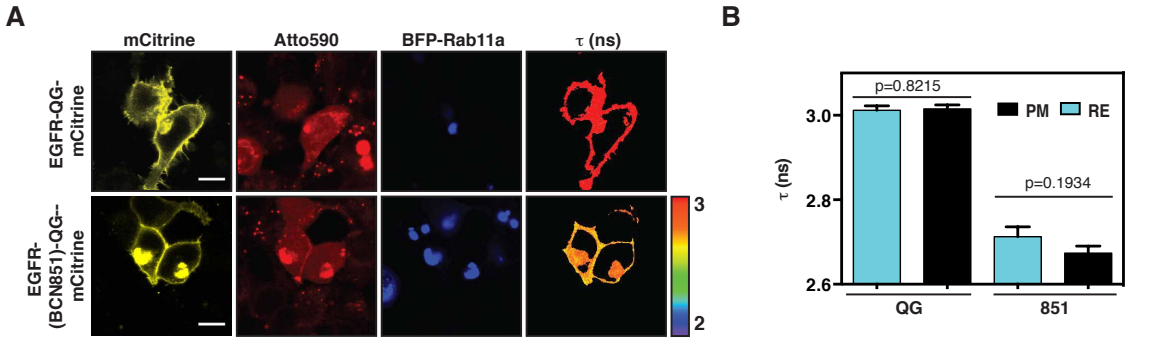

Figure 39: Suppression of spontaneous, autocatalytic EGFR activation at the recycling endosome. A. Fluorescence images of HEK293T cells expressing either EGFR-QG-mCitrine or CONEGI-851 and BFP-Rab11 and corresponding τ. **B.** Mean τ of EGFR-QG-mCitrine (n=3 cells) and CONEGI-851 (n=11) at the PM and RE. Scale bars: 10 µm. Error bars: SEM.

4.2.6. PTP1B dephosphorylates spontaneously activated EGFR in the perinuclear area

Internalized, EGF-activated EGFR is dephosphorylated by the endoplasmatic reticulum associated PTP1B in perinuclear areas[67]. To investigate whether spontaneously activated EGFR is also dephosphorylated by PTP1B in perinuclear areas, we co-expressed EGFR-mCitrine and BFP-PTP1B in Cos7 cells. Immunostaining against pY845, pY1045 and pY1068 showed that phosphorylation on all three tyrosine residues was significantly lowered in the presence of PTP1B (**Fig.40A,B**). To assess where the dephosphorylation of EGFR by PTP1B takes places, we examined the interaction between EGFR-mCitrine and a PTP1B trapping mutant tagged with mCherry (PTP1B-D181A-mCherry). This PTP1B mutant is catalytically inactive, but remains its ability to bind substrate. The interacting

fraction (α) between EGFR and PTP1B-D181A was mostly detected in perinuclear areas, where the RE is located (**Fig.40C**). The mean spatial coincidence of 63 ± 29% between interacting EGFR-PTP1-D181A complexes and BFP-Rab11a supports the idea that EGFR is dephosphorylated on pericentriolar membranes in vicinity of the RE. Co-expression of BFP-Rab11 also increased the interaction between EGFR-mCitrine and PTP1B-D181-mCherry, because of an increased partitioning of EGFR to the RE due to an enlargement of the compartment (**Fig.40C**). This showed that the partitioning of EGFR between PM and pericentriolar RE is an important parameter for the dephosphorylation efficiency of spontaneously activated EGFR.

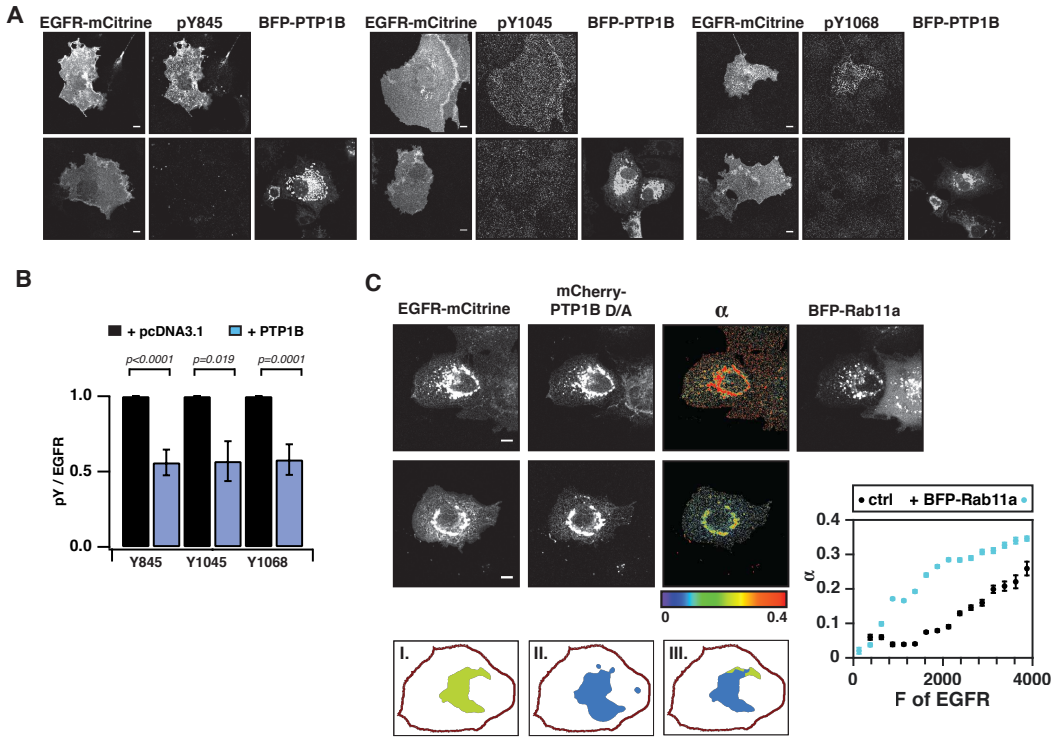

Figure 40: PTP1B dephosphorylates spontaneously activated EGFR in pericentriolar areas. A. Representative fluorescence microscopy images of Cos7 cells ectopically expressing EGFR-mCitrine that were immunostained with specific antibodies for pY845 (left), pY1045 (middle) and pY1068 (right) in presence of BFP-PTP1B or pcDNA3.1. **B.** Relative EGFR phosphorylation (pY/EGFR) on the specific tyrosines upon ectopic BFP-PTP1B expression normalized to relative EGFR phosphorylation (pY/EGFR) upon transfection with pcDNA3.1. n=51-69 cells. **C.** Fluorescence images of Cos7 cells co-expressing EGFR-mCitrine, a trapping mutant (DA) of PTP-1B-mCherry, corresponding α maps showing the fraction of EGFR-mCitrine interacting with the PTP1B trapping mutant in presence or absence of BFP-Rab11a expression. Average α in regions of high EGFR-mCitrine intensity as a function of mean fluorescence (F of EGFR) with (n=28 cells) or without ectopic BFP-Rab11a expression (n=20) (right). Percentage of EGFR/PTP1B D/A interactions in vicinity of the RE was retrieved from overlap (III) between regions with high α (I) and high BFP-Rab11a intensities (II) (lower panel). Scale bars: 10 µm. Error bars: SEM. (Data analysis in **C** was performed by Angel Stanoev).

4.2.7. EGF-dependent, ubiquitination-mediated switch in vesicular trafficking

We have shown that continuous recycling suppresses spontaneous EGFR phosphorylation, but also maintains a steady state partitioning of EGFR between PM and pericentriolar RE. In contrast, it is known that EGF stimulation leads to massive EGFR internalization. We therefore asked what factors are involved in the altered EGFR trafficking upon EGF stimulation. Especially, the role of the E3 ligase c-Cbl, which mediates receptor ubiquitination, was investigated. Cos7 cells ectopically expressing EGFR-mCitrine, c-Cbl-mCherry and BFP-Rab11a were stimulated with labeled EGF-Alexa647 leading to a transient EGFR translocation to the PM, delayed receptor internalization concurrent with c-Cbl recruitment to EGF-EGFR complexes and subsequent receptor depletion from the PM (**Fig.41A**). Differential images of EGFR-mCitrine clearly showed the translocation of EGFR to the PM within one minute and the delayed EGFR internalization, which is concomitant with receptor depletion from the PM (**Fig.41B**). EGF-EGFR complexes did not co-localize with the pericentriolar RE, indicating that ligand-bound EGFR does not recycle through the pericentriolar RE (**Fig.41A**). We repeated the experiment without ectopic expression of c-Cbl-mCherry and found that receptor depletion from the PM was less pronounced and that a subpopulation of EGF-EGFR complexes now trafficked to the pericentriolar RE demonstrating the importance of the stoichiometry between EGFR and c-Cbl to efficiently ubiquitinate the receptor (**Fig.41C,D**). At later time points, we observed a loss of EGFR from the RE, which was enhanced in Cos7 cells upon ectopic expression of c-Cbl-mCherry (**Fig.41A,C,E**). In addition, the pericentriolar RE itself shrank upon EGF stimulation due to redirection of EGFR vesicular trafficking (**Fig.41F**), thereby also redirecting vesicular membrane flux. These findings indicated the importance of the E3-ligase c-Cbl and ubiquitination in the switch of vesicular trafficking.

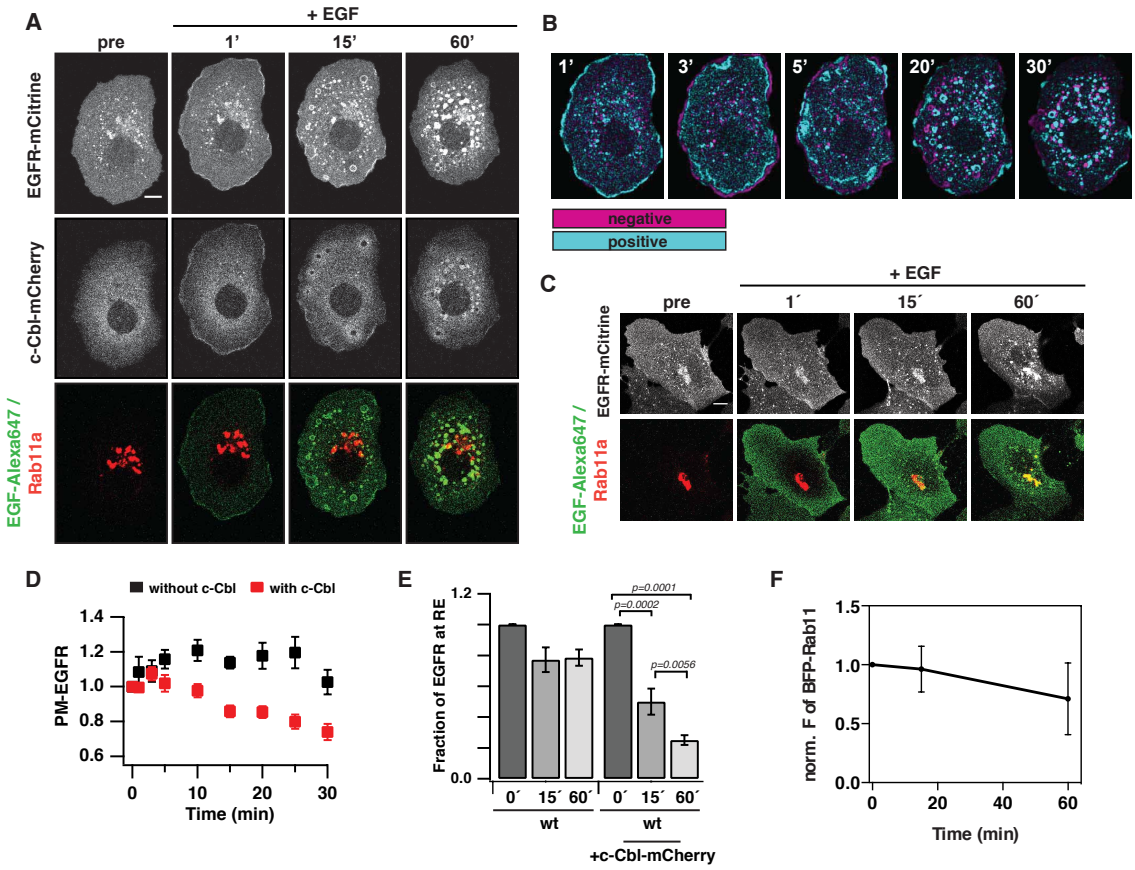

Figure 41: EGF-dependent switch in vesicular EGFR trafficking. A. Fluorescence images of Cos7 cells expressing EGFR-mCitrine, c-Cbl-mCherry and overlay of EGF-Alexa647 (green) and BFP-Rab11a (red) upon stimulation with 5 ng/ml Alexa647-labeled EGF. **B.** Differential images of EGFR-mCitrine showing the appearance (cyan) or loss (magenta) of EGFR-mCitrine intensity between the indicated time and the one prior to it upon stimulation with 5 ng/ml Alexa647-labeled EGF. **C.** Fluorescence images of Cos7 cells expressing EGFR-mCitrine and overlay of EGF-Alexa647 (green) and BFP-Rab11a (red) upon stimulation with 5 ng/ml Alexa647-labeled EGF. **D.** Normalized average fraction of EGFR-mCitrine at the PM (PM-EGFR over total EGFR) in presence (red; n=10 cells) or absence (black; n=6) of c-Cbl-mCherry upon stimulation with EGF. **E.** Fraction of EGFR at RE (EGFR at RE over EGFR at all endosomes) in presence (n=10 cells) or absence of c-Cbl-mCherry (n=6) upon EGF stimulation. **F**. Normalized BFP-Rab11a intensity upon EGF stimulation (n=10 cells). Scale bars: 10 μm. Error bars: SEM.

Besides the pericentriolar recycling, internalized EGFR can also be recycled via the Rab4-positive RE. To assess if and how the fast recycling contributes to the regulation of EGFR activity we co-expressed EGFR-mCitrine and BFP-Rab4 in Cos7 cells and stimulated with labeled EGF-Alexa647. Co-localization between EGFR-mCitrine and BFP-Rab4 increased upon EGF stimulation (**Fig.42A,B**). In contrast to pericentriolar recycling, EGF-EGFR complexes traffic through the fast recycling route (**Fig.42A**) suggesting a role in signal prolongation rather than signal attenuation.

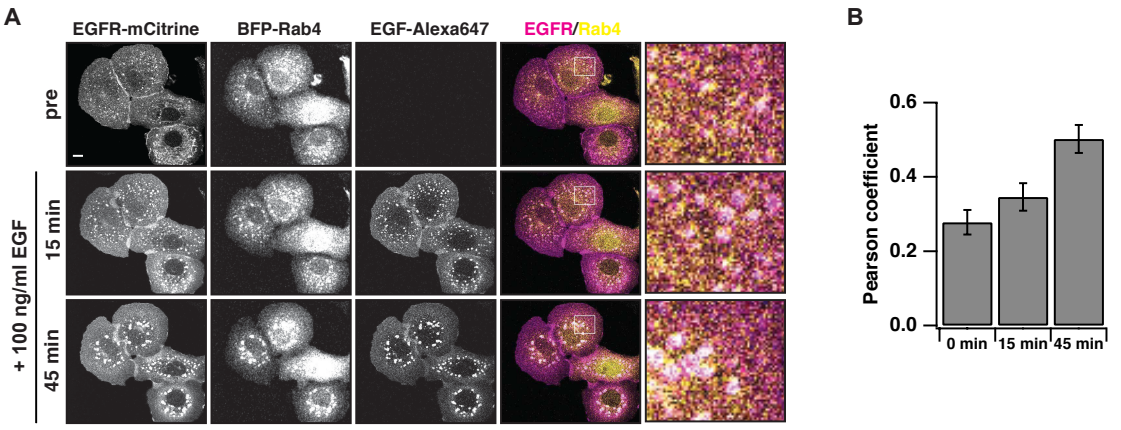

Figure 42: Co-localization of EGFR and Rab4. A. Fluorescence images of Cos7 cells co-expressing EGFR-mCitrine and BFP-Rab4 upon stimulation with 5 ng/ml EGF-Alexa647. Magenta/yellow overlay of EGFR and Rab4 and 'Zoom in' of indicated areas (white rectangular). Scale bar: 10 µm. **B.** Co-localization between EGFR and Rab4 upon EGF stimulation using Pearson's correlation coefficient. n=14 cells. Error bars: SEM.

To address when and where PTP1B dephosphorylates EGFR after EGF stimulation we stimulated Cos7 cells co-expressing EGFR-mCitrine, the PTP1B trapping mutant PTP1B-DA-mCherry and BFP-Rab11a with EGF. In the absence of ligand, the co-localization between EGFR and PTP1B was restricted to perinuclear areas in proximity to the pericentriolar RE, whereas upon EGF stimulation the interaction was also obtained on endosomes in the periphery of the cell (**Fig.43A,B**) demonstrating that the ER spans till the PM and that PTP1B activity is not restricted to perinuclear areas. We also observed again that the pericentriolar RE shrank upon EGF stimulation due to the trapping of EGFR by PTP1B-DA-mCherry and the re-routing of EGFR to the degradative pathway (**Fig.43C**).

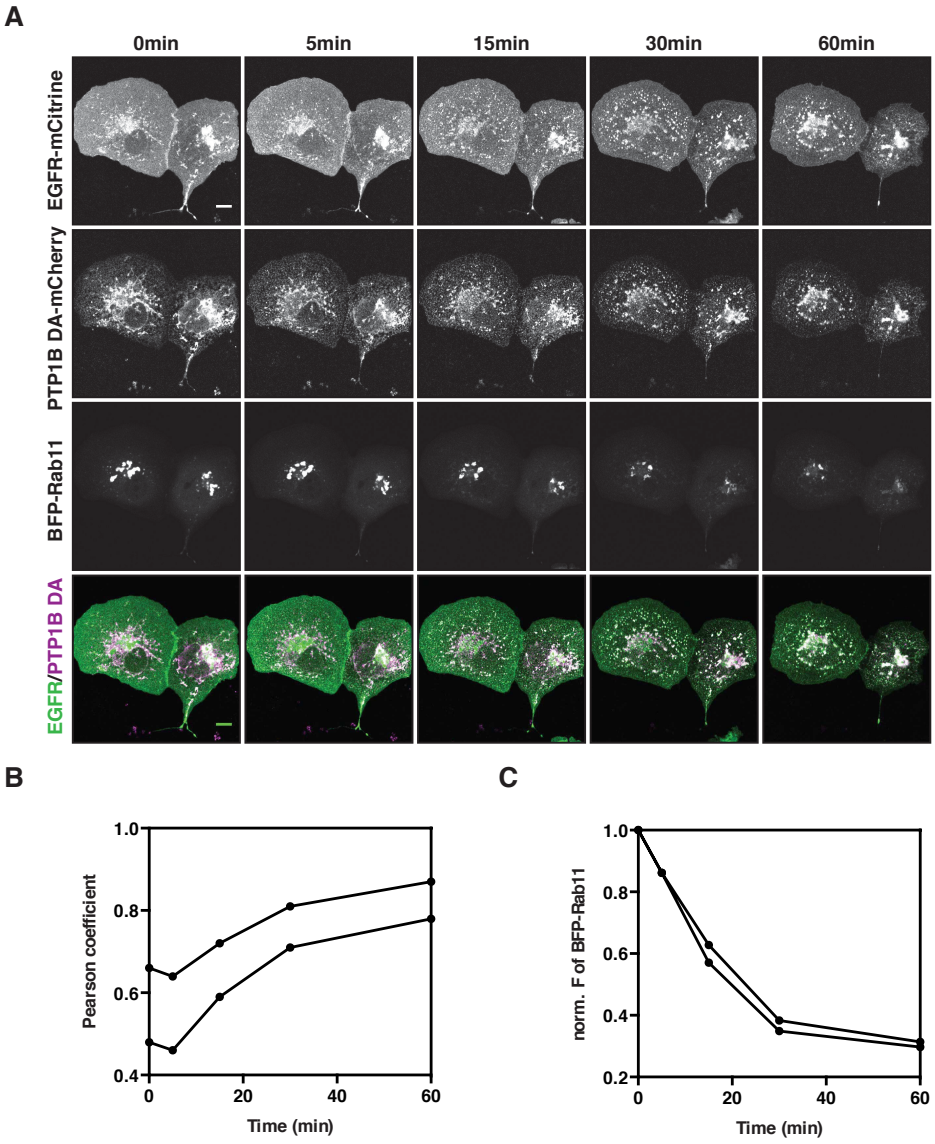

Figure 43: Interaction of EGFR and PTP1B DA trapping mutant. A. Fluorescence images of Cos7 cells co-expressing EGFR-mCitrine, PTP1B-DA-mCherry and BFP-Rab11a and corresponding green/magenta overlay of EGFR and PTP1B-DA upon stimulation with 100 ng/ml EGF. Scale bar: 10 µm. **B.** Co-localization between EGFR-mCitrine and PTP1B DA-mCherry upon EGF stimulation of two cells using Pearson's correlation coefficient. **C.** Normalized BFP-Rab11a intensity upon EGF stimulation of two cells.

To examine the role of ubiquitination in the switch of vesicular trafficking we stimulated Cos7 cells transfected with EGFR-mCitrine, c-Cbl-mCherry and HA-Ubiquitin with EGF or PV. Immunoprecipitation and Western blot analysis showed that EGF stimulation led to ubiquitination (IP) and degradation of EGFR (WB), whereas after PV treatment EGFR was much less ubiquitinated and not degraded (**Fig.44A-C**). Furthermore, in Cos7 cells co-expressing EGFR-mCitrine, c-Cbl-mCherry and BFP-Rab11a EGFR continued to recycle upon PV treatment, whereas a loss of EGFR from the RE was observed upon EGF stimulation (**Fig.44D-F**). This indicated that ubiquitination switches vesicular trafficking from continuous recycling to unidirectional trafficking towards pericentriolar areas.

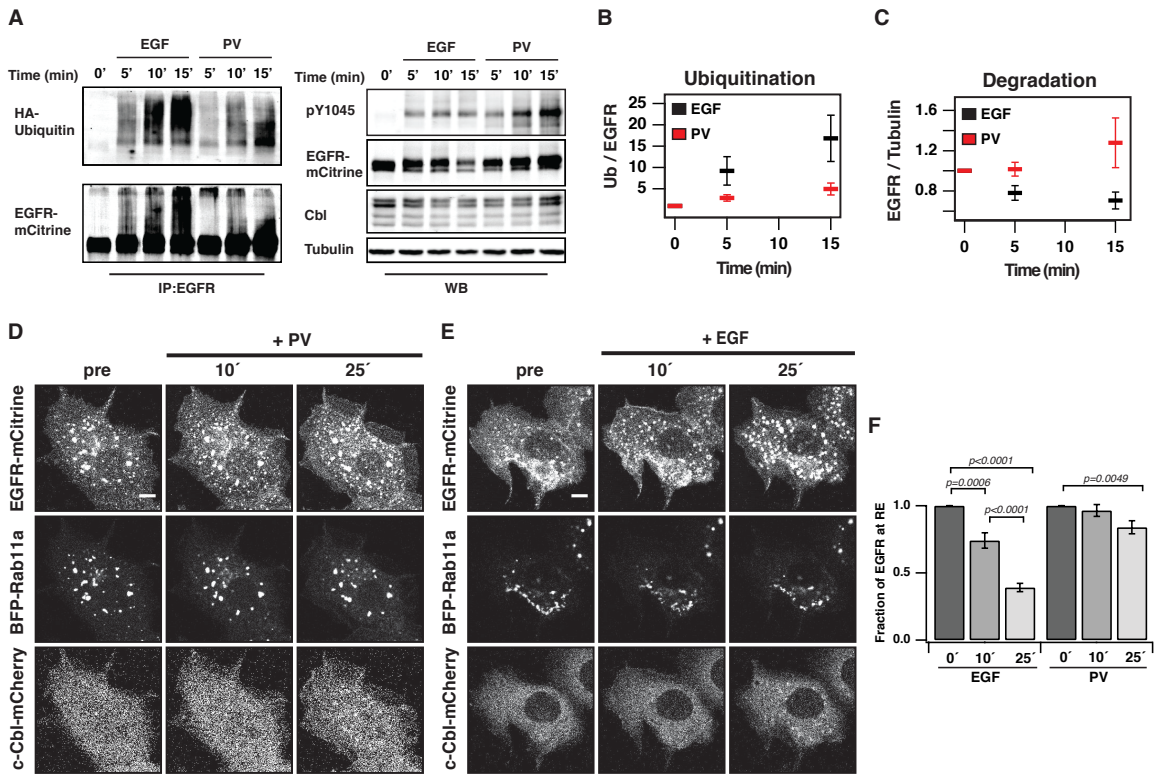

Figure 44: Ubiquitination of EGFR. A. Cos7 cells co-expressing EGFR-mCitrine, c-Cbl-mCherry and HA-ubiquitin were stimulated with EGF or PV and lysates were immunoprecipitated with anti-EGFR (left) or blotted for total proteins (right). IP was probed with anti-HA (HA-ubiquitin) and anti-GFP (EGFR-mCitrine) and total lysates were probed with anti-GFP (EGFR-mCitrine), anti-Cbl (c-Cbl-mCherry), anti-tubulin and anti-pY1045. **B.** Relative EGFR ubiquitination (ubiquitin/EGFR) upon EGF and PV. n=3. **C.** Relative EGFR level (EGFR/tubulin) upon stimulation with EGF or PV. n=3. **D. and E.** Fluorescence images of Cos7 cells expressing EGFR-mCitrine, BFP-Rab11a and c-Cbl-mCherry upon stimulation with PV (**D**) or EGF (**E**). **F.** Fraction of EGFR at RE (EGFR at RE over EGFR at all endosomes) upon EGF (n=12 cells) or PV treatment (n=14). Scale bars: 10 μm. Error bars: SEM. EGF stimulation: 100 ng/ml. PV treatment: 0.33 mM. **(**Experiments were performed and analyzed by Yannick Brüggemann).

Since ubiquitination is mediated by c-Cbl-binding to phosphorylated Y1045, we investigated the importance of this phosphorylation site. Two EGFR mutants, one that is impaired in direct c-Cbl-binding (EGFR-Y1045F) and one that abolished direct and indirect c-Cbl-binding via Grb2 (EGFR-Y1045/1068/1086F) continued to recycle even after EGF stimulation and c-Cbl was not recruited to EGFR (**Fig.45A-C**). Western blot analysis showed that these two ubiquitination-impaired mutants were not degraded, resulting in sustained EGFR phosphorylation (**Fig.45D-F**). However, phosphorylation of Y1045 alone is not sufficient for c-Cbl binding as we observed inefficient ubiquitination of EGFR after PV treatment, although Y1045 was equally or even higher phosphorylated as compared to EGF stimulation (**Fig.45A**). Receptor clustering that only occurred after EGF stimulation, but not upon PV treatment seems to be required for efficient receptor ubiquitination (**Fig.33B**). EGF-induced ubiquitination thus is a secondary signal that re-directs EGFR in pericentriolar areas with high PTP1B activity to terminate signaling and to

commit receptors for degradation in lysosomes thereby preventing recycling and reactivation of ligand-bound receptors at the PM.

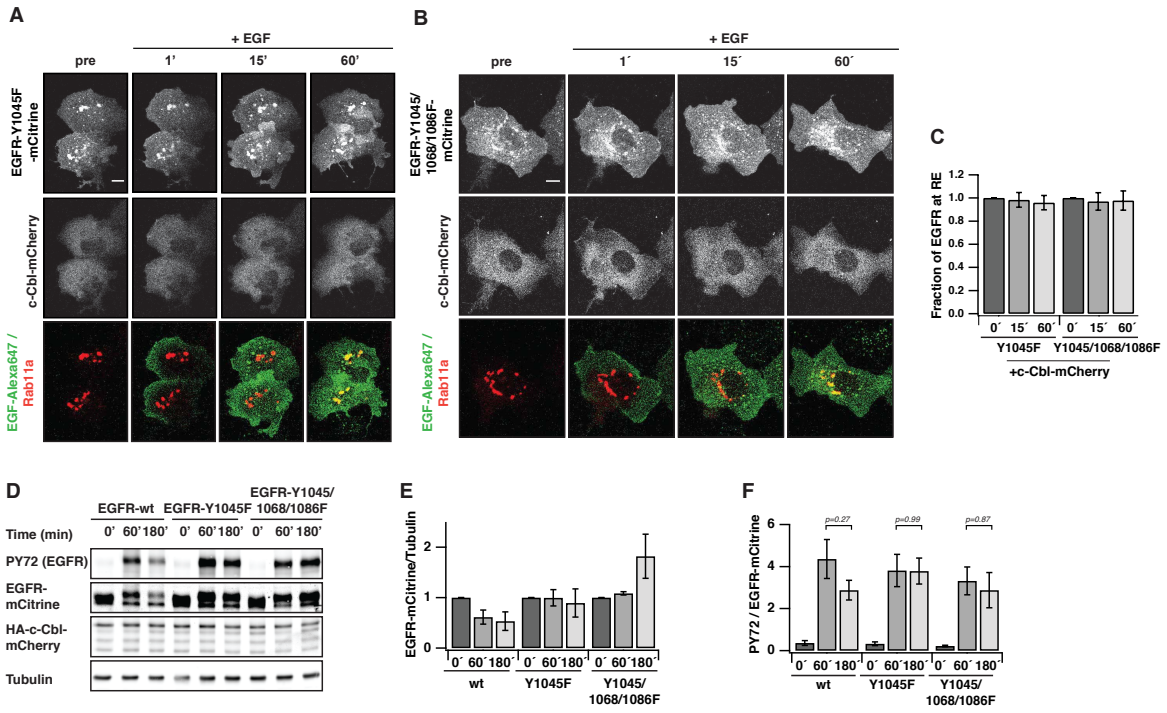

Figure 45: Ubiquitination deficient EGFR mutants continue recycling upon EGF stimulation. A. and B. Fluorescence images of Cos7 cells co-expressing c-Cbl-mCherry and either EGFR-Y1045F-mCitrine (**A**) or EGFR-Y1045/1068/1086F-mCitrine (**B**) and corresponding overlay of EGF-Alexa647 (green) and BFP-Rab11a (green) upon stimulation with Alexa647-labeled EGF (5 ng/ml). **C.** Fraction of EGFR at the RE (EGFR at RE over EGFR at all endosomes) for EGFR-Y1045F-mCitrine (n=9 cells) and EGFR-Y1045/1068/1086F-mCitrine (n=9) upon EGF stimulation (5 ng/ml). **D.** Cos7 cells co-expressing c-Cbl-mCherry and either wild type EGFR-mCitrine, EGFR-Y1045F-mCitrine or EGFR-Y1045/1068/1086F-mCitrine were stimulated with EGF (100 ng/ml) and collected lysates were used in Western blot analysis. Blots were probed with the generic phosphor tyrosine antibody PY72, anti-GFP (EGFR-mCitrine), anti-c-Cbl and anti-tubulin. **E.** Total EGFR (EGFR/Tubulin) for EGFR wt and ubiquitination-impaired EGFR mutants upon EGF stimulation. n=3. **F.** Relative phosphorylation of EGFR (pY/EGFR) for EGFR wt and ubiquitination-impaired EGFR mutants upon EGF stimulation. (n=3). Scale bars: 10 μm. Error bars: SEM. **(**Experiments **D**, **E** and **F** were performed and analyzed by Yannick Brüggemann).

5. Discussion

Autocatalysis a major feature in the EGFR activation mechanism, but can result in spontaneous, uncontrolled EGFR activation in the absence of ligand. We therefore aimed to investigate the molecular mechanism that underlies autocatalytic EGFR activation and how autonomous autocatalytic EGFR activation is suppressed to prevent uncontrolled EGFR phosphorylation.

The catalytic activity of EGFR depends on adopting an active TKD conformation, which is stabilized via allosteric dimer formation upon EGF stimulation. However, evidence has accumulated that the phosphorylation dynamics of EGFR cannot only be explained by this allosteric activation mechanism alone, but emerge from recursive interactions with PTPs and an autocatalytic activation of unliganded EGFR. This study aimed to further understand the EGFR activation mechanism by monitoring the conformational state of key structural elements in the EGFR TKD of liganded and ligandless receptors using a conformational FRET-based EGFR sensor. We identified that autocatalytic EGFR activation relies on EGFR monomers adopting an active conformation, which is stabilized upon Y845 phosphorylation. This autocatalytic amplification can be triggered by ligand-bound allosterically activated EGFR dimers. However, EGFR can also adopt an active conformation due to thermal fluctuations in the absence of ligand resulting in autonomous receptor phosphorylation. Y845 phosphorylated, kinase active EGFR monomers can then further propagate receptor phosphorylation to other monomers, resulting in an autocatalytic EGFR activation that, without mechanisms that constrain such activity, would lead to uncontrolled phosphorylation. Therefore, intrinsic and extrinsic safeguard mechanisms are required to control the activity of EGFR in the absence of ligand. Intrinsic steric auto-inhibitory features have been described in recent years, but these can be overcome by thermal conformational fluctuations. Thus extrinsic mechanisms are also needed that regulate EGFR activity. We identified a suppressive spatial cycle that dephosphorylates autonomously activated EGFR in perinuclear areas with high PTP1B activity, thereby maintaining a low EGFR phosphorylation level at the PM and responsiveness to EGF. EGF stimulation switches the vesicular trafficking from a suppressive cyclical to a unidirectional trafficking route towards lysosomes. This switch is induced by the secondary signal ubiquitin targeting EGFR for degradation. In both cases, the vesicular transport through perinuclear areas with high PTP1B activity suppresses EGFR signaling.

5.1. Design of CONEGI

To date, structural studies have gained insight in the activation mechanism of EGFR by taking snapshots of inactive and active conformations of the ECD and TKD[137,138] thereby representing the most favored conformation in a crystal rather than displaying a set of different possible conformations that EGFR could adopt under physiological conditions in living cells. On the other hand, biochemical data on cell populations provided insight in EGFR kinase activity and its regulation by enzymatic interactions with other proteins. To this end, the design of optical FRET-based sensors can allow us to better understand the spatial and temporal phosphorylation dynamics of EGFR[101,102]. However, due to the lack of an appropriate tool, the activity of the EGFR TKD has not yet been directly related to its conformation. Therefore, we developed multiple variants of the conformational FRET-based EGFR sensor CONEGI that allow us measuring of distinct conformational states of key structural elements in the EGFR TKD in living cells. Conformational changes coupled to EGFR activation are then mirrored by changes in the FRET efficiency due to changes in the distance and/or orientation between donor and acceptor. We generated several CONEGI variants always harboring the donor, mCitrine, in a fixed, rigid position and the acceptor, Atto590, specifically attached to different, flexible sites of the TKD including kinase loop 2, αC-helix and activation loop that change their conformation upon receptor activation. For EGFR labeling in these critical functional regions we used genetic code expansion in combination with bioorthogonal labeling chemistry. Because UAA incorporation theoretically enables fluorophore attachment in any position in a protein of interest without perturbing protein structure and function, this is a major advantage compared to larger sized FPs that are usually used for N- or C-terminal protein fusion[139]. Thus genetic code expansion establishes as a powerful tool for the development of FRET-based conformational kinase sensors. This was underlined by the recent development of a conformational FRET-based FGFR sensor using genetic code expansion and tetra-cysteine motif labeling [106].

However, because genetic code expansion does not exhibit 100% efficiency in incorporation of an UAA in response to an amber codon we positioned BCNK upstream of mCitrine in EGFR, thereby ensuring that mCitrine is only expressed when translation has not been terminated at the amber codon. Thus, every EGFR-mCitrine molecule detected harbors a BCNK molecule that can be labeled with Atto590. A change in the order of mCitrine and BCNK would result in expression of a mixture between full-length

EGFR(BCNK)-mCitrine molecules that can be labeled with Atto590 and truncated proteins containing EGFR-mCitrine alone that cannot be labeled with Atto590, because translation of the engineered protein was terminated at the amber codon. On the one hand this could affect EGFR functionality and on the other it would affect FLIM measurements depending on the efficiency of BCNK incorporation. However, our approach circumvents the latter issue, because its trade-off are non-fluorescent, truncated EGFR molecules, which do not affect FLIM measurements. Whether these truncated receptors affect EGFR-mediated cellular responses depends on the localization of these receptor species and therefore needs to be investigated in the future, e.g. by using labeled EGF in an EGF-binding assay to detect changes in EGF/EGFR ratios at the PM between an EGFR control construct without BCNK incorporation and the different CONEGI variants.

The hybrid design (combination of FP and fluorophore) of our CONEGI variants establishes a new class of FRET-based EGFR sensors that substantially differs from those that read out enzyme activity on a substrate level e.g. FLAME and Picchu[101,102]. Furthermore, previously engineered conformational EGFR sensors measured conformational states either of the ECD labeled outside of the cell or of the intracellular C-terminal tail upon *in vitro* labeling[103,104], but could not obtain conformational transitions of key kinase functional elements whose position defines whether the kinase is in an active or inactive state. The design of these sensors was probably restricted by the availability of membrane-permeable dyes that allow *in vivo* labeling of intracellular domains. The development of delivery systems for membrane-impermeable dyes into cells[140] or of novel membrane-permeable fluorophore species e.g. near-infrared silicon-rhodamine dyes[141] will probably facilitate the development of similar conformational FRET sensors in the future. However, here we proved BCNK-labeling with the membrane-permeable Atto590 to be stable and highly specific in living cells (**Fig.16, 17, 18**), which creates a FRET pair with mCitrine that allows different conformational states of the TKD to be represented by different FRET efficiencies. The experimentally obtained FRET efficiencies thereby were in agreement with the before calculated ones demonstrating the power of this approach (**Table 1, Fig.17, 18**).

5.2. Performance of the different CONEGI variants

Genetic code expansion is a powerful tool for protein labeling, because theoretically it allows incorporation of modifiable unnatural amino acids in any position of a protein. This

exchange from a natural to an UAA is supposed to only minimally perturb protein folding, structure and function. However, especially upon BCNK incorporation in structural key elements that are crucial for catalytic kinase activity, it was important to examine whether the engineered CONEGI variants retain their localization and functionality. BCNK incorporation in the TKD of EGFR did not alter the characteristic PM localization, but perturbed the kinase functionality to varying extents as judged by their different phosphorylation levels upon autonomous and EGF-mediated receptor activation (**Fig.16, 20, 21**). Whereas CONEGI-712/713, CONEGI-713, CONEGI-730 and CONEGI-737 showed slightly increased or comparable autonomous phosphorylation levels with respect to EGFR-QG-mCitrine, the phosphorylation upon EGF stimulation did not increase to the same extent as compared to EGFR-QG-mCitrine suggesting that incorporation of BCNK at these sites interferes with kinase function. For example, incorporation of BCNK in kinase loop 2 (712/713, 713) might perturb the inhibitory electrostatic interaction of kinase loop 2 with the PM[35], whereas BCNK incorporation at site 737 might prevent the formation of a salt bridge between K721 and E738, which is important for the stabilization of an active conformation after activation[10]. BCNK incorporation in the αC-helix (730 and 737) could also prevent correct folding of the α-helix and thus perturb kinase function. In contrast, the fold-changes in phosphorylation of CONEGI-843 and -851 were comparable to that of EGFR-QG-mCitrine. This showed that BCNK incorporation in the activation loop did not interfere with kinase function probably because the activation loop is a highly flexible structure and the incorporation sites are sufficiently apart from the DFG motif and a β-sheet that turns into a two-turn helix upon kinase activation[39]. Further characterization of CONEGI-851 by immunofluorescence showed that CONEGI-851 is fully functional and properly folded at the PM, whereas a subpopulation of CONEGI-851 that is partially unfolded due to protein instability might exist in the cell interior (**Fig.22**). Western blot analysis and fluorescence anisotropy measurements further revealed that its phosphorylation and dimerization was not affected upon labeling with Atto590 demonstrating that BCNK incorporation in conjunction with Atto590 labeling is compatible with EGFR kinase functionality (**Fig.22, 24**).

5.3. Autocatalytic activation of EGFR

The canonical view of EGFR activation implies that ligand binding induces asymmetric dimer formation by an allosteric interaction that stabilizes the active conformation of the

TKD and leads to trans-phosphorylation of regulatory and signaling tyrosines[37,142]. However, the collective EGFR phosphorylation dynamics cannot only be explained by the allosteric activation mechanism, but rather emerges from autocatalytic amplification of EGFR activation and its interplay with PTPs. EGFR autocatalysis was first described more than a decade ago, but its molecular basis remained unclear. New insight was gained when structural and molecular dynamics studies presented evidence that Y845 phosphorylation stabilizes an active conformation and suggested that this posttranslational modification in the EGFR activation loop enhances the dimerization affinity[10]. Deciphering the autocatalytic activation mechanism therefore requires monitoring the TKD conformation of liganded and ligandless EGFR and relating it to EGFR activity and its self-association. For this, we developed the conformational EGFR sensor CONEGI-851 that monitors the activation loop conformation, and thereby aimed to answer, on which EGFR species the autocatalytic EGFR activation relies, if Y845 phosphorylation stabilizes an active conformation and whether Y845 phosphorylation depends on EGFR kinase activity. Monitoring EGFR self-association by fluorescence anisotropy and EGFR conformation by fluorescence lifetime measurements on CONEGI-851 revealed that while the active conformation of EGF-induced EGFR dimers is stabilized by allosteric interactions, Y845 phosphorylation stabilizes the active conformation in EGFR monomers (**Fig.24**). The EGFR concentration-dependent increase in Y1068 phosphorylation further showed that Y845 phosphorylation occurs via trans-phosphorylation (**Fig.26**). This probably happens in EGFR-dense regions of the cell (e.g. clathrin-coated pits), where the chance of randomly colliding receptors is increased resulting in amplified EGFR phosphorylation[143]. The propagation of autocatalytic activation is thereby mediated by EGF-bound allosteric activated EGFR dimers due to Y845 trans-phosphorylation (**Fig.46**). Furthermore, autocatalysis can also enhance spontaneous EGFR activation that originates from thermal fluctuations generating a subpopulation of receptors that adopts an active conformation (**Fig.26**). Once Y845 is phosphorylated, this stabilizes the active conformation in a monomer that then can further trans-phosphorylate Y845 on other EGFR monomers, thereby amplifying EGFR activation. With this, we have uncovered two activating links that induce the autocatalytic activation on EGFR monomers. We further provide evidence that Y845 is an auto-phosphorylation site since the maximum phosphorylation on Y845 was dependent on EGFR kinase activity, however, we cannot exclude that EGFR-activated Src also phosphorylates Y845 (**Fig.25**)[131,144]. However, as long as Y845 phosphorylation depends on EGFR kinase activity this generates a positive feedback resulting in

autocatalytic amplification of ligandless EGFR monomer activation. Preventing the autocatalytic activation of EGFR monomers by replacement of the autocatalytic tyrosine with a phenylalanine (F) creating an Y845F mutant lowered both autonomous as well as the EGF-induced phosphorylation, but did not completely abolish EGFR phosphorylation (**Fig.26, 27, 28**). This together with the PV-induced change in conformation of CONEGI-Y845F suggests that an additional posttranslational modification or allosteric interaction stabilizes the active conformation of EGFR monomers (**Fig.26**).

If autocatalytic EGFR activation would be the only feature in the collective EGFR activation mechanism, this positive feedback would lead to complete phosphorylation of EGFR in time. Therefore, the question arises how the autocatalytic activation mechanism of EGFR is regulated by molecular interactions. Y1086 was shown to be involved in regulation of Y845 phosphorylation[12], and hence could provide an intrinsic layer in controlling autocatalytic activation. On the other hand, we identified a spatial cycle (more detailed description in section 5.7.) that suppresses autonomous Y845 phosphorylation by continuous recycling of internalized EGFR monomers through pericentriolar areas with high PTP activity. This keeps the phosphorylation level of the autocatalytic site in check to prevent uncontrolled receptor activation and maintains responsiveness to growth factors. The PV-induced active conformation of the EGFR TKD provided evidence that Y845 phosphorylation is also controlled by phosphatase activity directly at the PM (**Fig.24**). This could suggest a role of RPTPs, which are located at the PM and known to interact with or dephosphorylate EGFR[60,145]. Furthermore, coupling of EGFR activity to PTP inhibition via ROS production by NOX complexes[59] could generate a double negative feedback. This toggle switch topology in conjunction with the autocatalytic positive feedback provides the basis for the non-linear increase in phosphorylation at a threshold concentration of EGF.

In summary, we manifested a clear role of Y845 phosphorylation in the EGFR activation mechanism whose function was ambiguous for a long time, and is consistent with what is known for other kinases; that activation loop phosphorylation is an important feature to enable full catalytic activity of the TKD[146].

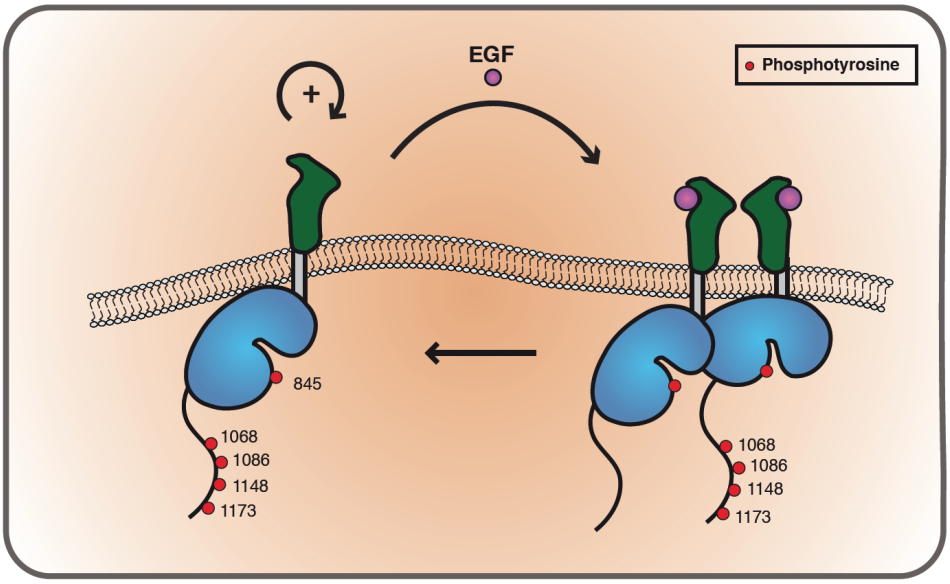

Figure 46: EGF-binding to EGFR induces allosteric receptor dimerization and subsequent trans-phosphorylation of auto-phosphorylation sites at the C-terminal receptor tail. These active EGFR dimers can trans-phosphorylate Y845 on EGFR monomers thereby stabilizing an active monomeric conformation. Propagation of Y845 phosphorylation by these active monomers on further EGFR monomers generates an autocatalytic amplification mechanism that enhances EGFR phosphorylation.

5.4. Autonomous activation of EGFR

Ligand-induced EGFR dimerization enhances the catalytic activity of the TKD resulting in auto-phosphorylation of signaling tyrosines at the C-terminal tail. However, in recent years, evidence has accumulated that EGFR can also be autonomously activated[49]. Since EGFR activity requires its TKD to adopt an active conformation, ligand-independent activation relies on conformational fluctuations in the EGFR TKD between an active and inactive conformation in the absence of ligand. Such a two state equilibrium was previously reported for the fibroblast growth factor receptor (FGFR)[51].

Here, we investigated the magnitude of autonomous, autocatalytic EGFR activation by measuring phosphorylation on the autocatalytic site Y845, the c-Cbl binding site Y1045 and the signaling site Y1068 as well as the EGFR TKD conformation as a function of EGFR expression level. Autonomous phosphorylation at all three tyrosine residues as well as the fraction of CONEGI-851 adopting an active conformation increased with EGFR expression (**Fig.26, 29, 30**). This can be explained by a higher probability of random collision of active monomers at high EGFR densities resulting in autonomous phosphorylation. Once Y845 is phosphorylated this stabilizes the active monomeric conformation that triggers autocatalytic amplification on further EGFR monomers. Autonomous autocatalytic receptor activation resulting in a concentration-dependent increase in phosphorylation has also been observed for the cell guidance RTK EphA2

suggesting that autonomous autocatalytic activation is a general mechanism to amplify RTK activation[105]. Out of the three tyrosines, Y845 was the most responsive site at steady state and a tyrosine to phenylalanine mutation of this site lowered auto-phosphorylation on Y1068 as well as the fraction of receptors adopting an active conformation, thereby demonstrating the autocatalytic function of Y845 (**Fig.26, 29, 30**). Furthermore, the higher phosphorylation of Y845 upon inhibition of phosphatases compared to that upon EGF stimulation demonstrated that this autocatalytic site is tightly controlled by phosphatase activity in the absence of ligand as well as after ligand stimulation to prevent uncontrolled EGFR activation (**Fig.31**). In contrast, the c-Cbl binding site Y1045 was the least responsive site in steady state suggesting a low catalytic efficiency of the kinase for this site to prevent receptor ubiquitination and degradation in the absence of ligand (**Fig.29, 30, 31**).

Since autonomous autocatalytic EGFR activation occurs at the PM predominantly in regions with high receptor densities[130,143] this leads to an increased Akt activation through PIP_3 production by PI3K[123]. On the other hand, Erk activation was not affected by increased autonomous EGFR phosphorylation suggesting that Erk is primarily activated on endosomes or that Erk adapts to sustained EGFR activity due to negative feedback in its network topology[147].

5.5. EGFR recycling suppresses autonomous, autocatalytic activation on EGFR monomers

The concentration-dependent increase in EGFR phosphorylation can trigger the autocatalytic activation mechanism resulting in uncontrolled EGFR activation. To control EGFR activity in the absence of ligand, safeguard mechanisms are required that counteract autonomous EGFR activation. Intrinsic structural features inhibit EGFR activation to a certain extent, but can be overcome by thermal fluctuations that allow EGFR to adopt an active conformation. Therefore, additional extrinsic safeguard mechanisms are required that regulate autonomous, autocatalytic EGFR activation. To better understand the regulation of EGFR activity in the absence of ligand, we addressed whether the endocytic machinery contributes to the regulation of autonomously activated EGFR monomers.

Co-localization between EGFR and Rab11 as well as FLAP and FRAP experiments in conjunction with pulse-labeling of EGFR at the PM showed that autonomously activated monomeric EGFR is continuously recycled between the PM and the pericentriolar RE,

thereby maintaining a constant EGFR concentration at the PM (**Fig.34, 35**). However, whether EGFR monomers take the same endocytic route via EEs as ligand-bound dimeric receptors or if this EGFR species is directly transported to the pericentriolar RE in small vesicles, could not be answered by these experiments. By photoactivating EGFR at the basal membrane in TIRF microscopy and then monitoring its occurrence in Rab5-positive EEs in widefield microscopy, we demonstrated that the decision whether EGFR is targeted for degradation or recycled back to the PM is made after entry in EEs (**Fig.37**). From EEs, autonomously activated EGFR is transported to the pericentriolar RE and then recycled back to the PM. What benefit does a cell have because of this spatial cycle? First, due to the partitioning of EGFR between the PM and the RE the EGFR density at the PM is reduced thereby decreasing the probability of random receptor collision that results in autonomous EGFR phosphorylation. And second, this spatial cycle actively decreases PM EGFR phosphorylation by transporting autonomously autocatalytic activated EGFR to perinuclear areas that exhibit high phosphatase activity e.g. PTP1B and TCPTP[148,149]. Previous work in our lab identified an activity gradient of PTP1B from the PM towards perinuclear areas where it exhibits highest phosphatase activity. This spatial separation of opposing activities allows ligand-induced receptor activation at the PM, but terminates EGFR signaling in the cell interior[67]. We therefore asked, whether continuous vesicular trafficking serves as a mechanism that suppresses autonomous autocatalytic EGFR phosphorylation by recycling EGFR monomers through areas with high phosphatase activity. siRNA-mediated depletion of the pericentriolar RE resulted in increased EGFR phosphorylation at Y845 and Y1045, whereas ectopic expression of BFP-Rab11a led to lower phosphorylation at Y845 and Y1045 demonstrating that EGFR phosphorylation is suppressed upon EGFR recycling (**Fig.38**). The interaction of EGFR and PTP1B was predominantly observed in perinuclear areas and enhanced by ectopic expression of BFP-Rab11a demonstrating that dephosphorylation of EGFR occurs in pericentriolar areas (**Fig.40**). This was further supported by the spatial phosphorylation profile of autonomously activated EGFR that exhibited declining EGFR activity from the PM towards the cell interior (**Fig.38**). By using CONEGI-851 we could also relate the lower EGFR phosphorylation at the RE to a lower fraction of receptors adopting an active conformation compared to the PM, which can be explained by Y845 dephosphorylation in these areas resulting in the destabilization of the active conformation (**Fig.39**). In contrast, an active conformation of the EGFR TKD can be stabilized at the PM by Y845 phosphorylation leading to autonomous EGFR phosphorylation due to the lower PTP

activity at the PM and the EGFR activity-dependent ROS-mediated inhibition of PTP activity.

Our observations demonstrate that continuous recycling serves as a suppressive cycle that transports autonomously activated EGFR in perinuclear areas where receptors can be dephosphorylated by PTP1B. Dephosphorylated EGFR monomers are then transported back to the PM, thereby maintaining a low EGFR phosphorylation level at the PM and responsiveness to new or sustained growth factor stimuli.

5.6. Ubiquitin-mediated switch in vesicular trafficking

EGF-mediated EGFR dimerization and trans-phosphorylation of C-terminal tyrosine residues are followed by receptor endocytosis into Rab5-positive EEs. From there, EGFR is either recycled to the PM or transported via LEs to lysosomes for degradation. The rate between both trafficking modes thereby determines signaling duration in response to growth factors. To determine how the cell distinguishes between autonomous and ligand-activated EGFR and what role c-Cbl-mediated EGFR ubiquitination plays in this process, we monitored ligand-induced EGFR endocytosis compared to that of autonomously activated EGFR monomers. Furthermore, we investigated whether ubiquitination-impaired EGFR mutants exhibited differential vesicular trafficking compared to EGFR-WT.

EGF-EGFR complexes did not co-localize with the Rab11-positive pericentriolar RE demonstrating that EGF-binding causes a switch in vesicular trafficking from the spatial cycle to a unidirectional trafficking mode (**Fig.41**). Since EGFR is still transported from the RE to the PM upon redirection of vesicular trafficking, this results in the loss of EGFR from the RE, thereby reducing the size of the RE due to concomitant redirection of membrane flux (**Fig.41**). Furthermore, the ongoing delivery of EGFR to the PM results in a fast, transient net translocation of EGFR at the PM before delayed ligand-bound EGFR internalization removes EGFR from the PM (**Fig.41**). Endocytosed, ubiquitinated EGFR is then transported via EEs towards LEs/lysosomes in perinuclear areas, where EGFR signaling is terminated by high phosphatase activity and, subsequently, receptors are degraded. This switch in vesicular trafficking was dependent on ectopic expression of c-Cbl-mCherry indicating that the c-Cbl concentration in a cell is an important parameter determining receptor fate (**Fig.41**). In contrast, autonomous, autocatalytically activated monomeric EGFR was not ubiquitinated, although highly phosphorylated at Y1045,

resulting in continuous EGFR recycling (**Fig.44**). This suggests that phosphorylation of Y1045 alone is not sufficient for EGFR, but rather depends on Y1045 phosphorylation in conjunction with receptor dimerization suggesting that c-Cbl preferentially binds to EGFR dimers (**Fig.33, 44**). We thus identified ubiquitination of activated EGFR dimers as a secondary signal that is essential for the re-routing of vesicular trafficking. We therefore asked, whether perturbation of ubiquitination by mutation of the direct c-Cbl binding site Y1045 or both, direct and indirect c-Cbl binding sites Y1045, Y1068 and Y1086, is sufficient to prevent the switch to a unidirectional trafficking mode. Co-localization of EGF-EGFR complexes with Rab11 showed indeed that impaired c-Cbl binding results in continuous recycling, but also confirmed that EGFR ubiquitination is not required for internalization (**Fig.45**)[150]. The continuous recycling of ligand-bound EGFR leads to a sustained EGFR phosphorylation of the ubiquitination-impaired EGFR mutants, as they can be reactivated at the PM (**Fig.45**). This demonstrates that the protective safeguard could also be exploited by oncogenic EGFR variants that lack the c-Cbl-binding site or by cancer cells that express c-Cbl mutants exhibiting decreased binding affinities to EGFR[151–154]. The resulting inefficient ubiquitination of EGFR leads to EGFR recycling and sustained EGFR phosphorylation.

Our findings show that ubiquitination together with EGFR self-association are decisive factors that determine receptor fate. The ubiquitin-mediated switch in vesicular EGFR trafficking from a suppressive cycle to a unidirectional trafficking mode is necessary to terminate EGFR signaling following EGF stimulation.

5.7. Continuous recycling suppresses autonomous EGFR activation and maintains responsiveness to EGF

Autonomous EGFR activation occurs because of thermal fluctuations of EGFR that allow a subpopulation of receptors to adopt an active conformation. Random collision of active monomeric EGFR molecules results in auto-phosphorylation events that can stabilize the active conformation of further EGFR molecules by Y845 phosphorylation. This generates an autocatalytic feedback that would create uncontrolled EGFR activation in the absence of ligand. Therefore, autonomously activated EGFR is internalized before autocatalytic EGFR activation can propagate across the whole PM. Trafficking of autonomous, autocatalytically activated EGFR via the pericentriolar RE through areas with high PTP1B activity dephosphorylates the autocatalytic site Y845 (**Fig.47**). Thus dephosphorylated

inactive EGFR returns to the PM and the system is reset. Furthermore, continuous recycling lowers the EGFR concentration at the PM by partitioning the receptor between the PM and the pericentriolar RE, thereby decreasing the chance of autonomous activation caused by random colliding receptors. Why is the counteracting activity of PTP1B spatially separated from EGFR activation requiring vesicular trafficking to maintain low EGFR phosphorylation? The answer to this question lies in the two orders of magnitude higher catalytic activity of PTP1B as compared to EGFR[65,148,149] that would also suffice to suppress ligand-induced EGFR activation at the PM, thereby preventing any EGFR response to extracellular signals. Thus, we can conclude that continuous vesicular recycling suppresses autonomous autocatalytic activation of EGFR monomers and maintains responsiveness to EGF. Why then does the regulation of ligand-dependent EGFR activation require a ubiquitin-mediated switch in vesicular trafficking? Ligand-bound EGFR would be similar to autonomously activated EGFR monomers dephosphorylated in pericentriolar areas by PTP1B. However, ligand binding would maintain the active conformation in EGFR molecules promoting re-activation at the PM resulting in sustained EGFR activity. Therefore, the ubiquitin-mediated switch in vesicular trafficking is required to terminate EGFR signaling (**Fig.47**). EGFR ubiquitination thereby is mediated by c-Cbl that binds to phosphorylated Y1045 in EGFR dimers. Hence, we identified EGFR ubiquitination and self-association as the decisive factors for the switch in vesicular trafficking to a unidirectional directional trafficking mode. The switch from a suppressive cyclic to a unidirectional finite EGFR trafficking mode has also been observed for EphA2 suggesting that continuous recycling to suppress autonomous receptor activation and maintain responsiveness to extracellular cues is a general mechanism in regulation of RTK activity [105].

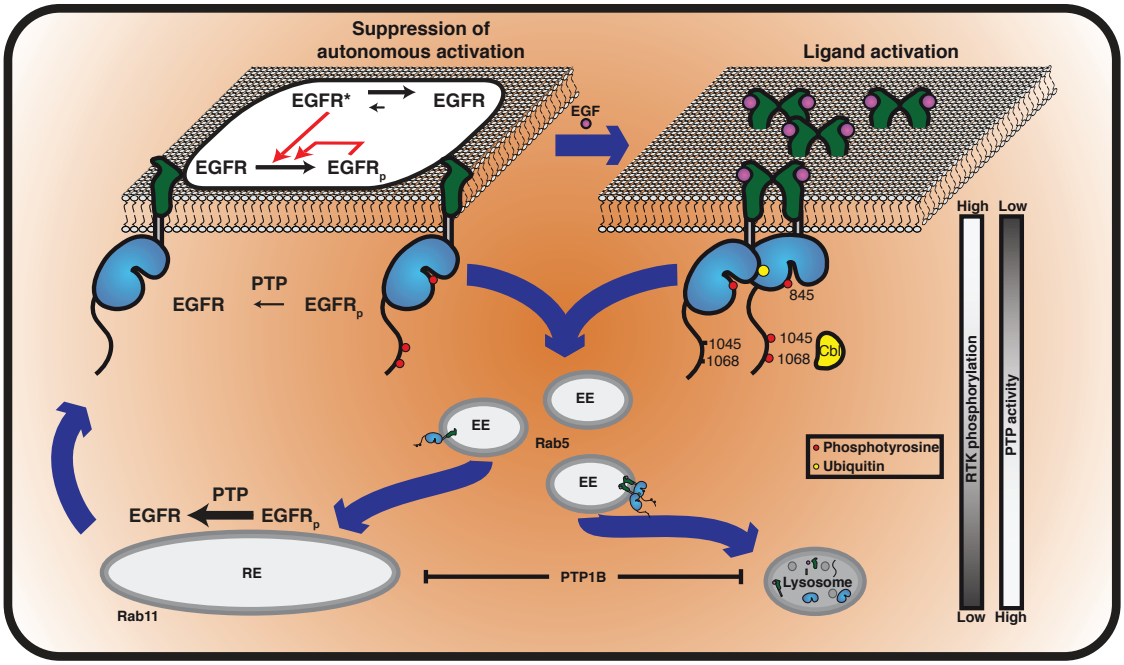

Figure 47: Continuous vesicular recycling acts as a safeguard mechanism that maintains a low level of EGFR activity at the PM by trafficking autonomous, autocatalytically activated EGFR monomers through areas with high PTP activity, where EGFR is dephosphorylated before its return to the PM. In contrast, EGF-induced ubiquitination of EGFR clusters switches the suppressive cycle to a unidirectional trafficking mode. Ubiquitinated EGFR dimers are transported from EEs via LEs to lysosomes, where EGFR signaling is terminated and EGFR is degraded by lysosomal proteases leading to a finite response.

6. Future perspectives

In this study, we gained more insight in the autocatalytic activation mechanism of EGFR by using the conformational EGFR CONEGI. We developed CONEGI to relate the activation loop conformation in the TKD to EGFR activity and self-association and uncovered that EGFR monomers can adopt an active conformation that is stabilized by Y845 phosphorylation, thereby creating the basis for autocatalytic EGFR activation. However, to better understand the amplifying mechanism of EGFR activity, we would need to identify the additional posttranslational modification or allosteric interaction with a protein that also contributes to the stabilization of the active conformation of the EGFR TKD besides Y845 phosphorylation. Furthermore, monitoring individual molecules at low densities instead of averaging over a whole population would allow an investigation into how many conformational states can be adopted in the absence of ligand and how fast the receptor fluctuates between different conformations. For single molecule microscopy, it might be necessary to move away from the hybrid design with one FP and one fluorophore to an approach with two fluorophores, because they exhibit higher brightness and photostability, which would increase the signal to noise ratio. EGFR labeling via SNAP-tag or cysteine motifs as it has been recently described for an FGFR sensor[106] in combination with genetic code expansion and bioorthogonal labeling chemistry could be a possibility for sensor design. However, a more elegant and less perturbing way would be the incorporation of two different UAAs using two orthogonal tRNA synthetase/tRNA pairs. This would require an additional codon such as the quadruplet codon besides the amber codon to encode the second UAA. So far the quadruplet codon was only used for the design of a FRET sensor in bacteria[155], but might be applicable in eukaryotic cells in the near future.

An interesting aspect in the regulation of EGFR activity by vesicular trafficking dynamics would be to investigate, how EGFR vesicular trafficking and EGFR activity are regulated upon stimulation with other EGFR ligands. Both have been individually investigated showing differential endocytic sorting as well as different cellular outcomes upon stimulation with theses ligands[156,157], however, the connection between trafficking dynamics to EGFR signaling outcome has not been drawn yet. Biased agonism inducing different dimer strength could be a major player in differential endocytic sorting[22], since it

would affect the ratio of EGFR dimers targeted to degradation versus EGFR monomers that are recycled and reactivated at the PM, thereby prolonging EGFR signaling.

7. Literature

1. Marshall, C. J. Specificity of Receptor Tyrosine Kinase Signaling : Transient versus Sustained Extracellular Signal-Regulated Kinase Activation. *Cell* **80,** 179–185 (1995).

2. Lemmon, M. A. & Schlessinger, J. Cell signaling by receptor tyrosine kinases. *Cell* **141,** 1117–1134 (2010).

3. Ullrich, A. & Schlessinger, J. Signal transduction by receptors with tyrosine kinase activity. *Cell* **61,** 203–212 (1990).

4. Ward, C. W., Lawrence, M. C., Streltsov, V. a., Adams, T. E. & McKern, N. M. The insulin and EGF receptor structures: new insights into ligand-induced receptor activation. *Trends Biochem. Sci.* **32,** 129–137 (2007).

5. Himanen, J. P. & Nikolov, D. B. Eph signaling: A structural view. *Trends Neurosci.* **26,** 46–51 (2003).

6. Huse, M. & Kuriyan, J. The conformational plasticity of protein kinases. *Cell* **109,** 275–282 (2002).

7. Hubbard, S. R. Juxtamembrane autoinhibition in receptor tyrosine kinases. *Nat. Rev. Mol. Cell Biol.* **5,** 464–471 (2004).

8. Chen, H. *et al.* A Molecular Brake in the Kinase Hinge Region Regulates the Activity of Receptor Tyrosine Kinases. *Mol. Cell* **27,** 717–730 (2007).

9. Bae, J. H. *et al.* The Selectivity of Receptor Tyrosine Kinase Signaling Is Controlled by a Secondary SH2 Domain Binding Site. *Cell* **138,** 514–524 (2009).

10. Shan, Y. *et al.* Oncogenic mutations counteract intrinsic disorder in the EGFR kinase and promote receptor dimerization. *Cell* **149,** 860–870 (2012).

11. Niu, X. L., Peters, K. G. & Kontos, C. D. Deletion of the carboxyl terminus of Tie2 enhances kinase activity, signaling, and function: Evidence for an autoinhibitory mechanism. *J. Biol. Chem.* **277,** 31768–31773 (2002).

12. Kovacs, E. *et al.* Analysis of the role of the C-terminal tail in the regulation of the epidermal growth factor receptor. *Mol. Cell. Biol.* **1162,** MCB.00248–15 (2015).

13. Arteaga, C. L. & Engelman, J. A. ERBB receptors: From oncogene discovery to basic science to mechanism-based cancer therapeutics. *Cancer Cell* **25,** 282–303 (2014).

14. Sharma, S. V. & Settleman, J. ErbBs in lung cancer. *Exp. Cell Res.* **315,** 557–571 (2009).

15. Roskoski, R. The ErbB/HER family of protein-tyrosine kinases and cancer. *Pharmacol. Res.* **79,** 34–74 (2014).

16. Erickson, S. L. *et al.* ErbB3 is required for normal cerebellar and cardiac development: a comparison with ErbB2-and heregulin-deficient mice. *Development* **124,** 4999–5011 (1997).

17. Gassmann, M. *et al.* Aberrant neural and cardiac development in mice lacking the ErbB4 neuregulin receptor. *Nature* **378,** 390–4 (1995).

18. Lee, K. F. *et al.* Requirement for neuregulin receptor erbB2 in neural and cardiac development. *Nature* **378,** 394–398 (1995).

19. Miettinen, P. J. Epithelial immaturity and multiorgan failure in mice lacking epidermal growth factor receptor. *Nature* **376,** 337–341 (1995).

20. Sibilia, M. & Erwin, F. Strain-Dependent Epithelial Defects in Mice Lacking the EGF Receptor. *Science (80-.).* **8477,** (1993).

21. Harris, R. C., Chung, E. & Coffey, R. J. EGF receptor ligands. *Exp. Cell Res.* **284,** 2–13 (2003).

22. Freed, D. M. *et al.* EGFR Ligands Differentially Stabilize Receptor Dimers to Specify Signaling Kinetics. *Cell* **0,** 1–13 (2017).

23. Falls, D. L. Neuregulins: Functions, forms, and signaling strategies. *EGF Recept. Fam. Biol. Mech. Role Cancer* **284,** 15–31 (2003).

24. Riese, D. J. & Stern, D. F. Specificity within the EGF family/ErbB receptor family signaling network. *BioEssays* **20,** 41–48 (1998).

25. Sibilia, M. *et al.* The epidermal growth factor receptor: From development to tumorigenesis. *Differentiation* **75,** 770–787 (2007).

26. Yu, F.-S. X., Yin, J., Xu, K. & Huang, J. Growth factors and corneal epithelial wound healing. *Brain Res. Bull.* **81,** 229–235 (2010).

27. Kornblum, H. I. *et al.* Abnormal astrocyte development and neuronal death in mice lacking the epidermal growth factor receptor. *J. Neurosci. Res.* **53,** 697–717 (1998).

28. Sibilia, M., Steinbach, J. P., Stingl, L., Aguzzi, A. & Wagner, E. F. A strain-independent postnatal neurodegeneration in mice lacking the EGF receptor. *EMBO J.* **17,** 719–731 (1998).

29. Sibilia, M. *et al.* Mice humanised for the EGF receptor display hypomorphic phenotypes in skin, bone and heart. *Development* **130,** 4515–4525 (2003).

30. Wang, K., Yamamoto, H., Chin, J. R., Werb, Z. & Vu, T. H. Epidermal growth factor receptor-deficient mice have delayed primary endochondral ossification because of defective osteoclast recruitment. *J. Biol. Chem.* **279,** 53848–53856 (2004).

31. Iwamoto, R. *et al.* Heparin-binding EGF-like growth factor and ErbB signaling is essential for heart function. *Proc. Natl. Acad. Sci. U. S. A.* **100,** 3221–6 (2003).

32. Miettinen, P. J. *et al.* Impaired lung branching morphogenesis in the absence of functional EGF receptor. *Dev. Biol.* **186,** 224–236 (1997).

33. Mitchell, C. *et al.* Heparin-binding epidermal growth factor-like growth factor links hepatocyte priming with cell cycle progression during liver regeneration. *J. Biol. Chem.* **280,** 2562–2568 (2005).

34. Ferguson, K. M. *et al.* EGF activates its receptor by removing interactions that autoinhibit ectodomain dimerization. *Mol. Cell* **11,** 507–517 (2003).

35. Endres, N. F. *et al.* Conformational coupling across the plasma membrane in activation of the EGF receptor. *Cell* **152,** 543–556 (2013).

36. Arkhipov, A. *et al.* Architecture and membrane interactions of the EGF receptor. *Cell* **152,** 557–569 (2013).

37. Zhang, X., Gureasko, J., Shen, K., Cole, P. A. & Kuriyan, J. An Allosteric Mechanism for Activation of the Kinase Domain of Epidermal Growth Factor Receptor. *Cell* **125,** 1137–1149 (2006).

38. Jura, N., Shan, Y., Cao, X., Shaw, D. E. & Kuriyan, J. Structural analysis of the catalytically inactive kinase domain of the human EGF receptor 3. *Proc. Natl. Acad. Sci. U. S. A.* **106,** 21608–21613 (2009).

39. Shan, Y., Arkhipov, A., Kim, E. T., Pan, A. C. & Shaw, D. E. Transitions to catalytically inactive conformations in EGFR kinase. *Proc. Natl. Acad. Sci. U. S. A.* **110,** 7270–5 (2013).

40. Sutto, L. & Gervasio, F. L. Effects of oncogenic mutations on the conformational free-energy landscape of EGFR kinase. *Proc. Natl. Acad. Sci. U. S. A.* **110,** 10616–21 (2013).

41. Batzer, A. G., Blaikie, P., Nelson, K., Schlessinger, J. & Margolis, B. The phosphotyrosine interaction domain of Shc binds an LXNPXY motif on the epidermal growth factor receptor. *Mol. Cell. Biol.* **15,** 4403–4409 (1995).

42. Yarden, Y. & Sliwkowski, M. X. Untangling the ErbB signalling network. *Nat. Rev. Mol. Cell Biol.* **2,** 127–137 (2001).

43. Di Guglielmo, G. M., Baass, P. C., Ou, W. J., Posner, B. I. & Bergeron, J. J. Compartmentalization of SHC, GRB2 and mSOS, and hyperphosphorylation of Raf-1 by EGF but not insulin in liver parenchyma. *EMBO J.* **13,** 4269–4277 (1994).

44. Wouters, F. S. & Bastiaens, P. I. Fluorescence lifetime imaging of receptor tyrosine kinase activity in cells. *Curr. Biol.* **9,** 1127–1130 (1999).

45. Nagy, P. Quantitative Characterization of the Large-Scale Association of ErbB1 and ErbB2 by Flow Cytometric Homo-FRET Measurements ´. *Biophys. J.* **95,** 2086–2096 (2008).

46. Nagy, P., Claus, J., Jovin, T. M. & Arndt-Jovin, D. J. Distribution of resting and ligand-bound ErbB1 and ErbB2 receptor tyrosine kinases in living cells using number and brightness analysis. *Proc. Natl. Acad. Sci. U. S. A.* **107,** 16524–16529 (2010).

47. Kozer, N. *et al.* Recruitment of the adaptor protein Grb2 to EGFR tetramers. *Biochemistry* **53,** 2594–2604 (2014).

48. Huang, Y. *et al.* Molecular basis for multimerization in the activation of the Epidermal Growth Factor Receptor. *Elife* **5,** 1–27 (2016).

49. Reynolds, A. R., Tischer, C., Verveer, P. J., Rocks, O. & Bastiaens, P. I. H. EGFR activation coupled to inhibition of tyrosine phosphatases causes lateral signal propagation. *Nat. Cell Biol.* **5,** 447–453 (2003).

50. Rowinsky, E. K. The erbB family: targets for therapeutic development against cancer and therapeutic strategies using monoclonal antibodies and tyrosine kinase inhibitors. *Annu. Rev. Med.* **55,** 433–57 (2004).

51. Chen, H. *et al.* Cracking the molecular origin of intrinsic tyrosine kinase activity through analysis of pathogenic gain-of-function mutations. *Cell Rep.* **4,** 376–384 (2013).

52. Tischer, C. & Bastiaens, P. I. H. Lateral phosphorylation propagation: an aspect of feedback signalling? *Nat. Rev. Mol. Cell Biol.* **4,** 971–974 (2003).

53. Koseska, A. & Bastiaens, P. I. Cell signaling as a cognitive process. *EMBO J.* **36,** 568–582 (2017).

54. Grecco, H. E., Schmick, M. & Bastiaens, P. I. H. Signaling from the living plasma membrane. *Cell* **144,** 897–909 (2011).

55. Kholodenko, B. Cell-signalling dynamics in time and space. *Nat. Rev. Mol. Cell Biol.* **7,** 165–176 (2006).

56. Kitano, H. Biological robustness in complex host-pathogen systems. *Prog. Drug Res.* **64,** 239–263 (2007).

57. Stelling, J., Sauer, U., Szallasi, Z., Doyle, F. J. & Doyle, J. Robustness of cellular functions. *Cell* **118,** 675–685 (2004).

58. Suárez Pestana, E. *et al.* The transmembrane protein tyrosine phosphatase RPTPsigma modulates signaling of the epidermal growth factor receptor in A431 cells. *Oncogene* **18,** 4069–79 (1999).

59. Xu, Y., Tan, L.-J., Grachtchouk, V., Voorhees, J. J. & Fisher, G. J. Receptor-type Protein-tyrosine Phosphatase-κ Regulates Epidermal Growth Factor Receptor Function. *J. Biol. Chem.* **280,** 42694 –42700 (2005).

60. Tarcic, G. *et al.* An Unbiased Screen Identifies DEP-1 Tumor Suppressor as a Phosphatase Controlling EGFR Endocytosis. *Curr. Biol.* **19,** 1788–1798 (2009).

61. Keilhack, H. *et al.* Phosphotyrosine 1173 mediates binding of the protein-tyrosine phosphatase SHP-1 to the epidermal growth factor receptor and attenuation of receptor signaling. *J. Biol. Chem.* **273,** 24839–24846 (1998).

62. Agazie, Y. M. & Hayman, M. J. Molecular mechanism for a role of SHP2 in epidermal growth factor receptor signaling. *Mol. Cell. Biol.* **23,** 7875–86 (2003).

63. Lammers, R. *et al.* Differential activities of protein tyrosine phosphatases in intact cells. *J. Biol. Chem.* **268,** 22456–22462 (1993).

64. Tiganis, T., Bennett, A. M., Ravichandran, K. S. & Tonks, N. K. Epidermal growth factor receptor and the adaptor protein p52Shc are specific substrates of T-cell protein tyrosine phosphatase. *Mol. Cell. Biol.* **18,** 1622–1634 (1998).

65. Zhang, Z. Y., Maclean, D., Thiemesefler, A. M., Roeske, R. W. & Dixon, J. E. A Continuous Spectrophotometric and Fluorometric Assay for Protein Tyrosine Phosphatase Using Phosphotyrosine-Containing Peptides. *Anal. Biochem.* **211,** 7–15 (1993).

66. Selner, N. G. *et al.* Diverse Levels of Sequence Selectivity and Catalytic Efficiency of Protein-Tyrosine Phosphatases. *Biochemistry* 397–412 (2014). doi:10.1021/bi401223r

67. Yudushkin, I. A. *et al.* Live-cell imaging of enzyme-substrate interaction reveals spatial regulation of PTP1B. *Science (80-.).* **315,** 115–119 (2007).

68. Finkel, T. Intracellular Redox Regulation by the Family of Small GTPases. *Antioxid. Redox Signal.* **8,** 1857–1863 (2006).

69. Rhee, S. G. H2O2 , a Necessary Evil for Cell Signaling. *Sci. Perspect.* 1882–1884 (2006). doi:10.1126/science.1130481

70. Xu, Y., Shao, Y., Voorhees, J. J. & Fisher, G. J. Oxidative inhibition of receptor-type protein-tyrosine phosphatase kappa by ultraviolet irradiation activates epidermal growth factor receptor in human keratinocytes. **281,** 27389–27397 (2013).

71. Lee, S.-R., Kwon, K.-S., Seung-Ryul, K. & Rhee, S. G. Reversible Inactivation of Protein-tyrosine Phosphatase 1B in A431 Cells Stimulated with Epidermal Growth Factor. *J. Biol. Chem.* **273,** 15366–15372 (1998).

72. Tyson, J. J., Novak, B., Tyson, J. J., Novak, B. & Tyson, J. J. Control of cell growth , division and death : information processing in living cells. (2014). doi:10.1098/rsfs.2013.0070

73. Stenmark, H. Rab GTPases as coordinators of vesicle traffic. *Nat. Rev. Mol. Cell Biol.* **10,** 513–525 (2009).

74. Alexandrov, K., Horiuchi, H., Steele-Mortimer, O., Seabra, M. C. & Zerial, M. Rab escort protein-1 is a multifunctional protein that accompanies newly prenylated rab proteins to their target membranes. *EMBO J.* **13,** 5262–5273 (1994).

75. Ullrich, O. *et al.* Rab GDP dissociation inhibitor as a general regulator for the membrane association of rab proteins. *J. Biol. Chem.* **268,** 18143–18150 (1993).

76. Eathiraj, S., Pan, X., Ritacco, C. & Lambright, D. G. Structural basis of family-wide Rab GTPase recognition by rabenosyn-5. *Nature* **436,** 415–9 (2005).

77. Cherfils, J. & Zeghouf, M. Regulation of small GTPases by GEFs, GAPs, and GDIs. *Physiol. Rev.* **93,** 269–309 (2013).

78. Sigismund, S. *et al.* Clathrin-independent endocytosis of ubiquitinated cargos. *Proc. Natl. Acad. Sci. U. S. A.* **102,** 2760–5 (2005).

79. Zerial, M. & Mcbride, H. Rab proteins as membrane organizers. *Nat. Rev. Mol. Cell Biol.* **2,** (2001).

80. Levkowitz, G. *et al.* c-Cbl/Sli-1 regulates endocytic sorting and ubiquitination of the epidermal growth factor receptor. *Genes Dev.* **12,** 3663–3674 (1998).

81. Sorkin, A. *et al.* Recycling of epidermal growth factor-receptor complexes in A431 cells: Identification of dual pathways. *J. Cell Biol.* **112,** 55–63 (1991).

82. Van der Sluijs, P. *et al.* The small GTP-binding protein rab4 controls an early sorting event on the endocytic pathway. *Cell* **70,** 729–740 (1992).

83. Ullrich, O., Reinsch, S., Urbé, S., Zerial, M. & Parton, R. G. Rab11 regulates recycling through the pericentriolar recycling endosome. *J. Cell Biol.* **135,** 913–924 (1996).

84. Schwartz, S. L., Cao, C., Pylypenko, O., Rak, A. & Wandinger-Ness, A. Rab GTPases at a glance. *J. Cell Sci.* **120,** 3905–3910 (2007).

85. Waterman, H. *et al.* A mutant EGF-receptor defective in ubiquitylation and endocytosis unveils a role for Grb2 in negative signaling. *EMBO J.* **21,** 303–313 (2002).

86. Grøvdal, L. M., Stang, E., Sorkin, A. & Madshus, I. H. Direct interaction of Cbl with pTyr 1045 of the EGF receptor (EGFR) is required to sort the EGFR to lysosomes for degradation. *Exp. Cell Res.* **300,** 388–395 (2004).

87. X. Jiang, F. Huang, A. Marusyk, A. S. Grb2 regulates internalization of EGF recptors through clathrin-coated pits. *Mol. Biol. Cell* **14,** 858–870 (2003).

88. Sigismund, S. *et al.* Threshold-controlled ubiquitination of the EGFR directs receptor fate. *EMBO J.* **32,** 2140–57 (2013).

89. Katzmann, D. J., Babst, M. & Emr, S. D. Ubiquitin-dependent sorting into the multivesicular body pathway requires the function of a conserved endosomal protein sorting complex, ESCRT-I. *Cell* **106,** 145–155 (2001).

90. Gruenberg, J. & Stenmark, H. The biogenesis of multivesicular endosomes. *Nat. Rev. Mol. Cell Biol.* **5,** 317–323 (2004).

91. Storrie, B. & Desjardins, M. The biogenesis of lysosomes: Is it a kiss and run, continuous fusion and fission process? *Bioessays* **18,** 895–903 (1996).

92. Shimomura, O., Johnson, F. H. & Saiga, Y. Extraction, Purification and Properties of Aequorin, a Bioluminescent Protein from the Luminous Hydromedusan,Aequorea. *J. Cell. Comp. Physiol.* **59,** 223–239 (1962).

93. Tinoco, I., Gonzalez, R. L., Jr, I. T. & Jr, R. L. G. Biological mechanisms , one molecule at a time Biological mechanisms , one molecule at a time. *Genes Dev.* **25,** 1205–1231 (2011).

94. Bastiaens, P. Fluorescence lifetime imaging microscopy: spatial resolution of biochemical processes in the cell. *Trends Cell Biol.* **9,** 48–52 (1999).

95. Bolbat, A. & Schultz, C. Recent developments of genetically encoded optical sensors for cell biology. *Biol. Cell* **109,** 1–23 (2017).

96. Shaner, N. C., Steinbach, P. a & Tsien, R. Y. A guide to choosing fluorescent proteins. *Nat. Methods* **2,** 905–909 (2005).

97. Anderson, N. G. *et al.* The Fluorescent Toolbox for Assessing protein location and function. *Science (80-.).* **217,** 217–224 (2006).

98. Adams, S. R. & Tsien, R. Y. Preparation of the membrane-permeant biarsenicals FlAsH-EDT2 and ReAsH-EDT2 for fluorescent labeling of tetracysteine-tagged proteins. *Nat. Protoc.* **3,** 1527–1534 (2008).

99. Davis, L. & Chin, J. W. Designer proteins: applications of genetic code expansion in cell biology. *Nat. Rev. Mol. Cell Biol.* **13,** 168–182 (2012).

100. Nikić, I. & Lemke, E. a. Genetic code expansion enabled site-specific dual-color protein labeling: Superresolution microscopy and beyond. *Curr. Opin. Chem. Biol.* **28,** 164–173 (2015).

101. Kurokawa, K. *et al.* A Pair of Fluorescent Resonance Energy Transfer-based Probes for Tyrosine Phosphorylation of the CrkII Adaptor Protein in Vivo. *J. Biol. Chem.* **276,** 31305–31310 (2001).

102. Offterdinger, M., Georget, V., Girod, A. & Bastiaens, P. I. H. Imaging phosphorylation dynamics of the epidermal growth factor receptor. *J. Biol. Chem.* **279,** 36972–36981 (2004).

103. Ziomkiewicz, I. *et al.* Dynamic conformational transitions of the EGF receptor in living mammalian cells determined by FRET and fluorescence lifetime imaging microscopy. *Cytom. Part A* **83,** 794–805 (2013).

104. Lee, N. & Koland, J. G. Conformational changes accompany phosphorylation of the epidermal growth factor receptor C-terminal domain. *Protein Sci.* 2793–2803 (2005). doi:10.1110/ps.051630305.Signaling

105. Sabet, O. *et al.* Ubiquitination switches EphA2 vesicular traffic from a continuous safeguard to a finite signalling mode. *Nat. Commun.* **6,** 8047 (2015).

106. Perdios, L. *et al.* Conformational transition of FGFR kinase activation revealed by site-specific unnatural amino acid reporter and single molecule FRET. *Sci. Rep.* **7,** 39841 (2017).

107. Chin, J. W. Expanding and Reprogramming the Genetic Code of Cells and Animals. *Annu. Rev. Biochem.* 1–30 (2014). doi:10.1146/annurev-biochem-060713-035737

108. Greiss, S. & Chin, J. W. Expanding the Genetic Code of an Animal Expanding the Genetic Code of an Animal. *J. Am. Chem. Soc.* **2,** 14196–14199 (2011).

109. Bianco, A., Townsley, F. M., Greiss, S., Lang, K. & Chin, J. W. Expanding the genetic code of Drosophila melanogaster. *Nat. Chem. Biol.* **8,** 748–50 (2012).

110. Ernst, R. J. *et al.* Genetic code expansion in the mouse brain. *Nat. Chem. Biol.* 1–5 (2016). doi:10.1038/nchembio.2160

111. Lang, K. & Chin, J. W. Cellular Incorporation of Unnatural Amino Acids and Bioorthogonal Labeling of Proteins. *Chem. Rev.* **114,** 4764–4806 (2014).

112. Xie, J., Supekova, L. & Schultz, P. G. A genetically encoded metabolically stable analogue of phosphotyrosine in Escherichia coli. *ACS Chem. Biol.* **2,** 474–478 (2007).

113. Neumann, H., Peak-Chew, S. Y. & Chin, J. W. Genetically encoding N(epsilon)-acetyllysine in recombinant proteins. *Nat. Chem. Biol.* **4,** 232–234 (2008).

114. Gautier, A. *et al.* Genetically encoded photocontrol of protein localization in mammalian cells. *J. Am. Chem. Soc.* **132,** 4086–4088 (2010).

115. Wu, N., Deiters, A., Cropp, T. A. & Schultz, P. G. A genetically encoded photocaged amino acid supplement. *J. Am. Chem. Soc.* **126,** 14306–14307 (2004).

116. Deiters, A., Groff, D., Ryu, Y., Xie, J. & Schultz, P. G. A genetically encoded photocaged tyrosine. *Angew. Chemie* **45,** 2728–2731 (2006).

117. Lemke, E. a, Summerer, D., Geierstanger, B. H., Brittain, S. M. & Schultz, P. G. Control of protein phosphorylation with a genetically encoded photocaged amino acid. *Nat. Chem. Biol.* **3,** 769–772 (2007).

118. Uttamapinant, C. *et al.* Genetic Code Expansion Enables Live-Cell and Super-Resolution Imaging of Site-Specifically Labeled Cellular Proteins. *J. Am. Chem. Soc.* 150401152214003 (2015). doi:10.1021/ja512838z

119. Lang, K. *et al.* Genetic encoding of bicyclononynes and trans-cyclooctenes for site-specific protein labeling in vitro and in live mammalian cells via rapid fluorogenic diels-alder reactions. *J. Am. Chem. Soc.* **134,** 10317–10320 (2012).

120. Mullis, K. B. & Faloona, F. a. Specific Synthesis of DNA in Vitro via a Polymerase-Catalyzed Chain Reaction. *Methods Enzymol.* **155,** 335–350 (1987).

121. Laemmli, U. K. Cleavage of Structural Proteins during the Assembly of the Head of Bacteriophage T4. *Nature* **227,** 680–685 (1970).

122. Grecco, H. E., Roda-Navarro, P. & Verveer, P. J. Global analysis of time correlated single photon counting FRET-FLIM data. *Opt. Express* **17,** 6493–6508 (2009).

123. Baumdick, M. *et al.* EGF-dependent re-routing of vesicular recycling switches spontaneous phosphorylation suppression to EGFR signaling. *Elife* (2015). doi:10.7554/eLife.12223

124. Grecco, H. E. *et al.* In situ analysis of tyrosine phosphorylation networks by FLIM on cell arrays. *Nat. Methods* **7,** 467–472 (2010).

125. Walther, K. a, Papke, B., Sinn, M. B., Michel, K. & Kinkhabwala, A. Precise measurement of protein interacting fractions with fluorescence lifetime imaging microscopy. *Mol. Biosyst.* **7,** 322–336 (2011).

126. Okutani, T. *et al.* Grb2/Ash binds directly to tyrosines 1068 and 1086 and indirectly to tyrosine 1148 of activated human epidermal growth factor receptors in intact cells. *J. Biol. Chem.* **269,** 31310–31314 (1994).

127. Schmied, W. H., Elsa, S. J., Uttamapinant, C. & Chin, J. W. Efficient Multisite Unnatural Amino Acid Incorporation in Mammalian Cells via Optimized Pyrrolysyl tRNA Synthetase/tRNA Expression and Engineered eRF1. *J. Am. Chem. Soc.* (2014). doi:10.1021/ja5069728

128. Huyer, G. *et al.* Mechanism of inhibition of protein-tyrosine phosphatases by vanadate and pervanadate. *J. Biol. Chem.* **272,** 843–851 (1997).

129. Squire, A., Verveer, P. J., Rocks, O. & Bastiaens, P. I. H. Red-edge anisotropy microscopy enables dynamic imaging of homo-FRET between green fluorescent proteins in cells. *J. Struct. Biol.* **147,** 62–69 (2004).

130. Masip, M. E. *et al.* Reversible cryo-arrest for imaging molecules in living cells at high spatial resolution. (2016). doi:10.1038/nmeth.3921

131. Osherov, N. & Levitzki, A. Epidermal Growth Factor Dependent Activation of the Src Family Kinases. *Eur. J. Biochem.* **225,** 1047–1053 (1994).

132. Rusnak, D. W. *et al.* The effects of the novel, reversible epidermal growth factor receptor/ErbB-2 tyrosine kinase inhibitor, GW2016, on the growth of human normal and tumor-derived cell lines in vitro and in vivo. *Mol. Cancer Ther.* **1,** 85–94 (2001).

133. Moasser, M. M., Basso, A., Averbuch, S. D. & Rosen, N. The Tyrosine Kinase Inhibitor ZD1839 (" Iressa) Inhibits HER2-driven Signaling and Suppresses the Growth of HER2-overexpressing Tumor Cells. **1839,** 7184–7188 (2001).

134. Moyer, J. D. *et al.* Induction of Apoptosis and Cell Cycle Arrest by CP-358 , 774 , an Inhibitor of Epidermal Growth Factor Receptor Tyrosine Kinase. 4838–4848 (1997).

135. Biscardi, J. S. *et al.* c-Src-mediated Phosphorylation of the Epidermal Growth Factor Receptor on Tyr 845 and Tyr 1101 Is Associated with Modulation of Receptor Function. *J. Biol. Chem.* **274,** 8335–8343 (1999).

136. Batzer, A. G., Rotin, D., Ureña, J. M., Skolnik, E. Y. & Schlessinger, J. Hierarchy of binding sites for Grb2 and Shc on the epidermal growth factor receptor. *Mol. Cell. Biol.* **14,** 5192–5201 (1994).

137. Lemmon, M. a, Schlessinger, J. & Ferguson, K. M. The EGFR Family: Not So Prototypical Receptor Tyrosine Kinases. *Cold Spring Harb. Perspect. Biol.* **6,** (2014).

138. Kovacs, E., Zorn, J. A., Huang, Y., Barros, T. & Kuriyan, J. A Structural Perspective on the Regulation of the Epidermal Growth Factor Receptor. *Annu. Rev. Biochem.* **84,** 150126111306006 (2014).

139. Stadler, C. *et al.* Immunofluorescence and fluorescent-protein tagging show high correlation for protein localization in mammalian cells. *Nat. Methods* **10,** 315–323 (2013).

140. Teng, K. W. *et al.* Labeling proteins inside living cells using external fluorophores for microscopy. *Elife* **5,** 1–13 (2016).

141. Lukinavičius, G. *et al.* A near-infrared fluorophore for live-cell super-resolution microscopy of cellular proteins. *Nat. Chem.* **5,** 132–139 (2013).

142. Wagner, M. J., Stacey, M. M., Liu, B. a & Pawson, T. Molecular Mechanisms of SH2-and PTB- Domain-Containing Proteins in Receptor Tyrosine Kinase Signaling. *Cold Spring Harb. Perspect. Biol.* **5,** a008987 (2016).

143. Ibach, J. *et al.* Single particle tracking reveals that EGFR signaling activity is amplified in clathrin-coated pits. *PLoS One* **10,** 1–22 (2015).

144. Sato, K. I., Nagao, T., Iwasaki, T., Nishihira, Y. & Fukami, Y. Src-dependent phosphorylation of the EGF receptor Tyr-845 mediates Stat-p21waf1 pathway in A431 cells. *Genes to Cells* **8,** 995–1003 (2003).

145. Yao, Z. *et al.* A Global Analysis of the Receptor Tyrosine Kinase-Protein Phosphatase Interactome. *Mol. Cell* **65,** 347–360 (2017).

146. Pucheta-Martínez, E. *et al.* An Allosteric Cross-Talk Between the Activation Loop and the ATP Binding Site Regulates the Activation of Src Kinase. *Sci. Rep.* **6,** 24235 (2016).

147. Fritsche-Guenther, R. *et al.* Strong negative feedback from Erk to Raf confers robustness to MAPK signalling. *Mol. Syst. Biol.* **7,** 489–489 (2014).

148. Romsicki, Y., Kennedy, B. P. & Asante-Appiah, E. Purification and characterization of T cell protein tyrosine phosphatase reveals significant functional homology to protein tyrosine phosphatase-1B. *Arch. Biochem. Biophys.* **414,** 40–50 (2003).

149. Fan, Y. X., Wong, L., Deb, T. B. & Johnson, G. R. Ligand regulates epidermal growth factor receptor kinase specificity: Activation increases preference for Gab1 and Shc versus autophosphorylation sites. *J. Biol. Chem.* **279,** 38143–38150 (2004).

150. Wong, C. & Mcnally, C. EGF receptor ubiquitination is not necessary for its internalization. *Proc. Natl. Acad. Sci.* **104,** 16904–16909 (2007).

151. Shtiegman, K. *et al.* Defective ubiquitinylation of EGFR mutants of lung cancer confers prolonged signaling. *Oncogene* **26,** 6968–6978 (2007).

152. Thien, C. B. & Langdon, W. Y. EGF receptor binding and transformation by v-cbl is ablated by the introduction of a loss-of-function mutation from the Caenorhabditis elegans sli-1 gene. *Oncogene* **14,** 2239–2249 (1997).

153. Peschard, P. & Park, M. Escape from Cbl-mediated downregulation: A recurrent theme for oncogenic deregulation of receptor tyrosine kinases. *Cancer Cell* **3,** 519–523 (2003).

154. Ravid, T., Heidinger, J. M., Gee, P., Khan, E. M. & Goldkorn, T. c-Cbl-mediated ubiquitinylation is required for epidermal growth factor receptor exit from the early endosomes. *J. Biol. Chem.* **279,** 37153–37162 (2004).

155. Wang, K. *et al.* Optimized orthogonal translation of unnatural amino acids enables spontaneous protein double-labelling and FRET. *Nat. Chem.* **6,** 393–403 (2014).

156. Roepstorff, K. *et al.* Differential effects of EGFR ligands on endocytic sorting of the receptor. *Traffic* **10,** 1115–1127 (2009).

157. Macdonald-Obermann, J. L. & Pike, L. J. Different epidermal growth factor (EGF) receptor ligands show distinct kinetics and biased or partial agonism for homodimer and heterodimer formation. *J. Biol. Chem.* **289,** 26178–26188 (2014).

Publications and presentations

Parts of this work were presented in the following publication and conferences:

Publications

- Baumdick*, Martin; Brüggemann*, Yannick; Schmick*, Malte; Xouri*, Giorgia; Sabet, Ola; Davis, Llloyd; Chin, Jason W; Bastiaens, Philippe IH. 'EGF-dependent re-routing of vesicular recycling switches spontaneous phosphorylation suppression to EGFR signaling.' 2015. *Elife*, e12223.
- Baumdick, Martin; Gelleri, Marton; Uttamapinant, Chayasith; Beranek, Vaclav; Chin, Jason; Bastiaens, Philippe. 'A conformational sensor based on genetic code expansion reveals autocatalytic EGFR activation.' Submitted to *Nat Chem Biol*.

Conferences:

- EMBO conference. Signaling and Endomembranes. May 2017, Pula, Italy.
  Poster titel: 'Conformational sensor using genetic code expansion reveals the autocatalytic activation mechanism of EGFR.' Martin Baumdick, Jason W Chin, Philippe Bastiaens.
- Tag der Chemie. February 2017, Dortmund Germany.
  Presentation: 'Unraveling EGFR activation using a FRET-based, conformational EGFR biosensor.' Martin Baumdick, Jason W Chin, Philippe Bastiaens.
- Functional Genomics and Systems Biology. October 2015, Hinxton, UK.
  Poster titel: 'Ubiquitin-mediated switch of vesicular EGFR trafficking from a suppressive cycle to a unidirectional signaling mode.' Martin Baumdick, Yannick Brüggemann, Malte Schmick, Giorgia Xouri, Ola Sabet, Lloyd Davis, Jason W Chin, Philippe IH Bastiaens.
- Tag der Chemie. February 2015, Dortmund Germany.
  Poster titel: 'A ubiquitin-mediated switch differentiates between autonomous and ligand-dependent EGFR activation.' Martin Baumdick, Giorgia Xouri, Yannick Brüggemann, Lloyd Davis, Jason W Chin, Philippe IH Bastiaens.

Acknowledgement

At first, I would like to thank Prof. Dr. Philippe Bastiaens for giving me the opportunity to work on such an interesting project in his laboratory, for his excellent supervision and guidance that made the past five years to an exciting and enjoyable time. Second, I would like to thank Prof. Dr. Roger S. Goody for being the second reviewer of this thesis.

Special thanks go to Prof. Dr. Jason Chin for hosting me a couple of month in his laboratory in Cambridge and giving me the opportunity to gain insight in genetic code expansion. In this regard, I would also like to thank everyone in the Chin group, especially Tao, Vaclav and Roberto, for all their help and support in the lab, but also after work.

Tanja and Astrid, thank you for organizing the department and all your help with the administrative work. Thank you, Hendrike, Jutta, Kirsten, Manu, Lisaweta, Michael, Petra and Michelle for all your help in the labs. Sven and Michael, thank you for your great support with all the different microscopes.

Instead of naming all the people from Dept. II individually (sorry Amit) and taking the risk to forget someone, I would like to thank all of you for the great time, the nice atmosphere and all your support and motivation during my Phd.

Finally, I would like to thank my family and especially Charlotte for their constant support during the past five years that made my life much easier.